Università degli Studi di Napoli “Federico II”

Dipartimento di Ingegneria Chimica

Dottorato in Ingegneria Chimica

XX Ciclo

Tesi di Dottorato

COMPUTATIONAL RHEOLOGY OF SOLID SUSPENSIONS

Gaetano D’Avino

Comitato Scientifico

Prof. Crescitelli Silvestro
Prof. Maffettone Pier Luca
Prof. Hulsen Martien A.
Prof. Grizzuti Nino
Dr. Greco Francesco

Coordinatore del Dottorato

Prof. Maffettone Pier Luca

Contents

Chapter 1

Introduction

1.1 General introduction and objectives

In the last years, an increasing interest in materials filled with solid particles is observed. Indeed, these materials show many interesting features such as high mechanical toughness, low costs, many application fields. In general, a suspension consists of discrete particles randomly distributed in a fluid medium. They can be divided in three categories according to the physical state of the particles inside the liquid: solid suspensions (solid particles in a liquid), emulsions (liquid droplets in a liquid) and gas in a liquid. In this work we will consider solid particles in a liquid.

There are many important applications of these kinds of materials: polymer melts with fillers, biomedical materials, paints, inks, rubbers, food, etc. So it is very important to understand the rheological properties of these composites in order to improve the processing stage and to predict their mechanical properties.

Important characteristics of solid particle suspensions are the filler size, shape, and concentration, plus the rheology of the suspending liquid. The possible range of variation of those parameters leads to quantitative and qualitative changes of the suspension properties. For an example, solid inclusions can range from macroscopic to nanoscopic characteristic dimensions, hence the appropriate dynamics of these systems is governed by very different laws. Consequently, a very ample literature does exist on suspension mechanics, often centered on specific topics (see e.g. the reviews [1, 2, 3]).

It is well known that the addition of rigid particles to a liquid alters the flow field. An example of the effect of an inclusion in a fluid is depicted in Figure 1.1 [4, 5]: the sphere determines a strong deformation in the streamlines. The streamlines become regular sufficiently far from the particles, where the fluid does not feel the presence of the inclusions. It is quite obvious that two or more particles close to each other lead to even more drastic changes in the fluid dynamic of the suspension with respect to the unfilled fluid (see Figure 1.1b and 1.1c). In general, no theory can be assessed in such a situation.

Furthermore, with increasing volume fraction, the hydrodynamic effects lead to variations in the rheological properties too [6] and the presence of high concentrations of solid

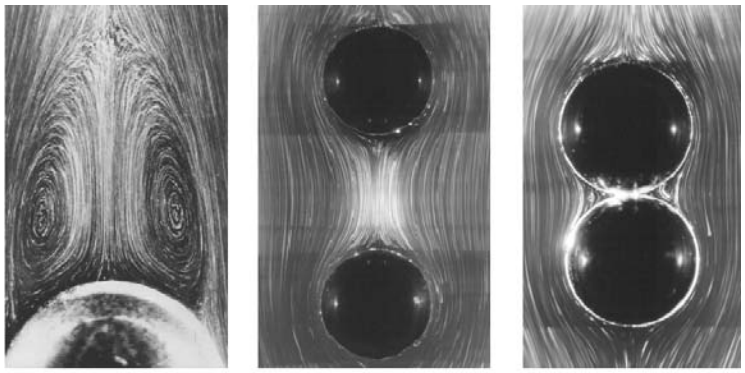

Figure 1.1: Streamline pattern visualized by suspending aluminum powder. (from [4, 5]).

particles can lead to typical viscoelastic phenomena such as shear thinning or shear thickening, even if the fluid medium shows a Newtonian behaviour.

For an example, in Figure 1.2 (from [7]), the viscosity of a suspension of charged poly(styrene-ethylacrylate) copolymer spheres in water as a function of shear stress is plotted. The curves refer to different volume fractions. In spite of the Newtonian nature of the suspending fluid, non linear behaviors can be observed. First of all, an increasing viscosity is found if the concentration of particles is increased. Furthermore, if the volume fraction is sufficiently high, the viscosity shear thins, showing a typical phenomenon of a viscoelastic fluid.

Therefore, the solid volume fraction in these materials is a crucial parameter and, by varying it, completely different phenomena can be observed. In this regard, the suspensions can be divided in dilute and concentrated systems, according to the quantity of the filler inside the fluid. A suspension is considered dilute if the solid volume fraction is not more than $5 - 6\%$, whereas for a concentrated suspension it can even achieve the $30 - 40\%$.

The simplest case that one can consider is the rheology of a dilute suspension of non-Brownian rigid spheres in a Newtonian fluid. The 100 years old analysis by Einstein [8] gives the first prediction of the bulk rheology of a dilute suspension of buoyancy-free, inertialess rigid spheres in a Newtonian liquid, condensed in the famous formula $\eta = \eta_0(1 + 2.5\phi)$ (with η the viscosity of the suspension, η_0 the viscosity of the suspending fluid, and ϕ the volume fraction). However, despite of the obvious relevance, the viscoelasticity of the suspending fluid has received relatively scarce attention.

The objective of this thesis is to analyze the rheology and the flow fields of a suspension of solid particles inside a viscoelastic medium. The analysis is carried out for dilute as well as concentrated systems, by using, of course, different procedures. Indeed, the main difference regards the hydrodynamic effects between the particles. The main assumption in a dilute system is that the particles are so far one to each other that they do not feel the presence of the others. In other words, no hydrodynamic interaction arises. On the contrary, by increasing the solid concentration, the particles are very close so the hydrodynamic effects cannot be neglected anymore and they play an important role affecting the

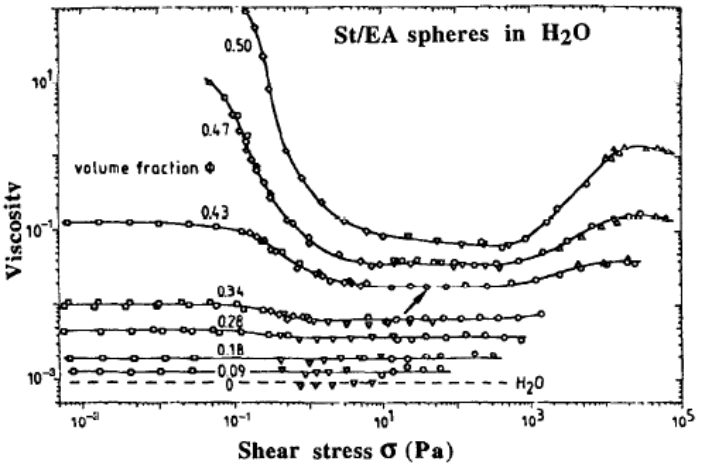

Figure 1.2: Viscosity versus shear stress for aqueous suspensions of charged poly(styrene-ethylacrylate) copolymer spheres at various volume fractions (from [7]).

rheology and the local flow fields. In conclusion, we need a different simulation algorithm in order to take into account the hydrodynamic effects.

In both cases, the local fields (such as velocity, pressure, stress tensor, etc.) are calculated by solving the governing equations of the system. These distributions give useful information about the microstructure of the suspension and they show how the presence of the inclusions can affect the fluid domain with respect to the unfilled medium. Then, the macroscopic properties of the suspension as a whole (= bulk properties) are investigated. These properties are related to the bulk stress that is recovered by integrating the local stress field over the whole fluid domain. In this regard, we use the Batchelor bulk stress formula [9] where the bulk stress is given by a fluid as well as a solid contribution.

1.2 Dilute suspensions

This work can be divided in two main parts. In the first one, the main assumption is the diluteness of the system. The fluid is modeled like a viscoelastic medium and the first analysis is carried out by choosing the Second Order Fluid (SOF) model. The SOF theory is valid when the flow is slow and slowly varying, i.e. very low Weissenberg number. This feature allows to carry out a perturbative approach in order to solve the problem. Therefore, an analytical procedure can be assessed.

In the past, the same problem has been studied in three different works [10, 11, 12], giving conflicting results. Quite recently, the problem has been reanalyzed by Koch and Subramanian [13] as well. In the latter paper, a clear discussion on the limitations of older analyses [10, 11, 12] is also reported.

It's important to point out that slight discrepancies between our derivation and [13] exist. Our stress prediction (see [14, 15, 16]), indeed, does not agree with that proposed

by [13].

In order to check the validity of our derivation, the problem is solved by means of numerical simulations as well. As shown in Chapter II and in [14, 15, 16], our analytical results are in excellent agreement with the numerical calculations, in the $Wi-$range where the SOF (and the perturbative technique) is valid. Moreover, a good qualitative agreement with experimental data is also found [17, 18, 19].

In the Chapter III, we abandon the SOF limit and we analyze a solid suspension in the same hypotheses but at high Weissenberg number. In order to manage the problem, more realistic constitutive equations need to be considered. Due to the mathematical complexity of the problem, an analytical theory cannot be assessed anymore and numerical simulations are required.

Recent experimental data [20] showed that particles in a viscoelastic fluid, subjected to simple shear flow, slow down with respect to a Newtonian medium. Moreover, the slowing down effect is more and more pronounced if the viscoelasticity of the suspending fluid increases.

Therefore, we primarily focus the attention on the rotation rate of the sphere inside the liquid, subjected to a shear flow, in order to capture the slowing down phenomenon. Different viscoelastic constitutive equations are chosen to try to relate the slowing down effect to a particular non linear phenomenon. Finally, we study the rheology of such a material as well, giving predictions for the relevant material functions (both transient and steady state).

1.3 Concentrated suspensions

In the second part of the thesis we abandon the hypotheses of diluteness and we consider concentrated suspensions. It's important to point out that a concentrated suspension is quite different from a dilute one because of the hydrodynamic interactions. Indeed, if the solid volume fraction is sufficiently high, the particles interfere one with each other. Therefore a completely different simulation scheme needs to be developed in order to manage the system. In this regard, many procedures have been developed in order to simulate concentrated systems, based on assumptions such as potential flow, Stokes flow, etc. [21, 22, 23]. However, these methods are only suitable for a Newtonian matrix fluid.

In the past, the problem was approached by modeling the hydrodynamic interactions [24, 25, 26] through theoretical considerations. Of course, this way to face the problem is limited to very specific applications and the interactions between particles are just approximations.

In the last two decades, Direct Numerical Simulations (DNS) techniques have been developed. They solve the (Navier-)Stokes equations directly for the fluid and the rigid-body motion equations for the solid. These equations are coupled through the no-slip condition on the particle boundaries, and through the hydrodynamic forces and torques which appear in the equations of the rigid-body motion. These hydrodynamic forces and torques must, of course, be those arising from the computed motion of the fluid, and so

are not known in advance, but only as the integration proceeds. It has to be pointed out that no approximation for these forces and torques is made. So, through DNS methods, hydrodynamic interactions are not modeled but computed.

In order to simulate really concentrated suspensions, a sufficiently high number of particles must be considered. On the other hand, a relatively small computational domain is needed to make the simulations feasible. A simple way to do this is to impose periodicity in all the directions so the computational domain is just a frame of an infinite domain. This concept was used by Hwang et al. [27, 28] to simulate solid concentrated suspensions in shear flow. In their scheme, the computational domain is a frame sliding with respect to each other. They applied the simulation scheme to Newtonian as well viscoelastic suspensions (in 2D case) with promising results.

An attempt to extend the bi-periodic concept to elongational flow has been done by the same authors [29]. However, in this case, the computational frame deforms because of the imposed flow. Therefore, a limitation in the maximum strain attained exists and no steady state can be achieved. For viscoelastic fluids, this means that, for high Weissenberg number, a large frame size is required. Furthermore, the moving mesh leads to remeshing and projection with a consequent loss in accuracy. Finally, the above mentioned scheme is only applied to Newtonian suspensions and we are not aware of simulations of viscoelastic suspensions in such a flow.

In Chapter IV, then, we propose a new numerical scheme in order to easily handle such a problem. We consider a concentrated suspension of rigid, non-Brownian disks in a planar elongational flow, where the particle and fluid inertia can be neglected. The main concept of the procedure is to randomly relocate a particle on an inflow section when it goes out from the computational domain. In order to fix boundary conditions sufficiently far from the particles and to allow the stress tensor surrounding a particle to be fully developed, we implement a three-layer scheme.

A Lagrange Multiplier/Fictitious Domain Method (LM/FDM) has been used [30] and the force-free, torque-free rigid body motion of the particles is described by a rigid-ring problem [27, 28]. So, a fixed mesh is used for the computation and the particles are described by their boundaries only, through collocation points. This description is possible because inertia is neglected. Finally, the rigid-body motion constraints are imposed through Lagrange multipliers, that can be identified as traction forces on the particle surfaces (with the contribution of the fluid pressure inside the object). Numerical simulations with many particles are performed and bulk rheological properties are discussed.

In Chapter V, the extension of our scheme to viscoelastic suspending fluid is carried out. The scheme is coupled with discretization techniques for viscoelastic fluids in order to improve the numerical stability. A many-particle system is analyzed and the local and bulk rheological quantities are investigated.

Again a comparison with experimental data found in the literature is carried out. Our simulations qualitatively agree. Moreover, we are able to predict the typical phenomena observed in the experiments, such as the reduction of the strain hardening in a filled polymer melt subjected to an elongational flow field.

Chapter 2

The Second Order Fluid theory

2.1 Introduction

The properties and the features of solid particle suspensions are influenced by many factors such as the filler, the matrix, hydrodynamic interactions. A vast literature [1, 3, 2, 31] showed that different properties of particles (such as shape and size), the nature of the fluid and the solid concentration can lead to quantitative and qualitative changes in the final behaviour of material properties. Indeed, depending on the spatial and time scale (i.e. nanoscopic/macrocospic solid dimensions, viscous/viscoelastic fluid), very different laws can govern the dynamic of such a materials. Of course, different approaches to study their properties are required.

The simplest case that one can imagine is to consider spherical, non-Brownian, buoyancy free, inertialess particles in dilute conditions. These hypotheses fix the properties of the filler: spherical particles sufficiently big with respect to the solvent molecular size (the Brownian motion can be neglected) and sufficiently far one to each other so that no hydrodynamic effect occurs (diluteness). Finally, a choice about the suspending fluid needs to be done. In this regard, we call "Newtonian" a suspension where the fluid shows the well known Newtonian behaviour whereas "viscoelastic" if the matrix shows typical non linear phenomena like shear thinning, elongational thickening, memory effects, etc.

Under the assumptions mentioned above, Newtonian suspensions have been subject to a vast analysis. The first prediction of bulk viscosity has been provided by Einstein [8] and is condensed in the famous formula $\eta = \eta_0(1 + \frac{5}{2}\phi)$ (with η the viscosity of the suspension, η_0 the viscosity of the suspending fluid, and ϕ the volume fraction). The pressure and velocity of the fluid surrounding the particles are known as well and analytical expressions are derived [32]. Furthermore, many experimental results confirm these predictions.

In spite of the obvious importance, the effects of viscoelasticity of the suspending fluid have received relatively scarce attention. The simplest way to take into account the viscoelastic behavior of the matrix is to consider, as constitutive equation, the so-called "Second Order Fluid", i.e., the most general properly invariant stress tensor quadratic in the velocity gradient [33]. The SOF stress tensor is the asymptote of an extremely ample class

of viscoelastic constitutive equations, for sufficiently slow and slowly varying flows [33].

The system discussed above has been analyzed in the past, giving conflicting results [10, 11, 12]. Quite recently, the problem has been reanalyzed by Koch and Subramanian [13] as well. In the latter paper, a clear discussion on the limitations of older analyses [10, 11, 12] is also reported. It should be mentioned, however, that slight discrepancies between our derivation presented in the following and [13] exist. Our stress prediction [14, 15, 16], indeed, does not agree with that proposed by [13].

In this Chapter, the analysis of a spherical particle suspensions in a SOF is carried out. We present the analytical procedure used and then proceed to compare the predictions with thorough 3D numerical simulations of the same fluid dynamic problem. The analytic derivation consists in a perturbative solution of the continuity and momentum equations of fluid mechanics for a single sphere immersed in a "Second Order Fluid" [33] subjected to a general linear flow field imposed at infinity. Correspondingly, numerical solutions for the single sphere problem are obtained with commercial codes.

The single sphere solution is then exploited to obtain the rheology of a very dilute monodisperse suspension of non-Brownian, buoyancy free, inertialess, rigid spheres immersed in a "Second Order Fluid". Bulk stresses are analytically and numerically computed through a standard volume averaging procedure [32, 9].

The analytic perturbative predictions and numerical results are found to be in excellent agreement with each other.

2.2 Statement of the problem

As stated in the Introduction, in this Chapter we analyze the fluid dynamic of a suspension of rigid spheres in a non-Newtonian suspending fluid. To maintain the highest possible generality, we here adopt "Second Order Fluid" (SOF) constitutive equation. The stress tensor $\boldsymbol{T}$ is given by:

$$\boldsymbol{T} = -p\boldsymbol{I} + \boldsymbol{\tau} = -p\boldsymbol{I} + 2\eta_0\boldsymbol{D} + \alpha_0\boldsymbol{A} + \beta_0\boldsymbol{D}^2 \tag{2.1}$$

In Eq. (2.1), p is the pressure (with $\boldsymbol{I}$ the identity tensor), $\boldsymbol{\tau}$ is the deviatoric part of the stress tensor, $2\boldsymbol{D} = \nabla\boldsymbol{v} + \nabla\boldsymbol{v}^T$ is the rate of deformation tensor, with $\boldsymbol{v}$ the velocity, and $\boldsymbol{A} = 2(\dot{\boldsymbol{D}} + \boldsymbol{D}\cdot\nabla\boldsymbol{v} + \nabla\boldsymbol{v}^T\cdot\boldsymbol{D})$ is the second Rivlin-Ericksen tensor, with the superimposed dot indicating the material time derivative. The coefficients α_0 and β_0 are constant constitutive parameters that account for elastic properties of the fluid. (Note that α_0 is a negative quantity.) It might be worthwhile to recall that those coefficients are linked to the first and second normal stress coefficients, Ψ_1 and Ψ_2 respectively, through the well known relationships: $\alpha_0 = -\Psi_1/2$, $\beta_0 = 4(\Psi_1 + \Psi_2)$.

Notice that the ratio $-\alpha_0/\eta_0$ is a characteristic viscoelastic time of the fluid.

As mentioned in the Introduction, the bulk rheology of a monodisperse dilute suspension of rigid, buoyancy free, inertialess, non-Brownian spheres can be determined once the single sphere fluid dynamic problem is solved [32, 9].

The problem of a single sphere in an externally imposed flow field, under isothermal condition, consists of the continuity (mass balance) and momentum balance equations. The imposed velocity field is linear at infinity, with a given velocity gradient $\nabla \boldsymbol{v}^\infty$, here assumed to be constant in time, i.e., we only solve the steady state problem. Negligible inertia, incompressibility and buoyancy free conditions are also assumed. By choosing the sphere radius R_0 as the characteristic length, and $\eta\|2\boldsymbol{D}^\infty\|$ as the characteristic stress, the nondimensional continuity and momentum equations then read:

$$\nabla \cdot \boldsymbol{v} = 0 \tag{2.2}$$

$$-\nabla p + \nabla^2 \boldsymbol{v} - Wi(\nabla \cdot \boldsymbol{A} + b\nabla \cdot \boldsymbol{D}^2) = \boldsymbol{0} \tag{2.3}$$

(All symbols appearing in these equations are for dimensionless quantities.) In Eq. (2.3), $b = \beta_0/\alpha_0$ is a purely constitutive dimensionless parameter, and Wi is the so-called Weissenberg number, the ratio between the constitutive characteristic time $-\alpha_0/\eta_0$ and the imposed characteristic time $1/\|2\boldsymbol{D}^\infty\|$ of the flow field. Thus, $Wi = 0$ represents a fluid with negligible internal characteristic time (a Newtonian fluid), whereas $Wi \neq 0$ describes viscoelastic situations. Realistic values for b range between -8 and -5, see [34].

Boundary conditions are assigned at infinity and on the sphere surface. At infinity it is:

$$p \to p^\infty \tag{2.4}$$

$$\boldsymbol{v} \to \nabla \boldsymbol{v}^\infty \cdot \boldsymbol{r} \tag{2.5}$$

with p^∞ a constant pressure.

Concerning the boundary conditions at the sphere surface, it proves convenient to adopt a frame of reference centered at the sphere center. The position vector $\boldsymbol{r}$ is then written as $\boldsymbol{r} = r\boldsymbol{u}$, with $r = |\boldsymbol{r}|$, and $\boldsymbol{u}$ a unit vector identifying a direction in space. No slip condition holds on the sphere surface $r = 1$. We also assume, as usually done, that the sphere is "freely rotating" [35, 36], i.e., that its rotation (if any) is only due to the motion of the surrounding fluid. This means that the total torque acting on the sphere is zero. Thus, the boundary conditions at $r = 1$ are:

$$\boldsymbol{v} = \tilde{\boldsymbol{v}} \tag{2.6}$$

$$\int_{4\pi} \boldsymbol{u} \times \boldsymbol{T} \cdot \boldsymbol{n}\, dA = \boldsymbol{0} \tag{2.7}$$

where $\boldsymbol{n}$ is the normal at the sphere surface (of course it is $\boldsymbol{n} \equiv \boldsymbol{u}$), and the integral of the local torque $\boldsymbol{u} \times \boldsymbol{T} \cdot \boldsymbol{n}\, dA$ spans the unit sphere surface 4π. The nondimensional local stress $\boldsymbol{T}$ in Eq. (2.7) is:

$$\boldsymbol{T} = -p\boldsymbol{I} + 2\boldsymbol{D} - Wi(\boldsymbol{A} + b\boldsymbol{D}^2) \tag{2.8}$$

The unknown time-independent velocity $\tilde{\boldsymbol{v}}$ in Eq. (2.6) is at any point on the sphere surface the linear velocity of that point. Hence, $\tilde{\boldsymbol{v}}$ is everywhere tangential to the surface, i.e.,

$\tilde{\boldsymbol{v}} \cdot \boldsymbol{n} = 0$. This velocity can be determined through Eq. (2.7). Of course, in an irrotational flow field it is $\tilde{\boldsymbol{v}} = \boldsymbol{0}$.

Once the pressure and the velocity fields are calculated for the single sphere problem, the bulk stress of the dilute monodisperse suspension is obtained by volume averaging of the single sphere local stress [32, 9, 37]. Indeed, "in the limit $c \to \infty$ (where c is the concentration of particle by volume) the flow near each particle is that which would be set up if it alone were immersed in an infinite body of ambient fluid with a uniform velocity gradient at large distance from the particle" [9]. The nondimensional bulk stress $\langle \boldsymbol{T} \rangle$ is then calculated as:

$$\langle \boldsymbol{T} \rangle = \frac{\int_{\mathbb{R}^3 - \frac{4\pi}{3}} \boldsymbol{T} dV}{\int_{\mathbb{R}^3} dV} + \frac{3\phi}{4\pi} \int_{4\pi} \boldsymbol{T} \cdot \boldsymbol{n}\boldsymbol{n} dA \tag{2.9}$$

In Eq. (2.9), $4\pi/3$ and 4π are the volume and the surface area, respectively, of the sphere with unit radius, $\mathbb{R}^3$ indicates the entire space, and ϕ is the suspension volume fraction. Equation (2.9) is the standard way the dilute suspension bulk stress is calculated (e.g., [32, 9]). Of course, the diluteness assumption implies the linearity of the bulk stress in the volume fraction ϕ.

2.3 Perturbative analysis

We proceed now to the perturbative analysis of Eqs. (2.2), (2.3) (together with their boundary conditions), with Wi as the expansion parameter. The pressure and velocity fields are formally expanded up to first order in Wi:

$$p = p_{EIN} + Wi \; p_{SOF} \tag{2.10}$$

$$\boldsymbol{v} = \boldsymbol{v}_{EIN} + Wi \; \boldsymbol{v}_{SOF} \tag{2.11}$$

with obvious notation. The zeroth order fields are those determined by Einstein for a Newtonian suspending fluid. They are [32]:

$$p_{EIN} = -\frac{5}{r^3} \boldsymbol{D}^{\infty} : \boldsymbol{u}\boldsymbol{u} + p^{\infty} \tag{2.12}$$

$$\boldsymbol{v}_{EIN} = \left(\frac{5}{2r^4} - \frac{5}{2r^2} \right) \boldsymbol{D}^{\infty} : \boldsymbol{u}\boldsymbol{u}\boldsymbol{u} - \frac{1}{r^4} \boldsymbol{D}^{\infty} \cdot \boldsymbol{u} + r \nabla \boldsymbol{v}^{\infty} \cdot \boldsymbol{u} \tag{2.13}$$

At order Wi, the fields p_{SOF} and $\boldsymbol{v}_{SOF}$ are determined by solving the following balance equations:

$$\nabla \cdot \boldsymbol{v}_{SOF} = 0 \tag{2.14}$$

$$-\nabla p_{SOF} + \nabla^2 \boldsymbol{v}_{SOF} - \left(\nabla \cdot \boldsymbol{A}_{EIN} + b \nabla \cdot \boldsymbol{D}_{EIN}{}^2 \right) = \boldsymbol{0} \tag{2.15}$$

The appropriate boundary conditions are, for $r \to \infty$:

$$p_{SOF} \to 0 \tag{2.16}$$

$$\boldsymbol{v}_{SOF} \to \boldsymbol{0} \tag{2.17}$$

and, at $r = 1$:

$$\boldsymbol{v}_{SOF} = \boldsymbol{0} \tag{2.18}$$

Indeed, the order Wi fields are nil at infinity because the zeroth order Einstein solution already fulfills the "complete" boundary conditions, Eqs. (2.4) and (2.5). On the other hand, the order Wi condition at $r = 1$, Eq. (2.18), is already known in the literature [35]. A novel simple derivation of this result is reported in Appendix A.

2.4 Perturbative solution

Looking at the mathematical structure of the balance equations at order Wi, Eq. (2.14) and Eq. (2.15), the following standard analytic solution procedure can be applied. By taking the divergence of Eq. (2.15), and by using the incompressibility condition (Eq. (2.14)), one gets a Poisson equation for p_{SOF} with a density term $\nabla \cdot \left(\nabla \cdot \boldsymbol{A}_{EIN} + b\nabla \cdot \boldsymbol{D}_{EIN}{}^2\right)$ calculated from the Einstein solution. Once this equation is solved for the pressure, one goes back to Eq. (2.15), which then becomes a (vectorial) Poisson equation for the velocity $\boldsymbol{v}_{SOF}$. In this case, the density term is $\nabla \overline{p}_{SOF} + \left(\nabla \cdot \boldsymbol{A}_{EIN} + b\nabla \cdot \boldsymbol{D}_{EIN}{}^2\right)$ where $\overline{p}_{SOF}$ is now the known pressure field.

The solution of these Poisson equations is greatly facilitated by the adoption of a tensorial representation of the unknown p_{SOF} and $\boldsymbol{v}_{SOF}$ fields, following the approach of [38]. The form of such fields is:

$$p_{SOF} = p_1 \boldsymbol{D}^\infty \boldsymbol{D}^\infty :: \boldsymbol{uuuu} + p_2 \boldsymbol{D}^\infty \cdot \boldsymbol{D}^\infty : \boldsymbol{uu} + p_3 \boldsymbol{D}^\infty : \boldsymbol{D}^\infty + p_4 \boldsymbol{A}^\infty : \boldsymbol{uu} \tag{2.19}$$

$$\begin{aligned} \boldsymbol{v}_{SOF} = {} & v_1 \boldsymbol{D}^\infty \boldsymbol{D}^\infty :: \boldsymbol{uuuuu} + v_2 \boldsymbol{D}^\infty \cdot \boldsymbol{D}^\infty : \boldsymbol{uuu} + v_3 \boldsymbol{D}^\infty : \boldsymbol{D}^\infty \, \boldsymbol{u} + \\ & v_4 \boldsymbol{D}^\infty : \boldsymbol{uu} \, \boldsymbol{D}^\infty \cdot \boldsymbol{u} + v_5 \boldsymbol{D}^\infty \cdot \boldsymbol{D}^\infty \cdot \boldsymbol{u} + v_6 \boldsymbol{A}^\infty : \boldsymbol{uuu} + v_7 \boldsymbol{A}^\infty \cdot \boldsymbol{u} \end{aligned} \tag{2.20}$$

These equations are the most general properly invariant expressions for a scalar (Eq. (2.19)) and a vector (Eq. (2.20)) quadratic in the imposed flow field at infinity. Needless to say, with the nondimensionalisation scales adopted in this work, the quadratic expressions just reported are in fact linear in the perturbation parameter Wi. From Eq. (2.19) and Eq. (2.20), the angular dependence of the pressure and velocity fields is therefore completely known beforehand. The yet unknown scalar functions p_i and v_i account for the radial dependence of those fields, and are functions of the constitutive parameter b.

The above mentioned Poisson equations thus reduce to a set of ordinary differential equations for p_i and v_i (see [39]). In terms of the p_i and v_i functions, the boundary conditions reduce to $p_i \to 0$ and $v_i \to 0$ at infinity, and to $v_i = 0$ at the sphere surface.

In conclusion, the complete set of functions is calculated as:

$$p_1 = \frac{45\ (6+b)}{4\,r^{10}} - \frac{25\ (11+2\,b)}{2\,r^8} + \frac{25\ (10+3\,b)}{4\,r^6} - \frac{35\ (60+11\,b)}{16\,r^5} + \frac{25\ (8+b)}{2\,r^3} \quad (2.21)$$

$$p_2 = \frac{15\ (6+b)}{r^{10}} - \frac{10\ (11+2\,b)}{r^8} + \frac{25\ (8+b)}{8\,r^6} + \frac{5\ (60+11\,b)}{4\,r^5} - \frac{5\ (228+43\,b)}{28\,r^3} \quad (2.22)$$

$$p_3 = \frac{6+b}{2\,r^{10}} - \frac{60+11\,b}{8\,r^5} + \frac{25\ (4+b)}{28\,r^3} \quad (2.23)$$

$$p_4 = \frac{-5}{2\,r^3} \quad (2.24)$$

$$v_1 = \frac{25\ (4+b)}{4\,r^7} - \frac{495\ (4+b)}{32\,r^6} + \frac{25\ (4+b)}{2\,r^5} - \frac{105\ (4+b)}{32\,r^4} \quad (2.25)$$

$$v_2 = \frac{-5\ (4+b)}{4\,r^7} + \frac{55\ (4+b)}{8\,r^6} - \frac{75\ (4+b)}{8\,r^5} + \frac{215\ (4+b)}{56\,r^4} - \frac{5\ (4+b)}{56\,r^2} \quad (2.26)$$

$$v_3 = \frac{-55\ (4+b)}{112\,r^6} + \frac{25\ (4+b)}{24\,r^5} - \frac{65\ (4+b)}{112\,r^4} + \frac{5\ (4+b)}{168\,r^2} \quad (2.27)$$

$$v_4 = \frac{-25\ (4+b)}{8\,r^7} + \frac{55\ (4+b)}{8\,r^6} - \frac{75\ (4+b)}{16\,r^5} + \frac{15\ (4+b)}{16\,r^4} \quad (2.28)$$

$$v_5 = \frac{-55\ (4+b)}{28\,r^6} + \frac{25\ (4+b)}{8\,r^5} - \frac{65\ (4+b)}{56\,r^4} \quad (2.29)$$

$$v_6 = 0, \quad (2.30)$$

$$v_7 = 0. \quad (2.31)$$

Once these equations are inserted in Eq. (2.19) and in Eq. (2.20), the analytic pressure and velocity fields at order Wi are completely determined, for whatever imposed velocity gradient at infinity. It can be verified that our solution for p and $\boldsymbol{v}$ coincides with that reported in [13], which was originally derived by [40]. It should be stressed that the derivation given here, based on the invariance properties of the pressure and velocity fields, is different from that of Peery [40].

2.5 Bulk stress

The nondimensional bulk stress composes of the Einstein stress plus the Wi first order contribution, as follows:

$$\langle \boldsymbol{T} \rangle = \langle \boldsymbol{T}_{EIN} \rangle + Wi \langle \boldsymbol{T}_{SOF} \rangle \quad (2.32)$$

where:

$$\langle \boldsymbol{T}_{EIN} \rangle = \frac{\int_{\mathbb{R}^3 - \frac{4\pi}{3}} (-p_{EIN}\boldsymbol{I} + 2\boldsymbol{D}_{EIN}) dV}{\int_{\mathbb{R}^3 - \frac{4\pi}{3}} dV} + \frac{3\phi}{4\pi} \int_{4\pi} (-p_{EIN}\boldsymbol{I} + 2\boldsymbol{D}_{EIN}) \cdot \boldsymbol{nn} dA \quad (2.33)$$

$$\langle \boldsymbol{T}_{SOF} \rangle = \frac{\int_{\mathbb{R}^3 - \frac{4\pi}{3}} \left[-p_{SOF}\boldsymbol{I} + 2\boldsymbol{D}_{SOF} - \left(\boldsymbol{A}_{EIN} + b\boldsymbol{D}^2_{EIN} \right) \right] dV}{\int_{\mathbb{R}^3 - \frac{4\pi}{3}} dV} + \frac{3\phi}{4\pi} \int_{4\pi} \left[-p_{SOF}\boldsymbol{I} + 2\boldsymbol{D}_{SOF} - \left(\boldsymbol{A}_{EIN} + b\boldsymbol{D}^2_{EIN} \right) \right] \cdot \boldsymbol{nn} dA \tag{2.34}$$

Upon substitution of the Einstein and SOF single sphere fields in Eq. (2.33) and (2.34), the nondimensional total bulk stress tensor $\langle \boldsymbol{\tau} \rangle$ is obtained by performing the integrations. The Einstein contribution is already well known.

For what matters the SOF contribution, the volume and surface integrals are calculated as follows. Straightforward computations lead to the following convenient expression for the local stress tensor $\boldsymbol{T}_{SOF} = -p_{SOF}\boldsymbol{I} + 2\boldsymbol{D}_{SOF} - \left(\boldsymbol{A}_{EIN} + b\boldsymbol{D}^2_{EIN} \right)$:

$$\boldsymbol{T}_{SOF} = \boldsymbol{F}(r, \boldsymbol{u}) + \left(1 - \frac{1}{r^5} \right) \boldsymbol{A}^\infty + \left(b + \frac{4+b}{r^{10}} - \frac{4+2\,b}{r^5} \right) \boldsymbol{D}^\infty \cdot \boldsymbol{D}^\infty \tag{2.35}$$

where the $\boldsymbol{F}$ is a known tensorial function of r and $\boldsymbol{u}$, parametric in the velocity gradient at infinity. Upon volume integration it turns out that no contribution arises from $\boldsymbol{F}$. Indeed, the most slowly decaying power of r in $\boldsymbol{F}$ is r^{-3}, which generates a logarithmic divergence upon volume integration. Such a divergence is overwhelmed by the volume integral in the denominator of Eq. (2.34), however, and hence no contribution of $\boldsymbol{F}$ survives. (A completely analogous mathematics holds when deriving the Einstein volume contribution from Eq. (2.33)) The only surviving terms of Eq. (2.35) give then the volume contribution to the bulk SOF stress as $\boldsymbol{A}^\infty + b\boldsymbol{D}^\infty \cdot \boldsymbol{D}^\infty$. (Analogously, the volume contribution to the bulk Einstein stress is $\boldsymbol{D}^\infty$, see [32, 9])

In calculating the surface contribution to the bulk SOF stress, the local dyadic $\boldsymbol{M}_{SOF} = \boldsymbol{T}_{SOF} \cdot \boldsymbol{nn}$ appears, which can be written as:

$$\boldsymbol{M}_{SOF} = m_1 \boldsymbol{D}^\infty \boldsymbol{D}^\infty :: \boldsymbol{uuuuuu} + m_2 \boldsymbol{D}^\infty \cdot \boldsymbol{D}^\infty : \boldsymbol{uuuu} + m_3 \boldsymbol{D}^\infty : \boldsymbol{D}^\infty \, \boldsymbol{uu} + m_4 \boldsymbol{D}^\infty : \boldsymbol{uu} \, \boldsymbol{D}^\infty \cdot \boldsymbol{uu} + m_5 \boldsymbol{D}^\infty \cdot \boldsymbol{D}^\infty \cdot \boldsymbol{uu} + m_6 \boldsymbol{A}^\infty : \boldsymbol{uuuu} + m_7 \boldsymbol{A}^\infty \cdot \boldsymbol{uu} \tag{2.36}$$

(Recall that $\boldsymbol{n} \equiv \boldsymbol{u}$) Notice that the m_i functions in Eq. (2.36) are only needed at $r = 1$ to compute the surface integral. Details on the integration of the dyad $\boldsymbol{M}_{SOF}$ and the list of coefficients m_i are reported in Appendix B.

Collecting the results of the volume and surface integration, the total nondimensional deviatoric bulk stress of the suspension is obtained as:

$$\langle \boldsymbol{\tau} \rangle = 2 \left(1 + \frac{5}{2}\phi \right) \boldsymbol{D}^\infty - Wi \left[\left(1 + \frac{5}{2}\phi \right) \boldsymbol{A}^\infty + b \left(1 + \frac{10 - 15/b}{7}\phi \right) \boldsymbol{D}^\infty \cdot \boldsymbol{D}^\infty \right] \tag{2.37}$$

or, in dimensional variables:

$$\langle \boldsymbol{\tau} \rangle = 2\eta_0 \left(1 + \frac{5}{2}\phi \right) \boldsymbol{D}^\infty + \alpha_0 \left(1 + \frac{5}{2}\phi \right) \boldsymbol{A}^\infty + \beta_0 \left(1 + \frac{10 - 15\alpha_0/\beta_0}{7}\phi \right) \boldsymbol{D}^\infty \cdot \boldsymbol{D}^\infty \tag{2.38}$$

Equation (2.38) clearly shows that a dilute suspension of rigid spheres in a second order fluid is itself a second order fluid (see Eq. (2.1)) with new constitutive parameters η, α, and

β depending on η_0, α_0, and β_0, and (linearly) on ϕ. These equations represent the generalization of the Einstein result to the case of a SOF suspending medium. Equation (2.38) differs from the very recent prediction for bulk stress as derived in [13]. Indeed, it turns out that the coefficient of $\boldsymbol{A}^\infty$ in Eq. (2.38) coincides with that given in [13], whereas the coefficients of $\boldsymbol{D}^\infty \cdot \boldsymbol{D}^\infty$ do not agree.

In the following Sections, we proceed to a numerical validation of our own results for pressure and velocity fields, and for the local stress tensor. Afterwards, the perturbative expressions are used to predict experimental observables (bulk rheological properties).

2.6 The numerical analysis

In this Section, the single sphere problem is studied by numerical analysis, as follows. First, the order Wi problem is addressed, by solving the mass and momentum balance equations given in Section 2.3, namely Eqs. (2.14) and (2.15), with boundary conditions given by Eqs. (2.16), (2.17), and (2.18). The obtained numerical solutions are then directly compared with the analytic predictions for p_{SOF} and $\boldsymbol{v}_{SOF}$ given in Section 2.4. Secondly, the complete (i.e., up to order Wi) mass and momentum balance equations, Eqs. (2.2) and (2.3), are solved. In this case, to compare the analytic perturbation analysis with the numerical results, the simulations must be run for *small* Wi and, correspondingly, the boundary conditions must be those pertaining up to the order Wi solution. Hence, Eqs (2.4) and (2.5) hold at the external boundary of the integration domain, and, at $r = 1$, it is $\boldsymbol{v} = \frac{1}{2}(\nabla \boldsymbol{v}^\infty - \nabla \boldsymbol{v}^{\infty T}) \cdot \boldsymbol{u}$. The latter condition stems from Eq. (2.13) and Eq. (2.18).

The 3D flow problem has been solved with two different commercial codes (Femlab© and Polyflow©) on a cubic cell containing a single sphere. It has been verified that the numerical predictions from both codes are essentially coincident. The flow field at infinity is of course imposed on the cube boundaries. The cell dimension was so chosen as to give cell invariant pressure and velocity fields. The results presented here were calculated with a cube side twenty times the sphere radius. (In order to optimize the computational effort, the symmetries pertaining to the imposed flow fields were exploited, see below.) Tetrahedric meshes were chosen, with a higher density of nodes close to the sphere, where larger gradients are expected. Convergence was achieved with a total number 4488 elements. In both codes we used continuous quadratic interpolation for the velocity, and continuous linear interpolation for pressure. This choice satisfies the so called LBB-condition [41], and avoids spurious oscillations in the pressure field. With Femlab, it was not necessary to discretize stress tensor because the stress components for SOF constitutive equation were explicit functions of velocity and pressure fields. This feature might give some convergence problems for high Weissenberg number values, but for the low Wi-values of interest here the FemLab code converged without problems. In PolyFlow, an DEVSS interpolation for stress tensor combined with streamline-upwinding [42] was adopted. This allowed for a continuous linear interpolation for the stress tensor components. With both codes, the discretized non-linear system was solved by a Newton-Raphson method, with relative tolerance 10^{-4}, and the resulting linear algebraic system at any iteration step was solved

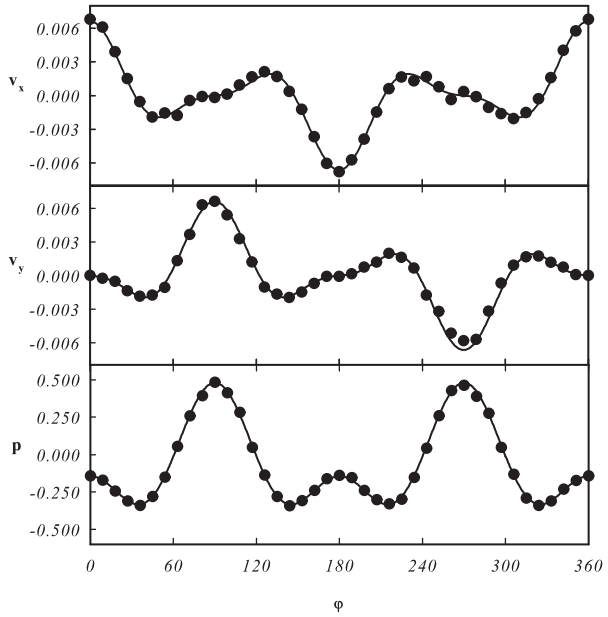

Figure 2.1: SOF velocity components and pressure in the shear plane at $r = 2$ for $b = -7$. The angle φ describes a counterclockwise rotation around the sphere in the shear plane. Lines are analytical predictions, symbols from numerical simulations.

by Gaussian elimination technique.

Two different velocity fields imposed at infinity were considered, namely, shearing and uniaxial elongational flows, which represent the most commonly studied rheological flows. The shear flow corresponds to a velocity gradient at infinity with only one nonzero component $\nabla \boldsymbol{v}^{\infty}_{xy} = 1$. Uniaxial elongation is given by $\nabla \boldsymbol{v}^{\infty}_{xx} = -2\nabla \boldsymbol{v}^{\infty}_{yy} = -2\nabla \boldsymbol{v}^{\infty}_{zz} = 1$. In shear, the numerical calculations were actually performed on one half of the cubic cell only. In elongation, only one eight of the cell was used. As it will be shown below, very good agreement is found between the analytical and the numerical predictions.

2.6.1 Shear flow

A first example of comparison between analytic and numerical results is presented in Figure 2.1, for the p_{SOF} and $\boldsymbol{v}_{SOF}$ fields in shear flow, for $b = -7$. Specifically, the pressure, and the v_x, v_y components in the shear plane at $r = 2$ are plotted. The angle φ goes counterclockwise from the imposed velocity direction (the x axis).

An excellent agreement is found between analytical and numerical predictions for all the three quantities. We have found a similar quantitative agreement (and also for the v_z component) throughout the cubic cell. In Figure 2.2, as an example, the pressure and the v_x component are plotted (for the same $b-$value as in Figure 2.1) as a function of the radial coordinate, along the bisectrix of the first quadrant of the shearing plane. Again,

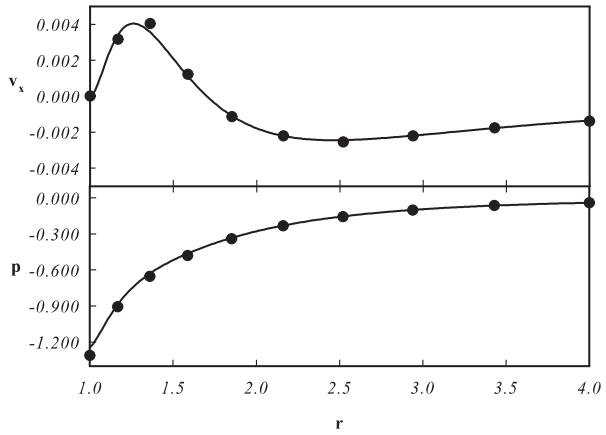

Figure 2.2: Radial profile of SOF velocity component and pressure along the bisectrix of the first quadrant of the shear plane for $b = -7$. Lines are analytical predictions, symbols are numerical results.

the agreement is very good.

In Figure 2.1 and Figure 2.2 only the SOF fields were plotted. We now consider the complete local stresses, i.e., inclusive of both the Newtonian (Einstein) and the SOF contributions.

In Figure 2.3 the local complete first normal stress difference $N_1 = T_{xx} - T_{yy}$ is shown, at the intersection of the sphere with the shear plane, for $Wi = 0.15$, $b = -7$, and

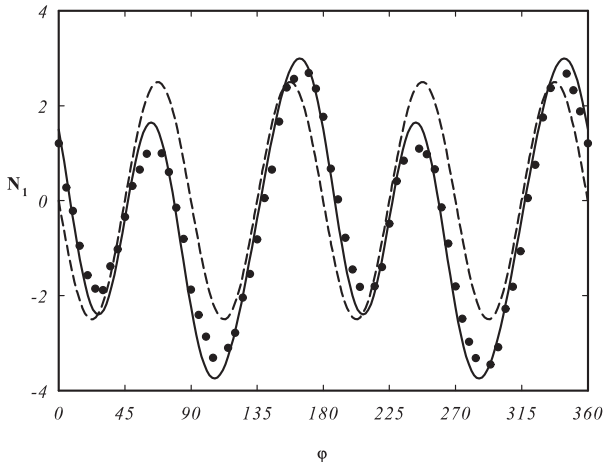

Figure 2.3: The local N_1 at $r = 1$ in the shear plane. Dashed line is the Newtonian analytical prediction; Solid line and dots are analytical and numerical results, respectively, for the viscoelastic case (for $Wi = 0.15$ and $b = -7$).

$\phi = 0.05$. Both the analytical prediction (solid line) and the numerical results (dots) are reported. For the sake of comparison, also the local N_1 of the Newtonian case is illustrated (dashed line). Indeed, a nonzero local N_1 does exist for the Newtonian case as well. The Newtonian minimum and maximum are found in the first quadrant of the shear plane, at $\frac{\pi}{8}$ and $\frac{3\pi}{8}$, respectively. The Newtonian N_1 field is $\frac{\pi}{2}$ periodic around the vorticity axis z (a 4-fold symmetry axis). Because of these symmetry properties, the bulk first normal stress difference $\langle N_1 \rangle$ for the Newtonian suspension is nil, as it is well known, even though nonzero local normal stresses exist close to the sphere.

Regarding the complete stress, it is apparent that the analytical and numerical predictions are in good agreement. Concerning the small discrepancies around maxima and minima, it should be remarked that $Wi = 0.15$ represents a quite large value in considering comparison with a perturbative solution. The composition of the Newtonian and SOF terms has a significant effect on the N_1 field symmetries. Indeed, the vorticity axis becomes now a 2-fold symmetry axis. The appearance of relative minima and maxima should be noticed, together with a displacement in their angular positions with respect to the Newtonian case. Of course, these angular positions depend on the imposed value of Wi.

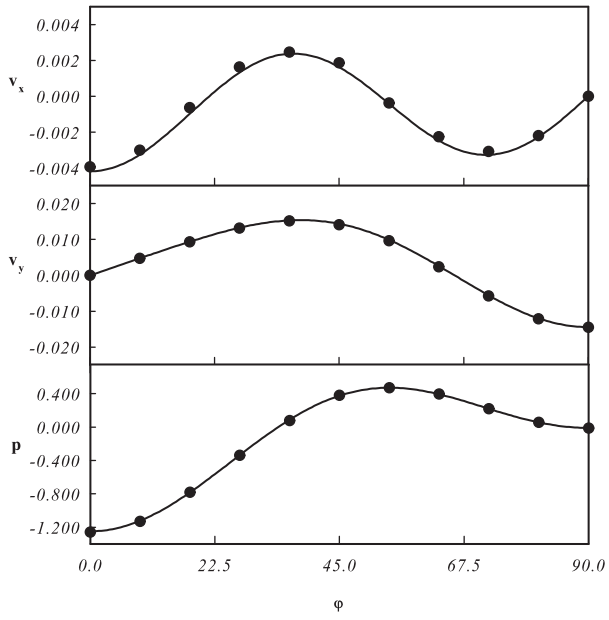

Figure 2.4: Uniaxial elongational flow with x as drawing axis. SOF velocity components and pressure in the first quadrant of the $xy-$plane at $r = 2$ for $b = -7$. The angle φ describes a counterclockwise rotation from the x axis. Lines are analytical predictions, symbols from numerical simulations.

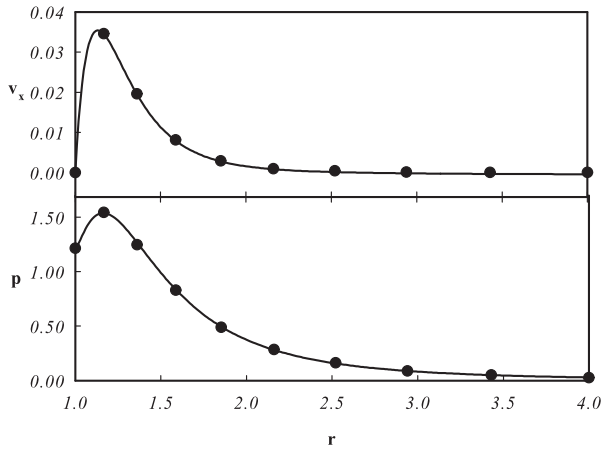

Figure 2.5: Radial profile of SOF velocity component and pressure along the bisectrix of the first quadrant of xy plane for $b = -7$ in the case of uniaxial elongational flow. Lines are analytical predictions, symbols are numerical results.

2.6.2 Uniaxial elongational flow

Figure 2.4 show the p_{SOF} and $\boldsymbol{v}_{SOF}$ fields in uniaxial elongational flow for $b = -7$. The pressure, and the v_x, v_y components in the xy plane at $r = 2$ are plotted. (Note that x is the draw direction.) Again, the angle φ goes counterclockwise from the x axis.

Also in the elongational case, an excellent agreement is found for all the three quantities. Figure 2.5 confirms such agreement also at various distances from the sphere, along the bisectrix of the first quadrant of the xy plane.

Figure 2.6 shows the complete local elongational stress field $T_{xx} - T_{yy}$, i.e., inclusive of both the Newtonian (Einstein) and the SOF contributions, at $r = 1$, for $Wi = 0.15$, $b = -7$, and $\phi = 0.05$. The numerical data just cover the first quadrant in the xy plane, since, for the elongational flow, simulations were run in one eight of the cubic cell. In the Newtonian case the maximum is found at 45° in the xy plane. For the complete stress, the maximum is enhanced, and angularly displaced towards the elongation axis. The numerical predictions show an excellent agreement with the analytical ones, even at this rather large $Wi-$value, with only minor discrepancies around the maximum.

2.7 Predictions for bulk rheology

The bulk constitutive equation is obtained by properly averaging the local stresses, see Eq. (2.32). In what follows, we will discuss some relevant rheological macroscopic quantities pertaining to the dilute suspension as a whole. Analytical predictions will be compared with numerical results obtained by numerically evaluating the integrals in Eqs. (2.33) and (2.34) with fourth order quadrature formulas.

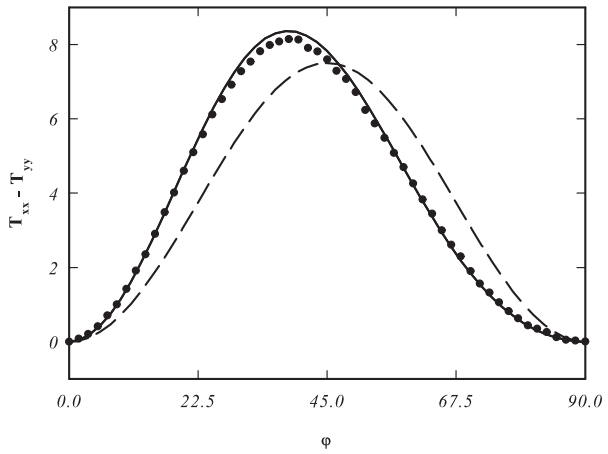

Figure 2.6: Local elongational stress field for a SOF suspending liquid at $r = 1$. Dashed line is the Newtonian analytical prediction; Solid line and dots are our analytical and numerical results, respectively, for the viscoelastic case (for $Wi = 0.15$ and $b = -7$).

The bulk first normal stress difference in shear is analytically calculated from Eq. (2.37) as

$$\langle N_1 \rangle = 2Wi \left(1 + \frac{5}{2}\phi\right) \tag{2.39}$$

showing how elastic effects depend on ϕ. The first normal stress difference of the Second Order Fluid is increased by the presence of the spheres. Notice also that $\langle N_1 \rangle$ does not depend on the constitutive parameter b. Equation (2.39) coincides with the prediction in [13].

Figure 2.7 shows the nondimensional first normal stress difference $\langle N_1 \rangle$ versus Wi at a volume fraction $\phi = 0.05$. Dashed line represents SOF with no inclusions, solid line is the new prediction (see Eq. (2.39)), and the symbols are the results from numerical calculations. The agreement between analytical and numerical prediction is excellent. Very minor discrepancies appear with increasing Wi, as already mentioned, in view of the perturbative nature of the theory. At $\phi = 0.05$, the relative difference in $\langle N_1 \rangle$ between filled and pure second order fluid is above 10%. It is worth remarking that the chosen value of volume fraction ($\phi = 0.05$) is most probably close to the border of the dilute regime, both for Newtonian and (even more so) for viscoelastic suspending liquids. The value adopted for ϕ in Figure 2.7 was chosen merely to improve figure clarity.

The analytical prediction for the second normal stress difference $\langle N_2 \rangle \equiv \langle T_{yy} \rangle - \langle T_{zz} \rangle$ from Eq. (2.37) is

$$\langle N_2 \rangle = -Wi \left(2 + \frac{b}{4} + \frac{125 + 10\,b}{28}\phi\right) \tag{2.40}$$

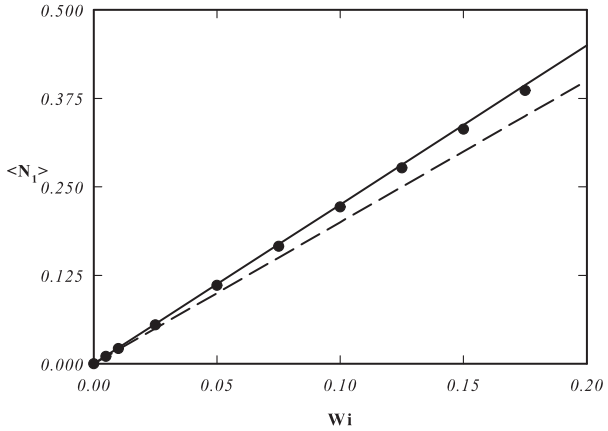

Figure 2.7: Shear flow: The bulk first normal stress difference versus Wi for $\phi = 0.05$ and $b = -7$. Dashed line is pure SOF, solid line from perturbative theory (Eq. 2.39), symbols from numerics.

Notice that $\langle N_2 \rangle$ does depend on the constitutive parameter b. Equation (2.40) shows an increase (in absolute value) with ϕ with respect to the pure SOF, for any b value. Again, good agreement between analytical and numerical results is found, see Figure 2.8.

In the Figure, also the analytical $\langle N_2 \rangle$-prediction by Koch and Subramanian [13] is shown. Our numerical results clearly indicate that Eq. (2.40) is in fact correct.

As usually done [17], it proves convenient to report first and second normal stress differences as a function of the shear stress. From Eq. (2.38) we obtain (dimensional

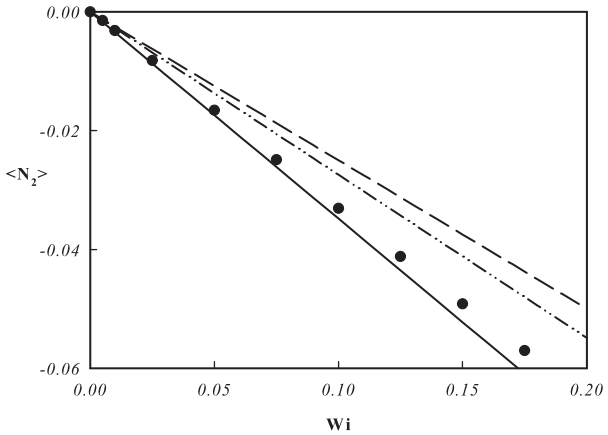

Figure 2.8: Shear flow: The bulk second normal stress difference versus Wi for $\phi = 0.05$ and $b = -7$. Dashed line is pure SOF, solid line from our perturbative theory (Eq. 2.40), symbols from numerics. Dot-dashed line is the analytical prediction by Koch.

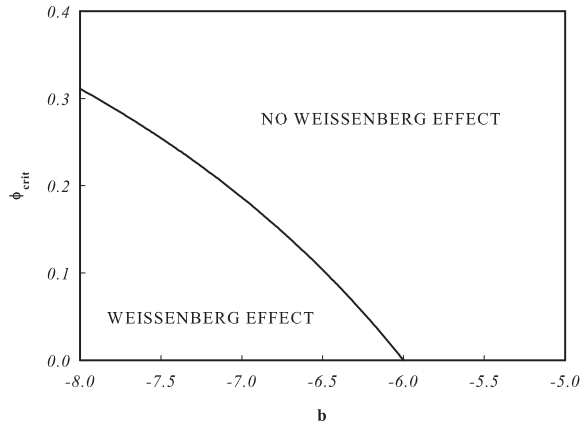

Figure 2.9: Existence of Weissenberg effect in a viscoelastic suspension. The line is $\phi_{cr} = \frac{14(6+b)}{15(2+b)}$ as deduced from Eq.2.43 in the text.

quantities):

$$\langle N_1 \rangle = -2\frac{\alpha_0}{\eta_0^2}\left[1 - \frac{5}{2}\phi\right]\langle T_{xy}\rangle^2 \tag{2.41}$$

$$\langle N_2 \rangle = 2\frac{\alpha_0}{\eta_0^2}\left(1 + \frac{\beta_0}{8\alpha_0} - \frac{155 + 25\,\beta_0/\alpha_0}{56}\phi\right)\langle T_{xy}\rangle^2 \tag{2.42}$$

It is readily seen from these equations that, at any fixed shear stress, the first normal stress difference decreases with ϕ, whereas the second normal stress difference increases. Both these features are in qualitative agreement with experimental findings [31, 17, 19]. The quantitative comparison with data of [17] turns out to be very good even at volume fractions well beyond the dilute limit [14, 15]. A word of caution is in order here, however, because there are limited data available in the literature, and also the error on the normal stress difference measurements is often substantial.

A further prediction of the theory presented here concerns the so called Weissenberg effect, i.e., the climbing of a viscoelastic fluid onto a rotating rod [34]. It is well known that this phenomenon is linked to the ratio $\Psi \equiv -\frac{N_2}{N_1}$ in shear flow. In the limit of vanishing Wi, Ψ is a purely constitutive quantity: for pure SOF it is $\Psi = 1 + \frac{b}{8}$. The Weissenberg climbing is found when $\Psi < \frac{1}{4}$, i.e., for $-8 < b < -6$. As it was shown in the above, the presence of spheres in a SOF alters the bulk normal stress differences, hence Ψ. Indeed, it is:

$$\Psi = 1 + \frac{b}{8}\left[1 - \left(\frac{15}{14} + \frac{15}{7\,b}\right)\phi\right] \tag{2.43}$$

It so turns out that, at any fixed $b-$value, there exists a critical volume fraction ϕ at which the Weissenberg effect is suppressed. Such a critical value is shown in Figure 2.9

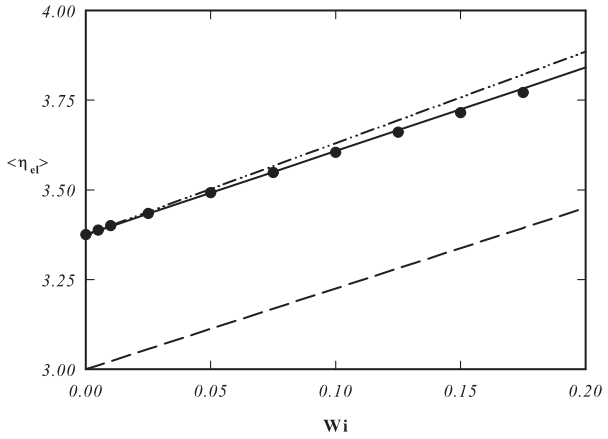

Figure 2.10: The bulk elongational viscosity versus Wi for $\phi = 0.05$ and $b = -7$. Dashed line is pure SOF, solid line from our perturbative theory (Eq. 2.44), symbols from numerics. Dot-dashed line is the analytical prediction by Koch.

as a function of b. This prediction is in qualitative agreement with experimental results reported by [43]. (Strictly speaking, Eq. (2.43) is valid for low ϕ only.)

We now pass to the extensional flow. The bulk nondimensional extensional viscosity $\eta_{el} = \langle T_{xx} \rangle - \langle T_{yy} \rangle$ in uniaxial elongational flow is given by:

$$\eta_{el} = 3\left(1 + \frac{5}{2}\phi\right) - 3Wi\left[1 + \frac{b}{4} + \frac{5}{28}\left(11 + 2\,b\right)\phi\right] \tag{2.44}$$

When the suspending fluid is Newtonian, the classical Einstein result is recovered, namely, that the Trouton ratio (elongational to shear viscosity) is three. With a second order fluid as the suspending liquid, the nondimensional elongational viscosity is linear in Wi, and depends on both b and ϕ. Figure 2.10 shows the extensional viscosity as a function of Wi. The lines are analytic predictions for the pure SOF (dashed) and the suspension (solid), with $\phi = 0.05$ and $b = -7$. The analytical prediction by Koch and Subramanian [13] is also reported in Figure 2.10 (dot-dashed line). Symbols are the results of numerical computations, showing excellent agreement with our theory, Eq. (2.44), throughout the $Wi-$range. The elongational viscosity is increased by the presence of the filler, as reported from experiments (see [31]). In Figure 2.10 the increase is around 10% up to $Wi \sim 0.2$. We are not aware of experimental data to quantitatively validate these predictions.

In the context of experimental extensional rheometry of filled viscoelastic systems, it has been proposed to quantify the effect of Wi (at a fixed loading) through the instantaneous relative viscosity $\lambda\left(t\right) \equiv \frac{\eta_{el}(Wi,\phi,t)}{\eta_{el}(Wi=0,\phi,t)}$. Within the present approach, we can only consider this quantity at the steady state, i.e., for $t \to \infty$. From Eq. (2.44) above, we calculate:

$$\lambda = 1 - Wi\left(1 + \frac{b}{4} - \frac{30 + 15b}{56}\phi\right) \tag{2.45}$$

From Eq. (2.45), we find that, at a fixed loading, λ increases with Wi. Conversely, at a fixed $Wi-$value, λ decreases with ϕ. Both these predictions are in qualitative agreement with experimental measurements (e.g. [18]) of instantaneous λ.

2.8 Conclusions

The problem of a single rigid sphere immersed in a viscoelastic liquid subjected to a linear flow field at infinity is solved, in the limit of low $Wi-$number. The stress tensor of a dilute suspension of rigid spheres in a viscoelastic liquid was analytically determined, by applying the averaging procedure proposed by [32, 9]. Analytic perturbative results were validated by computational fluid dynamics simulations. The numerical procedure was based on finite element schemes for fully 3D geometry. The numerical approach unequivocally confirmed the validity of the analytical expressions for local velocity and pressure fields Eqs. (2.21) – (2.31). An excellent agreement was also found between our analytic predictions for the bulk stress tensor, Eq. (2.38), and the numerical predictions for both shear and uniaxial elongational flows. Though very similar to our own equations, the analytical expression for the bulk stress tensor of the suspension as given by [13] slightly disagrees with the numerical results.

The analytical expression for the stress tensor is the generalization of the classical Einstein result [8] to the case of a viscoelastic suspending liquid, which is here considered as a SOF. The SOF constitutive equation represents the common asymptote of all viscoelastic simple liquids, but at vanishing flow rates. Nevertheless, the obtained predictions are in good qualitative agreement with the available experimental data.

The theory is limited to dilute conditions and to small Weissenberg number where the Second Order Fluid theory is valid. It seems worthwhile considering other viscoelastic constitutive equations, to abandon the asymptotic SOF theory, aiming at solving more realistic situations through numerical simulations. The extension to finite Weissenberg number is carried out in Chapter III.

Chapter 3

The analysis at finite Weissenberg number

3.1 Introduction

The Second Order Fluid analysis, carried out in Chapter II, is only valid for small Weissenberg number, when the flow is slow and slowly varying. Indeed, the SOF behavior can be considered as an asymptote (for vanishing Wi) for other viscoelastic constitutive equations [33].

In systems of practical interest, the external imposed flow is generally not slow and abrupt changes in the geometry, where the material flows in, lead to high gradients in velocity field. In such a case, more realistic viscoelastic constitutive equations need to be considered to model the suspending fluid since the SOF theory does not predicted well the material behavior. However, due to the mathematical complexity of the equations to be solved, an analytical theory cannot be assessed anymore, and numerical simulations are required. In this Chapter, the bulk rheology and the fluid dynamic of a dilute suspension of buoyancy-free rigid non-Brownian spheres in a viscoelastic matrix for finite Weissenberg number are studied. An external simple shear flow is considered since, in such a case, as discussed later, interesting experimental phenomena occur.

In general, externally imposed flow fields determine forces and torques on the particles, resulting in their translations and rotations. Diluteness of the suspension implies that the particles do not feel each other. Hence, the motion of a particle only depends on the particle characteristics, i.e., shape, surface properties, boundary conditions, and on the rheological features of the suspending liquid.

Under steady shear flow, the sphere translates in the flow direction, while rotating around the vorticity axis. Thus, in a frame translating with the sphere center, the sphere just rotates in time with a constant angular velocity, ω. Einstein [8] demonstrated that, in a Newtonian suspending liquid and under no-slip conditions, $\omega = \dot{\gamma}/2$, $\dot{\gamma}$ being the externally imposed shear rate. This simple result stems from a torque balance at the sphere surface, whereby the torque on the sphere is only due to the flow field (the so called torque-free

condition).

In the case of a viscoelastic suspending liquid, the analytical results reported in Chapter II and in [14, 15, 16] show that, in the limit of the SOF theory, the angular velocity remains the same as in the Newtonian case.

In experiments by Mason and coworkers [44, 45, 46] on the rotational motion of single rigid particles in Couette flow of a shear-thinning and a viscoelastic fluid, the rate of rotation of isolated particles was found to be identical to that observed in Newtonian fluids. Since the experiments were limited to slow flows, agreement with theoretical predictions for SOF was, in fact, expected.

In a recent paper, Astruc et al. [20] experimentally analyzed several suspensions, of both nearly spherical particles and agglomerates in viscoelastic liquids during steady state shear flow, abandoning the slow flow limit. In all cases, particle rotation is observed to slow down as the shear rate increases. A similar slowing down in angular velocity is also found in recent numerical simulations by Hwang et al. [27], for a 2D suspension of disks in an Oldroyd-B liquid. We are not aware of any prediction for the 3D case.

Our work is focused, then, on 3D numerical simulations of the single sphere shear problem for various non-Newtonian suspending liquids. The simulations are performed by means of the finite element method and the torque-free condition is imposed through constraints on the sphere surface. The effect of viscoelasticity on the angular velocity of the rotating sphere is examined for Weissenberg number up to 2.5, hence well beyond the slow flow limit. The selection of constitutive equations here adopted illustrates the relative weight of shear thinning and normal stresses on the slowing down of the sphere angular velocity.

Few experimental data on the rheological properties of suspensions of noncolloidal spheres in viscoelastic liquids can be found in the literature [47, 48, 43, 49, 17, 19]. One rather general conclusion is that the first and (magnitude of) second normal stress differences increase as the solid fraction increases. Most of the experiments, however, were carried out at relatively high solid loadings.

This Chapter is organized as follows: in Section 3.2 the mathematical model is introduced and the details of the numerical procedure implemented are described. In particular, in Sections 3.2.1 and 3.2.2 the governing equations and the viscoelastic constitutive models are presented. Then, the weak form of the problem is derived (Section 3.2.3) and the spatial and temporal discretization is discussed (Section 3.2.4). In Section 3.3 convergence tests are carried out (mesh resolution, size of the domain, time step). The results of our simulations are presented in Section 3.4. The rotation of the sphere is firstly discussed (Section 3.4.1) by focusing the attention on the influence of the constitutive model as well as the Weissenberg number. In Section 3.4.2 the rheological behaviour is studied and the bulk rheological quantities such as viscosity, first and second normal stress differences are derived. Finally, in Section 3.5 the conclusions are discussed.

3.2 Modeling

3.2.1 Governing equations

The fluid dynamic problem of a single sphere in an externally imposed flow field, under isothermal conditions, consists of the continuity (mass balance) and momentum balance equations. Incompressibility, negligible inertia, and buoyancy free conditions are also assumed. The balance equations then read:

$$\nabla \cdot \boldsymbol{u} = 0 \tag{3.1}$$

$$-\nabla p + \nabla \cdot \boldsymbol{\tau} = \mathbf{0} \tag{3.2}$$

where p is the pressure, $\boldsymbol{u}$ is the velocity, and $\boldsymbol{\tau}$ is the constitutive extra stress tensor. The extra stress tensor, for a single-mode model, is given by:

$$\boldsymbol{\tau} = G(\boldsymbol{c} - \boldsymbol{I}) \tag{3.3}$$

where $\boldsymbol{c}$ is the conformation tensor, $G = \eta_0/\lambda$ with η_0 the zero shear viscosity and λ the polymer relaxation time. Notice that for a purely viscous model, Eqs. (3.1) and (3.2) are sufficient to solve the problem, since the stress tensor is an explicit function of pressure and velocity. On the contrary, a viscoelastic constitutive model needs an extra equation for the stress tensor (or conformation tensor). The equations of the models used will be presented in Section 3.2.2. Boundary conditions are assigned at infinity and on the sphere surface. The far-field condition corresponds to the undisturbed shear flow:

$$\begin{aligned} &p \to p^{\infty} \\ &\boldsymbol{u} \to \nabla \boldsymbol{u}^{\infty} \cdot \boldsymbol{r} \end{aligned} \tag{3.4}$$

with p^{∞} a constant pressure, $\nabla \boldsymbol{u}^{\infty}$ the imposed velocity gradient, and $\boldsymbol{r}$ the position vector from the sphere center.

Here, the imposed velocity field at infinity is stationary simple shear flow, and we call x the flow direction, y the velocity gradient direction, and z the vorticity direction. Thus, at infinity, the imposed velocity gradient is $\nabla \boldsymbol{u}^{\infty}_{xy} = \dot{\gamma}$, the other components being nil, with $\dot{\gamma}$ the shear rate.

No slip boundary conditions are imposed at the sphere surface $r = R$. We also assume that the sphere is torque-free, or "freely rotating" [35, 36], i.e., its rotation is only due to the motion of the surrounding fluid. Thus, the torque-free boundary condition at $r = R$ is:

$$\int_{S_p} \boldsymbol{r} \times \boldsymbol{\sigma} \cdot \boldsymbol{n} \, dA = \mathbf{0} \tag{3.5}$$

where $\boldsymbol{n}$ is the normal at the sphere surface S_p, the tensor $\boldsymbol{\sigma}$ is $\boldsymbol{\sigma} = -p\boldsymbol{I} + \boldsymbol{\tau}$, and the integral of the local torque spans the sphere surface. Due to the symmetry of the imposed shearing flow, only the vorticity component z of Eq. (3.5) is significant (the other two

components being identically zero). In fact, the form of the velocity at the sphere surface is known, and can be written as:

$$\boldsymbol{u}(R) = \omega \boldsymbol{k} \times \boldsymbol{R} \tag{3.6}$$

$\boldsymbol{k}$ being the unit vector along z. The time-independent velocity $\boldsymbol{u}(R)$ in Eq. (3.6) is at any point on the sphere surface the tangential velocity of that point. Hence, $\boldsymbol{u}(R)$ is everywhere tangential to the surface, and parallel to the shear plane xy. The unknown angular velocity ω in Eq. (3.6) can then be determined through the z component of the torque-free condition, Eq. (3.5).

3.2.2 Constitutive equations

Aim of this work is to investigate how the viscoelastic properties of the suspending liquid affect the rotation of a suspended sphere in shear flow. Therefore, our choice of constitutive equations for the stress tensor $\boldsymbol{\tau}$ (see Eq. (3.2)) is so made as to highlight viscoelastic effects separately, i.e., viscosity thinning, and first and second normal stress differences (with or without thinning) are considered once at a time. Furthermore, since the presence of the inclusion leads to elongational flow components as well, the model predictions in such a flow have also an impact on the suspension properties.

The effect of shear thinning is considered first, through the purely viscous Bird-Carreau [50] constitutive equation:

$$\boldsymbol{\tau} = 2\frac{\eta_0}{(1 + 2\lambda^2 \boldsymbol{D} : \boldsymbol{D})^p}\boldsymbol{D} \tag{3.7}$$

where $\boldsymbol{D}$ is the deformation rate tensor and p fixes the shear thinning slope. Note that, in the case of pure shear flow, it is $2\boldsymbol{D} : \boldsymbol{D} = \dot{\gamma}^2$. Needless to say, the characteristic time in the Bird-Carreau equation does not relate to any time effect.

To describe normal stresses, the following three differential constitutive equations are thereafter considered (in parentheses, the corresponding equations in terms of $\boldsymbol{c}$ are reported):

$$\lambda \overset{\nabla}{\boldsymbol{\tau}} + \boldsymbol{\tau} = 2\eta_0 \boldsymbol{D} \qquad (\lambda \overset{\nabla}{\boldsymbol{c}} + \boldsymbol{c} - \boldsymbol{I} = \boldsymbol{0}) \tag{3.8}$$

$$\lambda \overset{\nabla}{\boldsymbol{\tau}} + exp\left[\frac{\epsilon\lambda}{\eta_0} Tr(\boldsymbol{\tau})\right]\boldsymbol{\tau} = 2\eta_0 \boldsymbol{D} \qquad (\lambda \overset{\nabla}{\boldsymbol{c}} + exp[\epsilon(Tr(\boldsymbol{c}) - 3](\boldsymbol{c} - \boldsymbol{I}) = \boldsymbol{0}) \tag{3.9}$$

$$\lambda \overset{\nabla}{\boldsymbol{\tau}} + \frac{\alpha\lambda}{\eta_0}\boldsymbol{\tau} \cdot \boldsymbol{\tau} + \boldsymbol{\tau} = 2\eta_0 \boldsymbol{D} \qquad (\lambda \overset{\nabla}{\boldsymbol{c}} + \boldsymbol{c} - \boldsymbol{I} + \alpha(\boldsymbol{c} - \boldsymbol{I})^2 = \boldsymbol{0}) \tag{3.10}$$

where $(\overset{\nabla}{})$ indicates the upper-convected time derivative:

$$\overset{\nabla}{\boldsymbol{\tau}} \equiv \frac{\partial \boldsymbol{\tau}}{\partial t} + \boldsymbol{u} \cdot \nabla \boldsymbol{\tau} - (\nabla \boldsymbol{u})^T \cdot \boldsymbol{\tau} - \boldsymbol{\tau} \cdot \nabla \boldsymbol{u} \tag{3.11}$$

Equation (3.8) is the UC Maxwell model [51], Eq. (3.9) the Phan Thien-Tanner (PTT) model [52, 53], and Eq. (3.10) is the Giesekus model (GSK) [54]. The latter two models contain each an additional parameter (ϵ and α, respectively), and $Tr(\cdot)$ represents the trace operator.

As it is well known, under steady state simple shear flow, the Maxwell model predicts a constant viscosity, a first normal stress difference N_1 quadratic in the shear rate, and no second normal stress difference N_2. In the PTT model, N_2 remains nil, whereas the viscosity and the first normal stress coefficient $\Psi_1 = N_1/\dot{\gamma}^2$ are both shear thinning, and decrease in values as ϵ increases. Finally, in the Giesekus model, both normal stress differences do exist. The viscosity and both normal stress coefficients, Ψ_1 and $\Psi_2 = -N_2/\dot{\gamma}^2$ are all shear thinning. At any given shear rate, the parameter α modulates the extent of the thinning. As α increases, the viscosity and Ψ_1 decrease in values, while Ψ_2 increases.

The analysis is carried out by making the above equations dimensionless, using λ as the characteristic time scale, and $\eta_0\dot{\gamma}$ as the scale for the stress. Then, the Weissenberg number, $Wi = \lambda\dot{\gamma}$ appears in all the equations. (Again, note that the Weissenberg number will be used for the Bird-Carreau model as well, but in this case Wi is just a dimensionless shear rate.) The Maxwell model is completely defined by Wi only, whereas in the other three models considered here one extra parameter has to be fixed (p, ϵ or α).

3.2.3 Weak form

Once a constitutive equation is selected for the extra stress tensor $\boldsymbol{\tau}$, the single sphere problem for shear flow consists in the determination of the pressure and velocity fields, plus the angular velocity of the sphere ω.

The 3D flow problem was solved by the finite element method on a cubic cell containing a single sphere (see Figure 3.1a). Since the sphere is located at the center of the cube, it rotates only, therefore we do not need to implement any moving mesh. Indeed, the sphere is just considered like a fixed surface of the domain. The rotation will be imposed through constraints, as discussed below.

For the symmetry of the problem, only one half ($z > 0$) of the full domain can be considered in order to optimize the computational effort (see Figure 3.1b). The flow field at infinity is of course imposed on the cube boundaries. It's important to point out that the boundary conditions imposed in such a way lead to the existence of two inflow sections on the cube boundaries (one-half of the $yz-$side for both positive and negative x values, i.e. the sections $\overline{ABCE}$ and $\overline{FGHI}$ in Figure 3.1b). As discussed below, the conformation tensor needs to be imposed on these sections.

The cell dimension was so chosen as to give cell invariant pressure and velocity fields. A test about the proper choice of the ratio between the cubic length and the sphere diameter is discussed in Section 3.3.1. A mesh with tetrahedral elements is chosen, with a higher density of elements close to the sphere, where larger gradients are expected. An example of the mesh used is depicted in Figure 3.2. As the zoom in the same figure clearly shows, finer elements surrounding the sphere surface becoming more and more coarse far from it.

The problem with Bird-Carreau model as constitutive equation is solved by means of

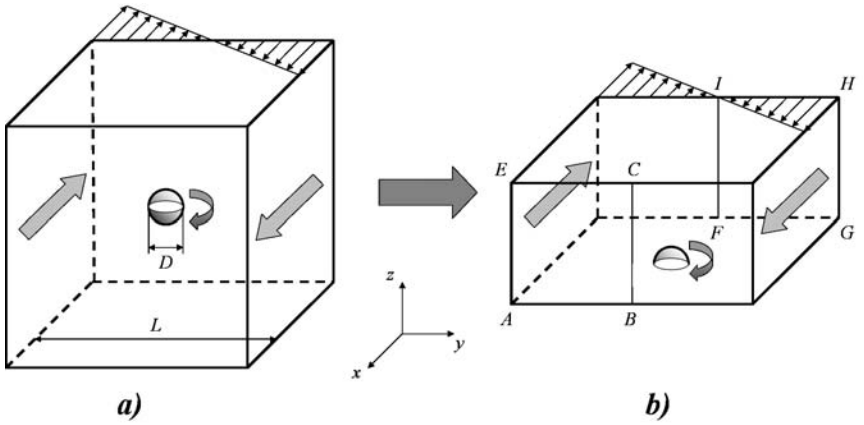

Figure 3.1: Geometric (a) and computational (b) domain.

a commercial software (Polyflow©) by using a standard velocity - pressure formulation (quadratic velocity and linear pressure). Upon discretization, a fully coupled non-linear system is linearized by the Newton-Rhapson method and the sparse linear system is solved by a frontal direct method based on Gaussian elimination. As it will be clear in the following, for this model only steady state case needs to be solved.

In order to deal with the viscoelastic models, the continuity and momentum equations (Eqs. (3.1) and (3.2)) need to be solved together with the constitutive one (Eqs. (3.8), (3.9) or (3.10)). However, in our numerical method, the momentum and continuity equations are decoupled from the constitutive equation, and, as discussed later, an implicit stress formulation is used. In this formulation the time-discretized constitutive equation is substituted into the momentum balance in order to obtain a Stokes like system (the stress tensor computed in the previous time step is used).

It is well known that the resultant system leads to convergence problems at relatively low Weissenberg number, if standard finite element discretization for the unknowns $(\boldsymbol{u}, p, \boldsymbol{\tau})$ is implemented. In order to improve the convergence at high Wi, stabilization techniques are required. In this regard, we discretized the momentum equation with the DEVSS formulation [42] by using in the constitutive equation the projected velocity gradient $(\boldsymbol{G})$ instead of $(\nabla \boldsymbol{u})^T$ (DEVSS-G formulation) [55]. The scheme is combined with the SUPG method [56] for the constitutive equation. In addition, we use the recently proposed log-conformation representation, which leads to a significantly improvement of numerical stability [57, 58]. According to this formulation, the original equation for the conformation tensor $\boldsymbol{c}$ is transformed to an equivalent equation for $\boldsymbol{s} = \log(\boldsymbol{c})$:

$$\dot{\boldsymbol{s}} = \frac{\partial \boldsymbol{s}}{\partial t} + \boldsymbol{u} \cdot \nabla \boldsymbol{s} = \boldsymbol{g}(\boldsymbol{\nabla u^T}, \boldsymbol{s}) \tag{3.12}$$

An expression for the function $\boldsymbol{g}$ can be found in [58]. Solving the equation for $\boldsymbol{s}$ instead of the equation for $\boldsymbol{c}$ leads to a substantial improvement of stability for high Weissenberg numbers.

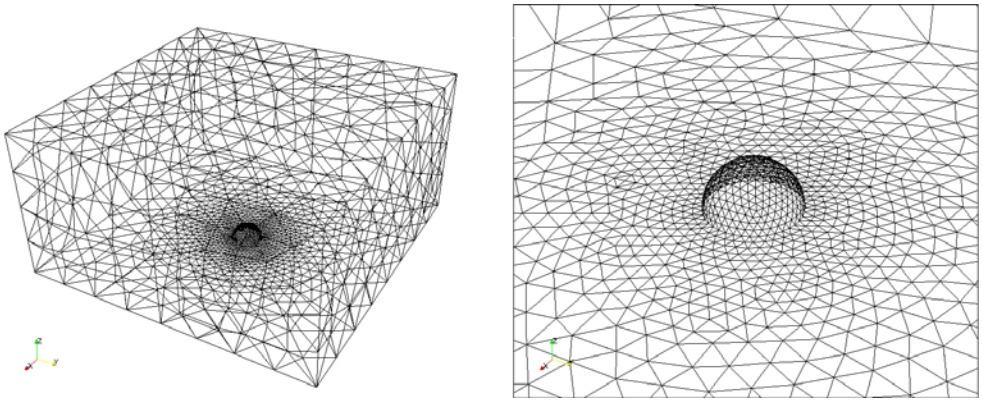

Figure 3.2: Example of mesh used in the computation (left) and a zoom of the zone close to the sphere surface.

Finally, the torque-free condition (Eq. (3.5)) is imposed through constraints on the sphere surface, by means of Lagrange multipliers. In this way, the sphere rotation is automatically calculated by solving the augmented system of equations, and no trial-and-error procedure is required.

The weak form of the system of equations (3.1), (3.2), (3.3) and the constitutive equation ((3.8), (3.9) or (3.10)) then reads: For $t > 0$, find $\boldsymbol{u} \in U, p \in P, \boldsymbol{s} \in S, \boldsymbol{G} \in H, \boldsymbol{\omega} \in \Re, \boldsymbol{\lambda} \in L^2(\partial S_p)$ such that:

$$-\int_V \nabla \boldsymbol{v}\, p\, dV + \int_V a(\nabla \boldsymbol{v})^T : \nabla \boldsymbol{u}\, dV - \int_V a(\nabla \boldsymbol{v})^T : \boldsymbol{G}^T\, dV + \langle \boldsymbol{v} - (\boldsymbol{\chi} \times \boldsymbol{r}), \boldsymbol{\lambda} \rangle_{\partial S_p} = -\int_V \boldsymbol{D}(\boldsymbol{v}) : \boldsymbol{\tau}\, dV, \quad (3.13)$$

$$\int_V q\, \nabla \cdot \boldsymbol{u}\, dV = 0, \quad (3.14)$$

$$\int_V \boldsymbol{H} : \boldsymbol{G}\, dV - \int_V \boldsymbol{H} : (\nabla \boldsymbol{u})^T\, dV = \boldsymbol{0}, \quad (3.15)$$

$$\int_V (\boldsymbol{S} + \tau \boldsymbol{u} \cdot \nabla \boldsymbol{S}) : \left(\frac{\partial \boldsymbol{s}}{\partial t} + \boldsymbol{u} \cdot \nabla \boldsymbol{s} - \boldsymbol{g}(\boldsymbol{G}, \boldsymbol{s}) \right) dV = \boldsymbol{0}, \quad (3.16)$$

$$\langle \boldsymbol{\mu}, \boldsymbol{u} - (\boldsymbol{\omega} \times \boldsymbol{r}) \rangle_{\partial S_p} = \boldsymbol{0}, \quad (3.17)$$

$$\boldsymbol{s} = \boldsymbol{s}_0 \quad \text{at } t = 0, \quad \text{in } V, \quad (3.18)$$

$$\boldsymbol{s} = \boldsymbol{s}|_{\phi=0} \quad \text{on inflow sections} \quad (3.19)$$

for all $\boldsymbol{v} \in U$, $q \in P$, $\boldsymbol{S} \in S$, $\boldsymbol{H} \in H$, $\boldsymbol{\chi} \in \Re$ and $\boldsymbol{\mu} \in L^2(\partial S_p)$, where U, P, S, G are suitable functional spaces. The τ parameter in Eq. (3.16) is given by $\tau = \beta h / 2U_e$, where β is a dimensionless constant, h is a typical size of the element and U_e is a characteristic velocity for the element. In our simulations, we have chosen $\beta = 1$ and for U_e we take the

average of the magnitude of the velocities in all integration points. In addition, a in the Eq. (3.13) is chosen equal to the viscosity, $a = \eta_0$. We take the initial value of $\boldsymbol{s}_0 = \mathbf{0}$, corresponding to zero initial stress. Finally, $\boldsymbol{s}|_{\phi=0}$ is the conformation tensor for a unfilled fluid in the same conditions as the suspension and generally is a function of time. In this way, we impose an unperturbed flow condition on the inflow sections of the domain (being sufficiently far from the sphere).

Notice that the angular velocity, ω, is treated as an additional unknown and is included in the weak form of momentum equation. Only the z-component of ω is set different to zero since, for the symmetry of the problem, the sphere can rotate around the vorticity axis only. The torque-free condition is imposed through the Lagrange multipliers, $\boldsymbol{\lambda}$, in each node of the sphere surface. Only the $x-$ and $y-$component of $\boldsymbol{\lambda}$ are set different to zero since the Lagrange multipliers act as constraints on the $x-$ and $y-$component of the sphere velocity, being the $z-$component always nil.

3.2.4 Discretization

For the discretization of the weak form, we use tetrahedral elements with continuous quadratic interpolation (P_2) for the velocity $\boldsymbol{u}$, linear continuous interpolation (P_1) for the pressure p, linear continuous interpolation (P_1) for the velocity gradient $\boldsymbol{G}$ and linear continuous interpolation (P_1) for the log-conformation tensor $\boldsymbol{s}$.

Regarding the time discretization, since we do not consider any solvent, an implicit stress formulation is required. Indeed, let us consider the DEVSS-G explicit stress formulation of the momentum and continuity equations at iteration $n+1$ if the solvent is taken into account:

$$-\nabla \cdot (2\eta_s \boldsymbol{D}(\boldsymbol{u}^{n+1})) + \nabla p^{n+1} - a\nabla \cdot (\nabla \boldsymbol{u}^{n+1} - \boldsymbol{G}^{n+1,T}) = \nabla \cdot \boldsymbol{\tau}(\boldsymbol{c}^{n+1}) \tag{3.20}$$

$$\nabla \cdot \boldsymbol{u}^{n+1} = 0 \tag{3.21}$$

$$-\nabla \boldsymbol{u}^{n+1} + \boldsymbol{G}^{n+1,T} = \mathbf{0} \tag{3.22}$$

where η_s is the solvent viscosity and $\boldsymbol{c}^{n+1}$ has already been computed from a previous time step. If $\eta_s = 0$, remembering that $\boldsymbol{G}^T = \nabla \boldsymbol{u}$, the system becomes singular and no update of the velocity field is possible. Instead of fully couple the system unknowns ($\boldsymbol{u}$, p, $\boldsymbol{G}$, $\boldsymbol{c}$), we can find an expression for $\boldsymbol{\tau}(\boldsymbol{c}^{n+1})$ which involves still unknown terms for the velocity $\boldsymbol{u}^{n+1}$. Let us recall, then, the explicit-Euler formulation of a general viscoelastic constitutive equation:

$$\frac{\boldsymbol{c}^{n+1}}{\Delta t} = \frac{\boldsymbol{c}^n}{\Delta t} - \boldsymbol{u}^n \cdot \nabla \boldsymbol{c}^n + \nabla \boldsymbol{u}^{n,T} \cdot \boldsymbol{c}^n + \boldsymbol{c}^n \cdot \nabla \boldsymbol{u}^n + \boldsymbol{f}(\boldsymbol{c}^n) \tag{3.23}$$

where $\boldsymbol{f}(\boldsymbol{c})$ is a function depending on the model. A dependence on $\boldsymbol{u}^{n+1}$ can be achieved in the following way:

$$\frac{\boldsymbol{c}^{*,n+1}}{\Delta t} = \frac{\boldsymbol{c}^n}{\Delta t} - \boldsymbol{u}^{n+1} \cdot \nabla \boldsymbol{c}^n + \nabla \boldsymbol{u}^{n+1,T} \cdot \boldsymbol{c}^n + \boldsymbol{c}^n \cdot \nabla \boldsymbol{u}^{n+1} + \boldsymbol{f}(\boldsymbol{c}^n) \tag{3.24}$$

In the models investigated in this work, a linear relationship between $\boldsymbol{\tau}$ and $\boldsymbol{c}$ holds (Eq. (3.3)) so the stress term in Eq. (3.20) can be written as:

$$\boldsymbol{\tau}(\boldsymbol{c}^{*,n+1}) = G\Delta t\left(-\boldsymbol{u}^{n+1}\cdot\nabla\boldsymbol{c}^{n} + \nabla\boldsymbol{u}^{n+1,T}\cdot\boldsymbol{c}^{n} + \boldsymbol{c}^{n}\cdot\nabla\boldsymbol{u}^{n+1}\right) + G\left(\boldsymbol{c}^{n} + \Delta t\boldsymbol{f}(\boldsymbol{c}^{n}) - \boldsymbol{I}\right) \tag{3.25}$$

Substituting this expression into the momentum equation (without solvent) leads to the implicit stress formulation:

$$\begin{aligned}\nabla p^{n+1} - a\nabla\cdot(\nabla\boldsymbol{u}^{n+1} - \boldsymbol{G}^{n+1,T}) - \nabla\cdot(G\Delta t(-\boldsymbol{u}^{n+1}\cdot\nabla\boldsymbol{c}^{n} + \\ \nabla\boldsymbol{u}^{n+1,T}\cdot\boldsymbol{c}^{n} + \boldsymbol{c}^{n}\cdot\nabla\boldsymbol{u}^{n+1})) = \nabla\cdot(G(\boldsymbol{c}^{n} + \Delta t\boldsymbol{f}(\boldsymbol{c}^{n}) - \boldsymbol{I}))\end{aligned} \tag{3.26}$$

$$\nabla\cdot\boldsymbol{u}^{n+1} = 0 \tag{3.27}$$

$$-\nabla\boldsymbol{u}^{n+1} + \boldsymbol{G}^{n+1,T} = \boldsymbol{0} \tag{3.28}$$

Finally, the time-stepping procedure can be stated as follows:

Initialization. At $t = 0$, the log-conformation tensor $\boldsymbol{s}$ is set to $\boldsymbol{0}$, representing a zero initial stress condition. No initial condition for the velocity is required since we neglect the inertia.

Step 1. The unknowns ($\boldsymbol{G}$, $\boldsymbol{u}$, p, ω) as well as the Lagrange multipliers ($\boldsymbol{\lambda}$) are found by solving the following system according to the implicit stress formulation:

$$\begin{aligned}&-\int_V \nabla\cdot\boldsymbol{v}\, p^{n+1}\,dV + \int_V a(\nabla\boldsymbol{v})^T : \nabla\boldsymbol{u}^{n+1}\,dV - \int_V a(\nabla\boldsymbol{v})^T : \boldsymbol{G}^{n+1,T}\,dV + \\ &G\Delta t\int_V (\nabla\boldsymbol{v})^T : (-\boldsymbol{u}^{n+1}\cdot\nabla\boldsymbol{c}^{n} + \nabla\boldsymbol{u}^{n+1,T}\cdot\boldsymbol{c}^{n} + \boldsymbol{c}^{n}\cdot\nabla\boldsymbol{u}^{n+1}))\,dV + \\ &\qquad\langle\boldsymbol{v} - (\boldsymbol{\chi}\times\boldsymbol{r}), \boldsymbol{\lambda}^{n+1}\rangle_{\partial S_p} = -\int_V \boldsymbol{D}(\boldsymbol{v}) : G(\boldsymbol{c}^{n} + \Delta t\boldsymbol{f}(\boldsymbol{c}^{n}) - \boldsymbol{I})\,dV,\end{aligned} \tag{3.29}$$

$$\int_V q\,\nabla\cdot\boldsymbol{u}^{n+1}\,dV = 0, \tag{3.30}$$

$$\int_V \boldsymbol{H} : \boldsymbol{G}^{n+1}\,dV - \int_V \boldsymbol{H} : (\nabla\boldsymbol{u}^{n+1})^T\,dV = \boldsymbol{0}, \tag{3.31}$$

$$\langle\boldsymbol{\mu}, \boldsymbol{u}^{n+1} - (\boldsymbol{\omega}^{n+1}\times\boldsymbol{r})\rangle_{\partial S_p} = \boldsymbol{0}, \tag{3.32}$$

Notice that, in Eq. (3.29), $\boldsymbol{c}^{n}$ is the conformation tensor evaluated in the previous time step.

Step 2. The log-conformation tensor at the next time step, $\boldsymbol{s}^{n+1}$, is evaluated by integrating the constitutive equation (3.16). A combined first-order Euler forward/backward scheme is used and Eq. (3.16) is replaced by the following time-discretized form:

$$\int_V (\boldsymbol{S} + \tau\boldsymbol{u}^{n+1}\cdot\nabla\boldsymbol{S}) : \left(\frac{\boldsymbol{s}^{n+1} - \boldsymbol{s}^{n}}{\Delta t} + \boldsymbol{u}^{n+1}\cdot\nabla\boldsymbol{s}^{n+1} - \boldsymbol{g}(\boldsymbol{G}^{n+1}, \boldsymbol{s}^{n})\right) dV = \boldsymbol{0}, \tag{3.33}$$

Table 3.1: Meshes used to check the spatial convergence

Mesh	N° elements	N° elements on sphere surface
A	2731	146
B	3547	203
C	4621	241
D	5558	300
E	6229	342
F	7861	405
G	9203	459

In both Step 1 and 2, an unsymmetric sparse linear system needs to be solved. We use the parallel direct solver PARDISO [59, 60, 61].

3.3 Convergence test

3.3.1 Mesh convergence

In order to check the spatial convergence of the numerical procedure described in Section 3.2, we performed different simulations by varying the mesh resolution. In addition, since the shear flow boundary conditions need to be imposed far from the sphere (unperturbed conditions), we check whether the ratio L/D used in our simulations is large enough, where L is the length of the cubic side of the computational domain, and $D = 2R$ is the sphere diameter.

The meshes used are summarized in Table 3.1. In Figure 3.3, the transient and steady state rotation rate of the sphere in a Maxwell fluid are reported for the different meshes used (for clarity, in the transient analysis only 4 mesh results are reported). The Weissenberg number is the highest used in this work ($Wi = 2.5$) and the other parameters of the simulations are: $\Delta t = 0.05$, $L/D = 10$, $\eta_0 = 1.0$, $\dot{\gamma} = 1$. It is clear from the figures that a spatial convergence is achieved when the mesh E is used.

Regarding the L/D ratio, to save memory and CPU time, it should be chosen as the smallest value still assuring unperturbed conditions on the cube boundaries. Then, we perform two simulations for $L/D = 10$ and $L/D = 20$ (in both cases we consider Maxwell fluid, $Wi = 2.5$, $\Delta t = 0.05$, $\eta_0 = 1.0$). The transient rotation rate and bulk viscosity (defined in Section 3.4.2) is depicted in Figure 3.4. The curves overlap so the box size does not affect the results. By decreasing L/D, more and more large deviations occur (not shown) and the sphere "feels" the presence of the boundary conditions imposed (just like a wall). In the following, $L/D = 10$ will be set and the particle radius is chosen equal to 1.

3.3.2 Convergence in time

Our numerical procedure is transient so the time step has to be chosen. The implicit scheme used allows to choose a relatively large time step (in terms of numerical stability). In Figure 3.5, the transient rotation rate is reported for different time steps (for a Maxwell fluid and $Wi = 2.5$, $\eta_0 = 1.0$). Notice that only the start-up phase is depicted, indeed no steady state is achieved yet. The curves, starting from 0.5, show a different trend up to a strain of 3-4 then they overlap. The major difference can be noticed after few time steps: the curve at $\Delta t = 0.05$ goes up and goes down, whereas with decreasing the time step, an asymptotic trend is found (with asymptote $\omega = 0.5$). However, since the maximum error (maximum deviation from the largest and smallest time step) is less than 2% and the steady state is unaffected, we choose $\Delta t = 0.05$ to speed up the simulations. Finally, notice also that the deviation showed in the figure refers to the highest Wi investigated and, if Wi is decreased, the discrepancy goes more and more down.

3.4 Results

In this Section the results of our simulations for shear flow are presented. First, the rotation of the sphere is investigated, and the influence of non-Newtonian behavior and viscoelasticity of the suspending fluid is analyzed. Then, the bulk rheological properties of the dilute suspensions are evaluated. In both cases, the transient results are shown before the steady state ones. Since the steady state is achieved at the end of the simulation, the number of time steps is dependent on the Weissenberg number.

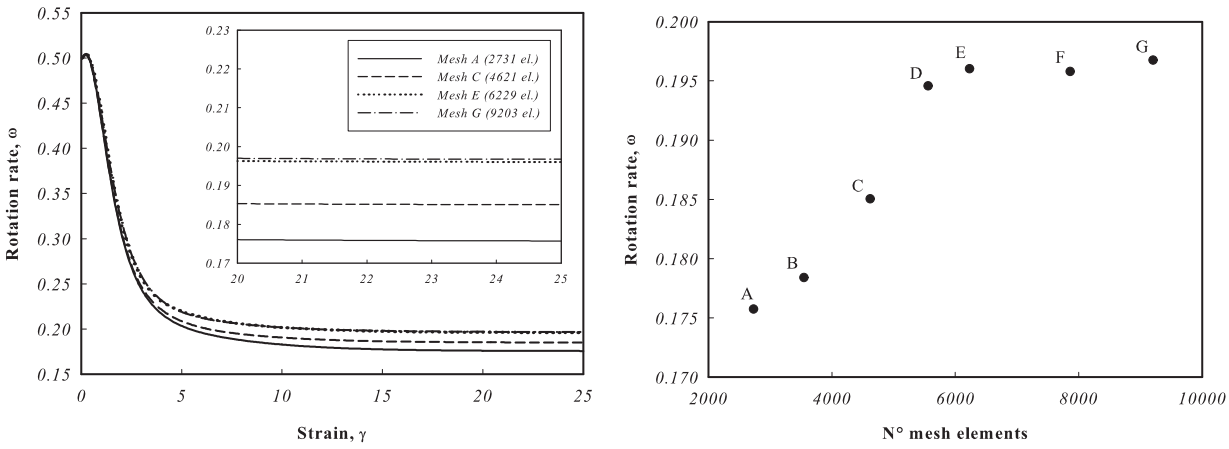

Figure 3.3: Transient (left) and steady state (right) rotation rate for different mesh resolutions (the letters refer to the meshes in Table 3.1).

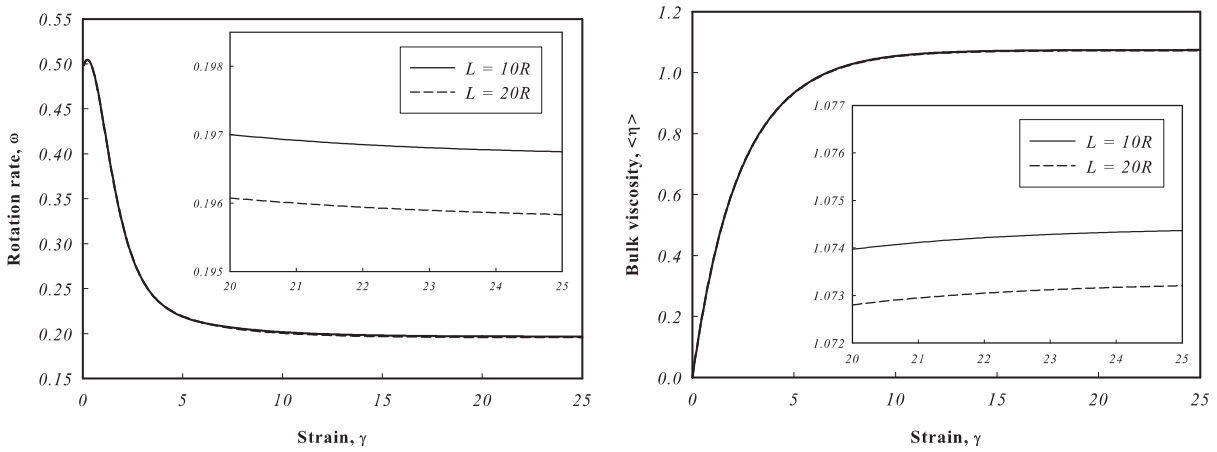

Figure 3.4: Transient rotation rate (left) and bulk viscosity (right) for two L/D ratios.

3.4.1 Rotation of the sphere

In Figure 3.6, the rotation rate of the sphere in a Maxwell fluid, ω, as a function of strain, $\dot{\gamma}t$, is reported, for different Weissenberg numbers. All the curves start from the Newtonian rotation rate, $\omega = 0.5$. By increasing the strain, the rotation rate decreases for every Wi investigated and, after a certain transient time depending on the Wi, a steady state is achieved. As previously discussed, the slight increase of the curves for small strains is due to the time step chosen. By reducing the time step, the curves start more and more asymptotically to $\omega = 0.5$, as should be in agreement with the SOF theory (see Chapter II).

The results for the PTT model ($\epsilon = 0.1$ and $\epsilon = 0.5$) are reported in Figure 3.7. Again,

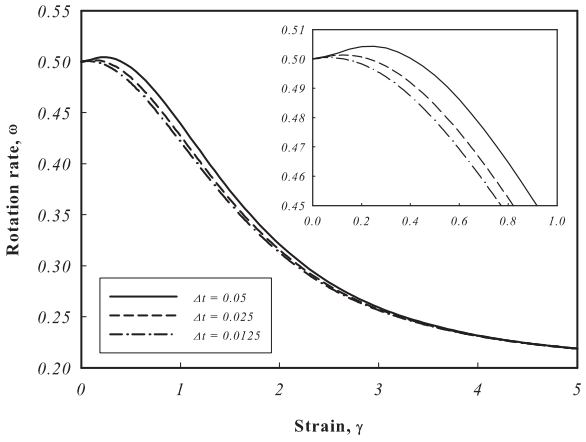

Figure 3.5: Transient rotation rate for different time steps.

starting from the Newtonian rotation rate, a decreasing trend is found, before achieving a steady state. However, in this case, an undershoot is found for high Wi, therefore a minimum in the rotation rate is attained. Notice that the undershoot is more pronounced if ϵ parameter is increased, indeed, for $\epsilon = 0$ the Maxwell behavior must be recovered. A similar trend is found for the Giesekus model as well (Figure 3.8). Also in this case, the undershoot appears for sufficiently high Wi and is more pronounced if α parameter is increased (for $\alpha = 0$ the Maxwell model is recovered). Finally, no start-up phase occurs if the Bird-Carreau model is considered, since the constitutive model does not include any dependence on time (it is just a Stokes problem with a different, independent of time, viscosity). For this model, only steady state results will be reported.

By taking the rotation rate values after the transient phase extinguished, we get steady state curves as a function of Weissenberg number. However, in order to make a qualitative comparison with the trend found in the experimental data, we consider the rotation period also ($T = 2\pi/\omega$).

It is well known that the rotation period T_{Newt} of a rigid sphere immersed in a Newtonian fluid under shearing flow can be written in terms of a Jeffery period as $T_{Newt} = 4\pi/\dot{\gamma}$ [8]. In what follows we use a normalized viscoelastic rotation period defined as [20]: $\overline{T} = T_{NN}/T_{Newt}$, where T_{NN} is the rotation period of the sphere in the viscoelastic medium. Of course, for vanishing Wi, $\overline{T}$ tends to unity. Experimental results [20] show that $\overline{T}$ is an increasing function of the Weissenberg number, i.e., the sphere slows down by increasing Wi. Figure 3.9 shows $\overline{T}$ and ω plotted as a function of Wi varying in the range [0, 2.5] for the Bird-Carreau purely viscous fluid, the Maxwell fluid, and the PTT fluid.

The numerical results for the Bird-Carreau model are indicated with the dotted line. Two values of the constitutive parameter p were considered ($p = 2$ and $p = 4$), to investigate the possible effect of different shear thinning slopes (see Eq. (3.7)). It turns out that the two curves exactly superimpose, and give $\overline{T} = 1$ throughout the explored Weissenberg range. Thus, a purely viscous, shear-thinning fluid as described with the Bird-Carreau model does

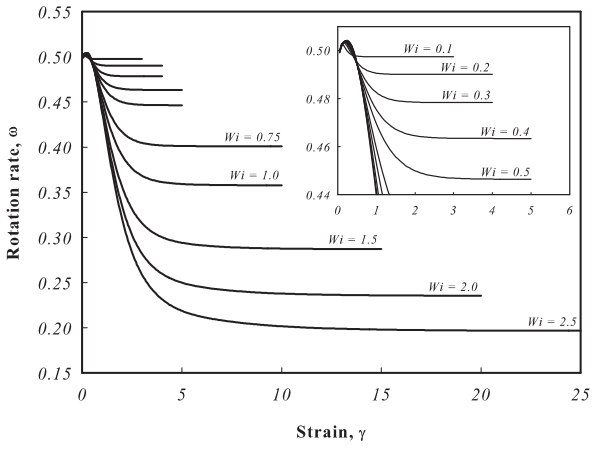

Figure 3.6: Transient rotation rate for Maxwell model for different Weissenberg numbers.

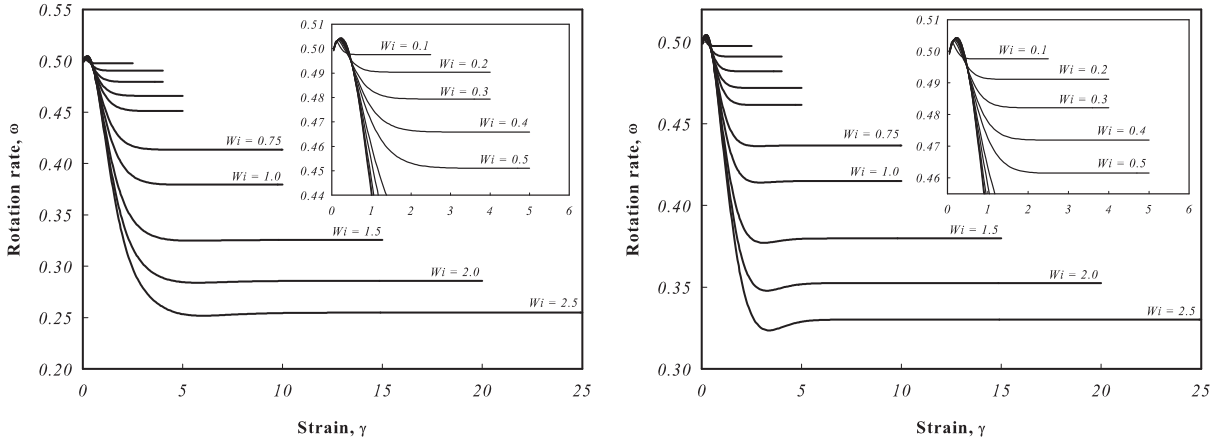

Figure 3.7: Transient rotation rate for Phan-Thien Tanner model for different Weissenberg numbers ($\epsilon = 0.1$ on the left and $\epsilon = 0.5$ on the right).

not show any slowing down of the sphere, which keeps rotating as in the Newtonian case also at high Wi.

Conversely, the Maxwell model (solid line in Figure 3.9) apparently shows a substantial increase of $\overline{T}$ (decrease of ω), i.e., a slowing down of the sphere angular velocity, with increasing Wi. The $\overline{T}$ vs Wi curve soon reaches an asymptotic slope of $\sim 4/5$. Thus, fluid elasticity rather than shear-thinning seems to be responsible for the slowing down of particle rotation at finite Wi. As it will be shown in the following, the Maxwell model, in fact, leads to the largest rotation period of the sphere, at least in the investigated Wi-range.

Finally, the rotation period of the sphere in a PTT fluid is also plotted in Figure 3.9.

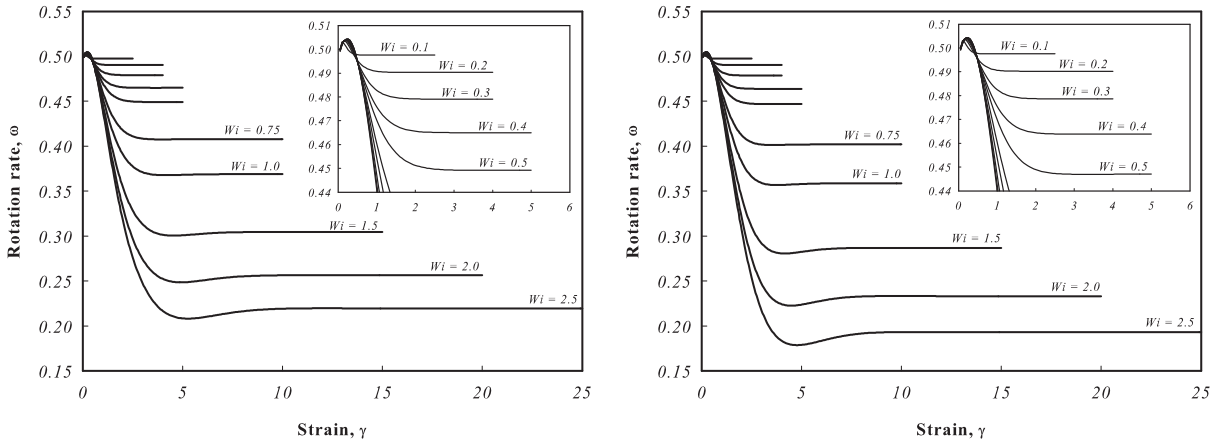

Figure 3.8: Transient rotation rate for Giesekus model for different Weissenberg numbers ($\alpha = 0.2$ on the left and $\alpha = 0.5$ on the right).

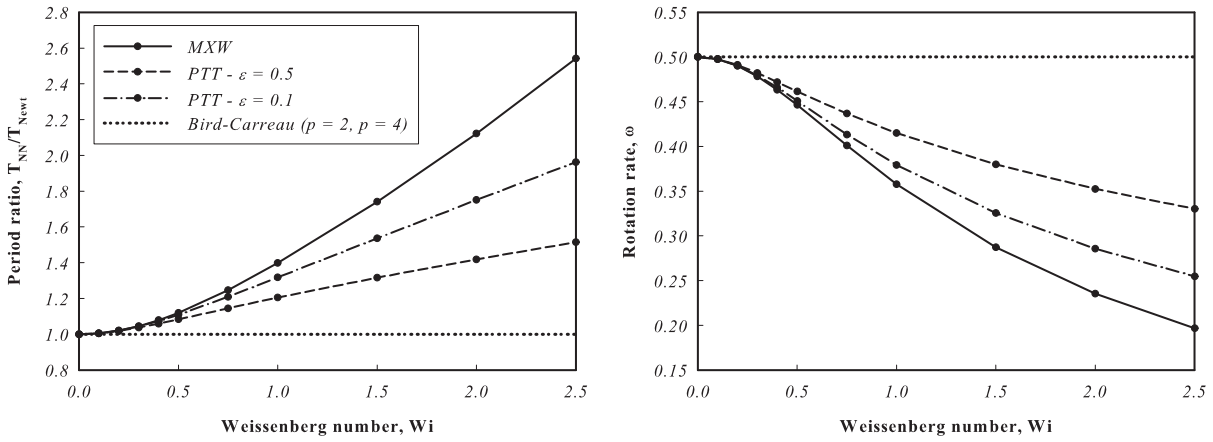

Figure 3.9: Steady state period ratio (left) and rotation rate (right) for Maxwell, Bird-Carreau and Phan-Thien Tanner models, as functions of Weissenberg number.

Two different values of the constitutive parameter are chosen: $\epsilon = 0.1$ (dot-dashed line), and $\epsilon = 0.5$ (dashed line). The rotation period (rotation rate) increases (decreases) by increasing Wi, and the constitutive parameter ϵ modulates the slope of the curves. Both curves lie in between the Maxwell and Bird-Carreau (= Newtonian) ones. In comparing PTT with Maxwell predictions, it so appears that the "weakening" of N_1 of the suspending fluid with increasing Wi (with respect to the Maxwell behavior $N_1 = 2Wi$) implies a smaller slowing down effect on the particle rotation.

Notice that, by increasing ϵ at fixed Wi, a smaller rotation period is predicted (i.e., a faster rotation). This is shown in Figure 3.10 where $\overline{T}$ and ω vs ϵ are plotted, for $Wi = 2.0$. The curves start from the Maxwell prediction ($\epsilon = 0$), and monotonic trend is observed.

The predictions with a Giesekus model are reported in Figure 3.11, where also the Maxwell and Bird-Carreau results are plotted for the sake of comparison. As for the Maxwell model, an increase (decrease) of the normalized period $\overline{T}$ (rotation rate ω) is observed with increasing Wi. As for the PTT model, such an increase is less steep than for the Maxwell fluid. However, notice that for the maximum exploited α parameter (= 0.5), the curve overlaps the Maxwell one.

Indeed, an interesting feature of the Giesekus fluid is the effect of the α parameter on the period ratio. At fixed Wi, a non-monotonic behavior of $\overline{T}$ with increasing α is found, as shown in Figure 3.12 (contrast with Figure 3.10 for the PTT model) for $Wi = 2.0$. A similar behavior is found at other Wi. The reason for such a non-monotonic behavior is unclear. It should perhaps be considered that the Giesekus fluid is the only fluid investigated here possessing a nonzero second normal stress difference. The presence of a minimum for $\overline{T}$ (maximum for ω) implies that for low values of α the rotation period departs from Maxwell prediction, to increase again for larger α (at a constant value of Wi).

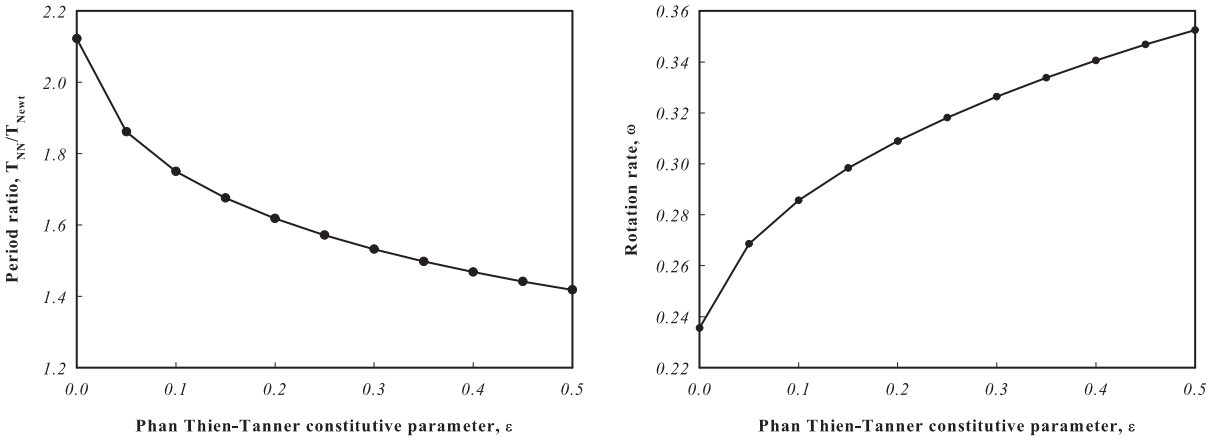

Figure 3.10: Steady state period ratio (left) and rotation rate (right) as functions of ϵ constitutive parameter for Phan-Thien Tanner model ($Wi = 2.0$).

3.4.2 Rheological properties

The rheology of a dilute suspension of rigid spheres in simple shear flow is now explored. Once the full problem is solved in the simulation cell, the local stress fields are obtained, and the bulk stress of a dilute suspension as a whole is recovered by using the Batchelor formula [9]:

$$\langle \boldsymbol{\tau} \rangle = \frac{1}{V} \int_{V - \frac{4\pi R^3}{3}} \boldsymbol{\tau}\, dV + \frac{3}{4\pi R^3} \phi \int_{4\pi R^2} \boldsymbol{\tau} \cdot \boldsymbol{nx}\, dA \tag{3.34}$$

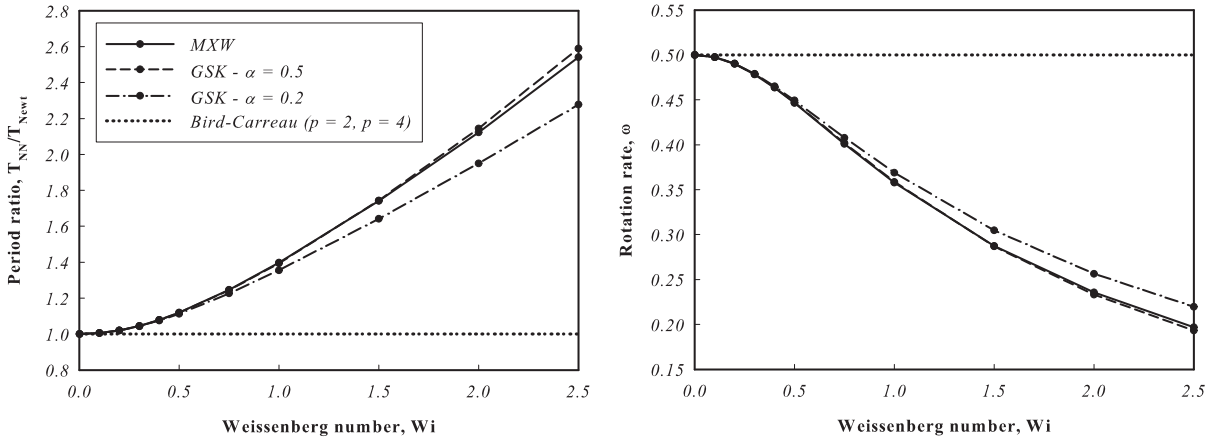

Figure 3.11: Steady state period ratio (left) and rotation rate (right) for Maxwell, Bird-Carreau and Giesekus models, as functions of Weissenberg number.

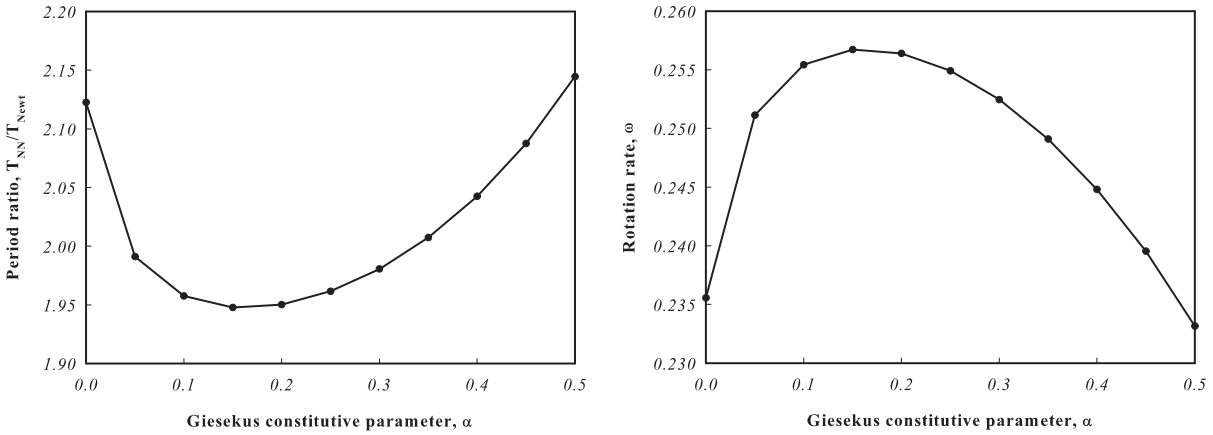

Figure 3.12: Steady state period ratio (left) and rotation rate (right) as functions of α constitutive parameter for Giesekus model ($Wi = 2.0$).

In Eq. (3.34), $\langle \boldsymbol{\tau} \rangle$ is the deviatoric bulk stress of the suspension, V and $4/3\pi R^3$ are the cell and sphere volume, respectively, ϕ is the (low) volume fraction of the suspension, $4\pi R^2$ is the sphere surface, $\boldsymbol{n}$ is the normal to the surface itself and $\boldsymbol{x}$ is the position of a point on the sphere surface. It is of course presumed in Eq. (3.34) that the cell is large enough to recover undisturbed fields at the cell boundaries.

In the case of shear flow, with x as the velocity direction and y as the gradient direction, the bulk viscosity is related to the xy component of the bulk stress tensor as follows:

$$\langle \eta \rangle = \frac{\langle \tau_{xy} \rangle}{\dot{\gamma}} \tag{3.35}$$

The bulk first and second normal stress differences are defined as:

$$\langle N_1 \rangle = \langle \tau_{xx} - \tau_{yy} \rangle \tag{3.36}$$

$$\langle N_2 \rangle = \langle \tau_{yy} - \tau_{zz} \rangle \tag{3.37}$$

In the following, predictions for the quantities $\langle \eta \rangle$, $\langle N_1 \rangle$ and $\langle N_2 \rangle$ will be given in nondimensional form, i.e., using λ as the characteristic time scale, and $eta_0\dot{\gamma}$ as the scale for the stress.

Analytical predictions for a dilute suspension of rigid spheres in SOF fluid under simple shear flow were given in Chapter II and in [14, 15, 16]. Here is reported the constitutive equation for a SOF fluid (in nondimensional form) (Eq. (2.8)):

$$\boldsymbol{\tau} = 2\boldsymbol{D} - Wi(\boldsymbol{A} + b\boldsymbol{D} \cdot \boldsymbol{D}) \tag{3.38}$$

where $\boldsymbol{A}$ is the second Rivlin-Ericksen tensor, and b is a constitutive parameter linked to normal stresses. For the viscoelastic fluids considered in this work, the SOF asymptote

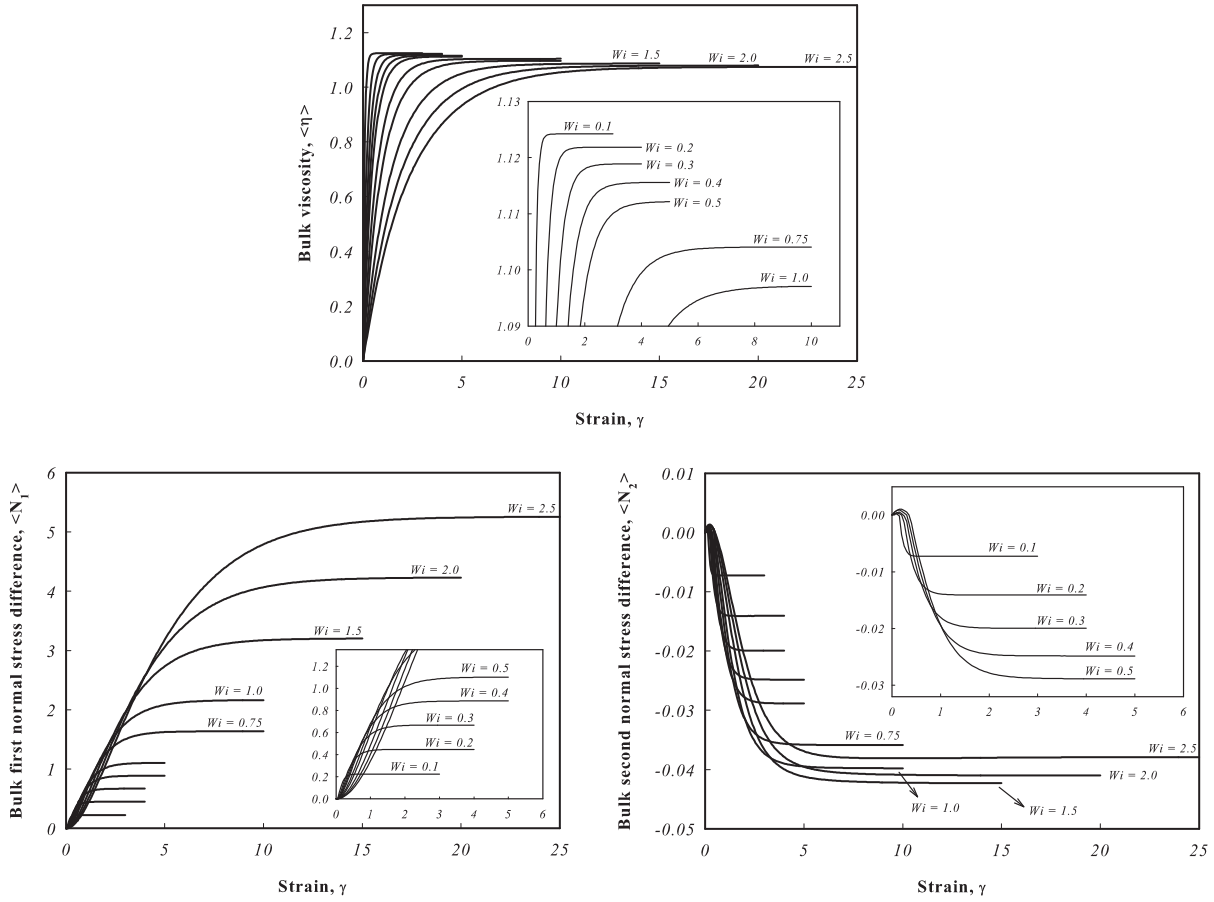

Figure 3.13: Transient bulk viscosity, first and second normal stress differences for Maxwell model and different Weissenberg numbers.

is recovered with $b = -8$ for the Maxwell and PTT models, whereas for the Giesekus fluid b depends on α. A quantitative agreement between our present simulations and SOF predictions for $Wi \to 0$ is then expected.

The results presented below refer to a volume fraction $\phi = 0.05$, which is chosen in such manner that the suspension can still be expected to be in the dilute limit, yet sufficiently high to give a significant suspension contribution to the overall stress. For all suspensions considered here, the suspension viscosity, the first and (in absolute value) the second normal stress differences are all found to increase with respect to the corresponding quantities for the pure suspending fluids, at any given Wi. In general, it is also found that with increasing Wi the differences between suspension and pure fluid rheological quantities progressively slightly decrease.

In Figure 3.13, $\langle\eta\rangle$, $\langle N_1\rangle$, and $\langle N_2\rangle$ are reported as a function of strain for a suspensions of spheres in a Maxwell fluid, for different Weissenberg numbers. All the curves start from 0 and a monotonic behavior can be noticed. In particular, the bulk viscosity and N_1

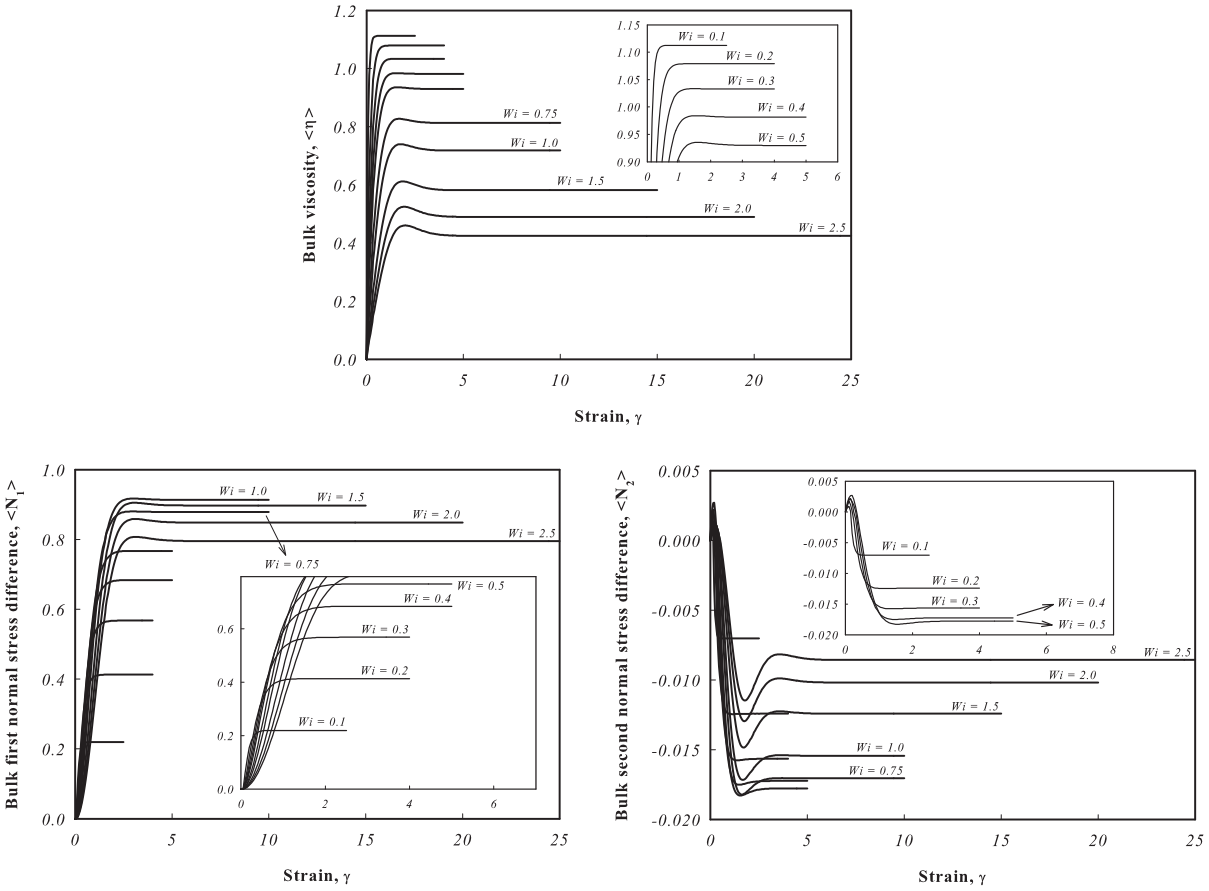

Figure 3.14: Transient bulk viscosity, first and second normal stress differences for Phan-Thien Tanner model ($\epsilon = 0.5$) and different Weissenberg numbers.

increases with strain whereas bulk N_2 decreases. However, no overshoot/undershoot is found. Finally, notice also that the steady state viscosity does not change too much if Wi is varied, even if, of course, the time to achieve the steady state is strongly dependent on it.

A different behavior is found for the PTT model ($\epsilon = 0.5$) as shown in Figure 3.14. In this case, the viscosity trend is strongly influenced by Wi. In addition, for high Wi an overshoot in $\langle\eta\rangle$ and $\langle N_1\rangle$ can be observed. As the transient rotation rate, the overshoot is more and more pronounced if ϵ increases. Regarding $\langle N_2\rangle$, starting from 0, a decreasing trend is initially observed, then a minimum is attained and, if Wi is sufficiently high, also a maximum is reached before achieving the steady state. It's important to point out that unfilled Maxwell as well as PTT fluids do not predict any second normal stress differences that then arise by adding particles into the fluid. This behavior was predicted by the SOF theory as well (see Eq. 2.40).

Finally, in Figure 3.15, rheological quantities for a suspension of spheres in a Giesekus

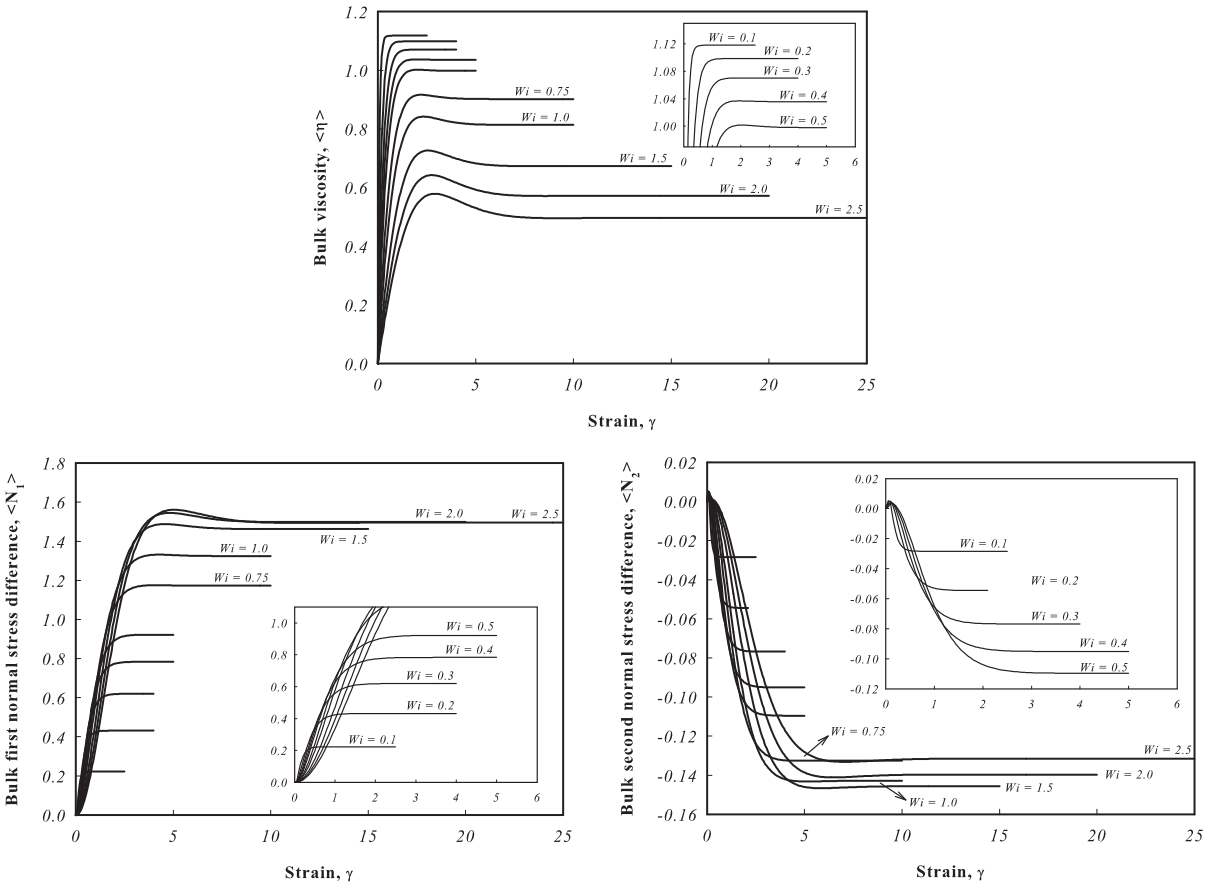

Figure 3.15: Transient bulk viscosity, first and second normal stress differences for Giesekus model ($\alpha = 0.2$) and different Weissenberg numbers.

fluid are depicted ($\alpha = 0.2$). A similar behavior of $\langle\eta\rangle$ and $\langle N_1\rangle$ with PTT suspension is found, but the second normal stress difference graph shows only an undershoot for high Wi. However the magnitude of bulk N_2 is one time greater than a Maxwell and PTT suspension, since a pure Giesekus fluid predicts non-zero second normal stress difference.

As did for the rotation rate, we can take the steady state values of the rheological quantities just shown in order to analyze the steady state behavior.

In Figure 3.16, the steady state bulk properties $\langle\overline{\eta}\rangle$, $\langle\overline{N}_1\rangle$, and $\langle\overline{N}_2\rangle$ (the over line means steady state) are reported as a function of Wi, for a suspension of spheres in a Maxwell fluid. The asymptotic SOF suspension results are plotted as dotted line and the grey line refers to the unfilled fluid.

Both viscosity of an unfilled SOF and a Maxwell fluid are equal to η_0 (=1) and they do not depend on Wi (not reported in figure). As just said, the SOF suspension viscosity (dotted line) is independent of Wi as well and coincides with the Newtonian one ($\langle\eta\rangle = 1.125$ for $\phi = 0.05$). A slight shear thinning of $\langle\overline{\eta}\rangle$ vs Wi is found for a filled Maxwell

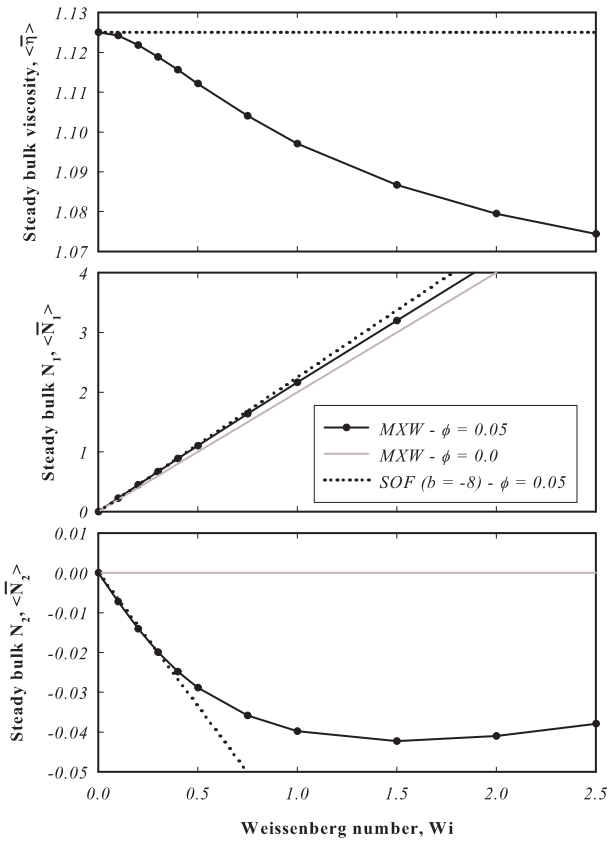

Figure 3.16: Steady state bulk viscosity, first and second normal stress differences for Maxwell fluid. The rheological properties for SOF fluid and unfilled Maxwell fluid are plotted as well.

fluid. This seems to imply that the slowing down of the rotational motion of the individual spheres corresponds to smaller dissipation.

The effect of solid particles on $\langle \overline{N}_1 \rangle$ in a Maxwell fluid can be observed on the second plot of Figure 3.16. At vanishing Wi the SOF asymptote is recovered. With increasing Wi, however, a slight thinning of the bulk first normal stress difference sets in, at variance with the behavior of a pure Maxwell fluid. Finally, a non-zero bulk second normal stress difference appears in the filled Maxwell fluid (as discussed above). The simulation results merge with the analytic SOF limit at low Wi, and for $b = -8$. It is worth noticing that the bulk second normal stress difference, which is only due to rigid inclusions in the Maxwell liquid, shows a clear non-monotonic behavior with Wi (with the adopted nondimensionalization).

Figure 3.17 shows the shear rheology for PTT suspending fluid. Two values of the PTT parameter ϵ are considered, namely, $\epsilon = 0.1$ and 0.5. The suspension viscosity starts from Newtonian or SOF prediction, and shear thins with increasing Wi. The suspension

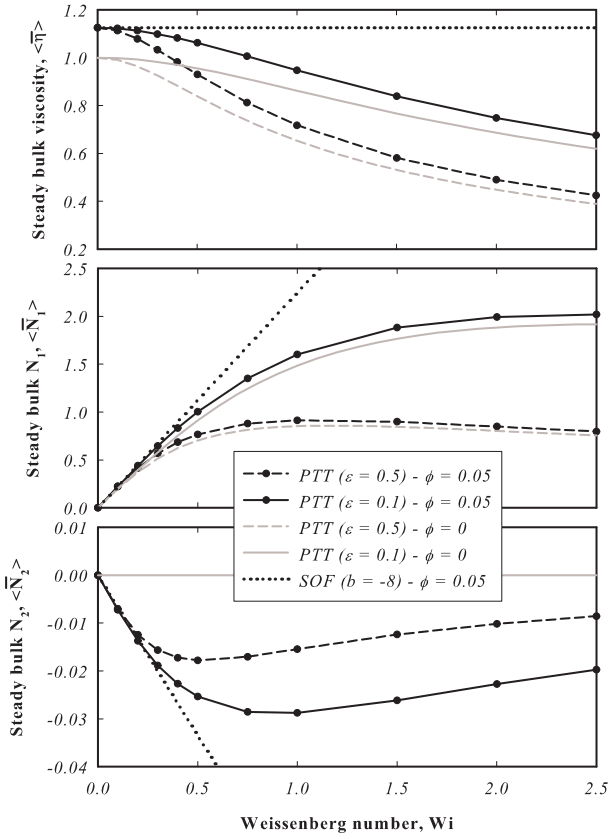

Figure 3.17: Steady state bulk viscosity, first and second normal stress differences for PTT fluid. The rheological properties for SOF fluid and unfilled PTT fluid are plotted as well.

first normal stress difference of course shows a thinning behavior much more evident than in the Maxwell suspension, as the suspending fluid is itself thinning. A slight maximum is observed around $Wi = 1$ for the $\epsilon = 0.5$ PTT suspension. Both viscosity and first normal stress difference are higher than the corresponding unfilled fluid quantity (grey lines). Finally, a non-zero second normal stress difference appears in the suspension, with clear minima at both ϵ values. Notice that, again, for $Wi \to 0$ all curves asymptotize to the corresponding SOF curves. Specifically, for the suspension second normal stress difference, note that the two PTT fluids investigated have a common SOF asymptote, as the b value (see Eq. (3.38)) of the SOF fluid corresponding to PTT (for $Wi \to 0$) does not depend on ϵ.

In Figure 3.4.2, the material functions for a suspension of spheres in a Giesekus fluid are illustrated. Two values of the constitutive parameter α are chosen, $\alpha = 0.2$ and 0.5. All the trends already observed for the PTT fluid are qualitatively confirmed.

Concerning the suspension second normal stress difference, it is worth noting that the $Wi \to 0$ asymptote now depends on the parameter α. The corresponding SOF asymptote

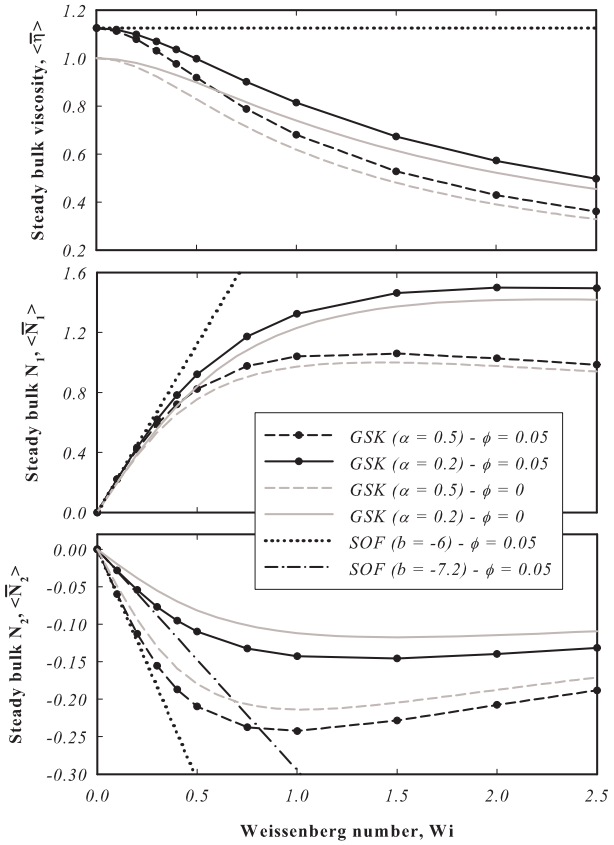

Figure 3.18: Steady state bulk viscosity, first and second normal stress differences for GSK fluid. The rheological properties for SOF fluid and unfilled GSK fluid are plotted as well.

for the Giesekus fluid is recovered with $b = 4(\alpha - 2)$. It is apparent from Fig. that the agreement between numerical and analytical predictions in the vanishing Wi limit is excellent.

Coming back to the differences between suspension bulk properties and suspending fluid properties, Figure 3.19 shows the ratio of the viscosity of the suspension (at $\phi = 0.05$) to that of the pure suspending liquid versus Wi, for the Maxwell, PTT ($\epsilon = 0.1$) and Giesekus ($\alpha = 0.2$) models. In all cases, as already mentioned in the beginning of this Section, the relative increase of the viscosity due to the rigid inclusions decreases with increasing Wi. Similar trends (not shoewn) are found for the ratios $\langle N_{1,\phi=0.05}\rangle/\langle N_{1,\text{pure}}\rangle$ and $\langle N_{2,\phi=0.05}\rangle/\langle N_{2,\text{pure}}\rangle$. Thus, in the dilute regime at least, the influence of the filler slightly weakens with increasing Wi, as already mentioned in the beginning of this Section.

An alternative way to show the steady state behavior of rheological properties is suggested in [62, 63, 17], where the bulk normal stress differences are plotted as a function of bulk shear stress, $\langle \boldsymbol{\sigma}_{xy} \rangle$. The (dimensional) stress differences are scaled by $G = \eta_0/\lambda$. Our simulation results are reported in Figure 3.20, for Maxwell (a), Giesekus (b) and Phan-

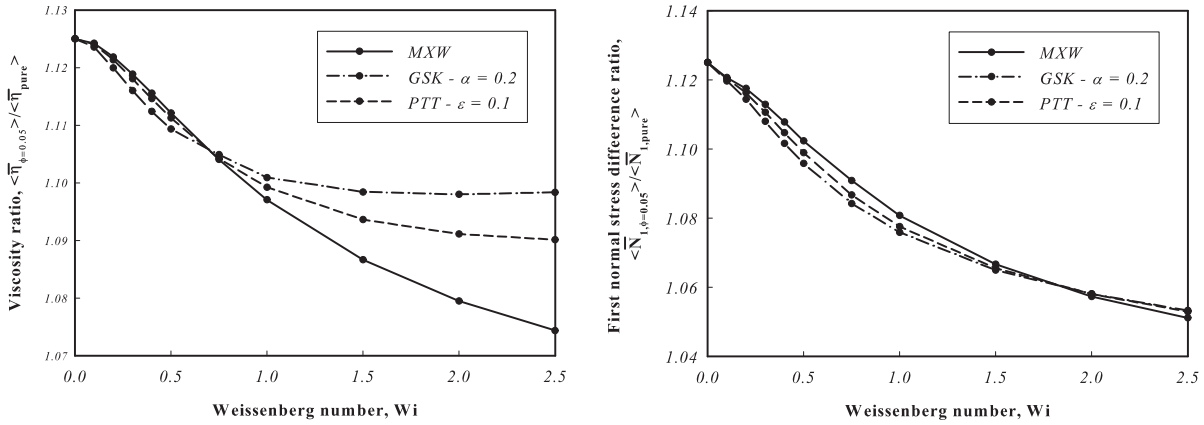

Figure 3.19: Viscosity and first normal stress difference ratio for Maxwell, PTT ($\epsilon = 0.1$) and Giesekus ($\alpha = 0.2$) fluids.

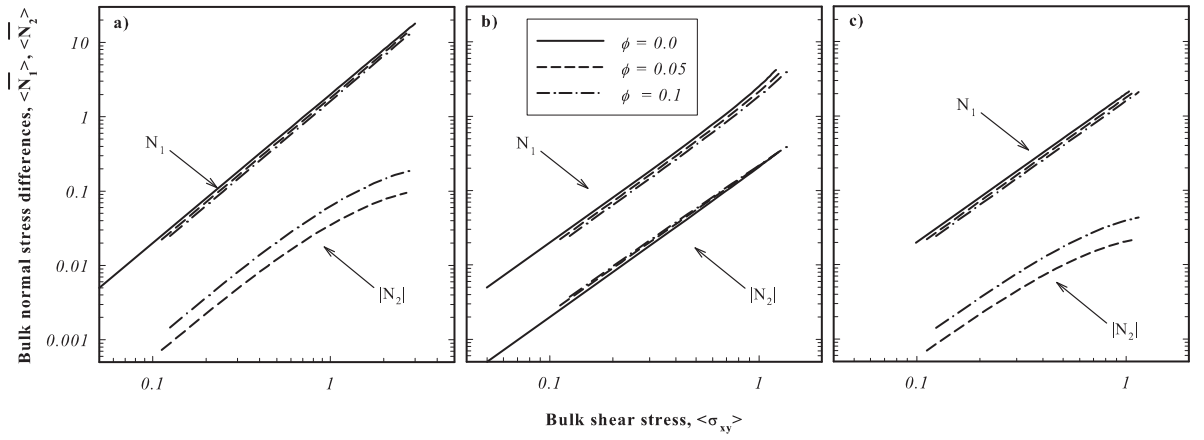

Figure 3.20: Bulk first and second normal stress differences (normalized by $G = \eta_0/\lambda$) as a function of bulk shear stress for Maxwell (a), Giesekus (b) and Phan-Thien Tanner (c) models.

Thien Tanner (c) models. Solid lines (if any) refer to the pure suspending liquid, and the effect of increasing ϕ is shown in the figure. With this representation, the first and second normal stress differences decrease and increase, respectively, with increasing volume fraction. (As already showed above, N_2 for Maxwell and PTT model only exists for the filled systems.) These trends are in good qualitative agreement with the experimental results by Mall-Gleissle et al. [17]. Quantitative agreement between predictions and data can not be assessed, however. Indeed, the experimental data are taken at volume fractions not actually in the dilute regime. Moreover, our simulations are made in a limited Wi-range (up to 2.5), whereas experimental data were taken at larger Wi-values.

3.5 Conclusions

In this Chapter we abandoned the low Weissenberg number hypothesis (Chapter II) and we analyzed the fluid dynamic and the rheology of a dilute suspension of spheres at high Wi in simple shear flow. The analysis is carried out through numerical simulations by solving the governing equations of the system coupled with a viscoelastic constitutive equation for the suspending fluid. Viscoelastic models with different behaviors are taken into account in order to relate the phenomena observed to a particular non linear effect.

A cubic frame with a sphere at the center is considered, so that the sphere can only rotate. Shear flows boundary conditions are imposed on the cubic faces and the size of the cube is chosen sufficiently larger than the particle radius to recover unperturbed conditions on the cube boundaries. Since the sphere does not translate, it is represented by a fixed spherical surface. The rigid-body motion (i.e. rotation) is imposed by means of constraints on the surface (Lagrange multipliers). In this way, the torque-free condition is automatically satisfied and the angular velocity is added as unknown and is recovered by solving the full system of equations.

In order to improve the convergence at high Weissenberg number, we discretized the momentum equation with the DEVSS-G [42, 55] formulation combined with the SUPG method [56] for constitutive equations. In addition, the log-conformation representation is used [57, 58] in order to improve the numerical stability and an implicit time-stepping procedure is implemented.

Preliminary convergence tests are carried out in order to test the code and set proper mesh parameters (resolution and domain size) as well as the time step.

First of all, results about the rotation rate of the sphere are discussed by focusing the attention on the impact of the viscoelasticity and the viscoelastic model. Our simulations showed the purely viscous Bird-Carreau model is not able to capture the experimentally observed slowing down of the sphere. On the contrary, if first normal stress differences are taken into account, the slowing down effect can be predicted and it is more and more pronounced if the Weissenberg number increases (in qualitative agreement with experiments [20]). In particular, the Maxwell model predicts the slowest rotation whereas the Giesekus and Phan-Thien Tanner curves lie in between the Maxwell and Newtonian ones. However, the additional constitutive parameter of Giesekus and PTT models strongly affect the slope of these curves. In this regard, for PTT model, a monotonic trend of the rotation rate as a function the constitutive parameter is found whereas a maximum is attained for a Giesekus fluid. The transient analysis has shown different behaviors as well. Starting form the Newtonian rotation rate, we found a decreasing trend of the rotation rate in time for every model investigated. However, Maxwell model always predicts a monotonic behavior whereas for Giesekus and PTT models an undershoot is observed if Wi is sufficiently high.

The bulk rheology of such a suspension is then investigated. The bulk properties are recovered by using a standard averaging procedure [9] where the bulk stress is given by a contribution of the fluid as well of the solid. If a Maxwell model is considered, starting from the Newtonian prediction, we found a slight shear thinning steady state bulk viscosity even if the unfilled fluid predicts a constant viscosity. Furthermore, the presence of the particles

increase bulk N_1 with respect to the pure fluid and, surprisingly, leads to non zero bulk second normal stress differences. The transient analysis shows again a monotonic trend.

The steady state bulk viscosity and N_1 for PTT and Giesekus shows a similar behavior and both are higher then the corresponding unfilled fluid quantity. Again, a non zero second normal stress difference is found for PTT if particles are added into the fluid. Contrarily to Maxwell predictions, overshoots and undershoots are observed in the transient trends of these rheological properties.

In addition, for vanishing Wi, our simulation results are in excellent agreement with the analytical predictions for a SOF suspension carried out in the previous Chapter.

Finally, the influence of the particle concentration is also investigated. Our simulations predict a decreasing bulk N_1 and a increasing bulk N_2 (in absolute value) if the volume fraction is increased. These results are in qualitatively agreement with experimental data from literature [17].

Chapter 4

Concentrated suspensions in planar elongational flow - Newtonian case

4.1 Introduction

The analysis carried out in the previous Chapters is based on the diluteness assumption. Typically, in many systems of practical interest, the concentration of particles is high so they are non-dilute or concentrated. In other words, a many-particle system should be considered and the hydrodynamic interactions play a crucial role by affecting the local flow fields, bulk properties and the final behavior of the material. It is quite obvious that, in this case, not only an analytical theory cannot be assessed but the computational scheme is not straightforward anymore. Indeed, in order to take into account hydrodynamic effects, particle interactions need to be considered, leading to the development of solid structure. The particles, in fact, are not isolated anymore but move because of the fluid and the particles themselves. Therefore a proper numerical scheme needs to be developed.

In the last decades, Direct Numerical Simulations (DNS) techniques have been developed in order to predict and understand the complex flow of particle-filled fluids. The motion of the fluid is governed by the (Navier-)Stokes equations and the motion of the particles by the linear and angular momentum equations of rigid-body dynamics. The coupling of the fluid and the particles is achieved through the no-slip condition on the particle boundaries and the hydrodynamic forces and torques on the particles. The hydrodynamic forces and torques are, of course, those arising from the computed motion of the fluid, and therefore are not known in advance. These interactions are then computed and no theoretical approximation is required.

In order to manage the problem computationally, we need to develop a suited simulation scheme using the smallest domain that still has the same average properties as the whole suspension. Hence, by solving the flow problem in this domain, we should be able to predict the average micro-structure and the bulk properties of the suspensions, with reduced CPU time and memory.

This idea has been used by Hwang et al. [28, 27] where the authors combine Lees-

Edwards boundary conditions, i.e. a sliding bi-periodic domain, with a standard velocity-pressure finite element formulation for a Newtonian suspension as well as a DEVSS/DG (Discrete Elastic Viscous Split Stress/Discontinuous Galerkin) scheme for viscoelastic suspensions in simple shear flow. According to this scheme, each frame slides relatively to one another by an amount determined by a given shear rate. So, a frame can be considered a sample of the whole suspension and transforms the many-particle suspension into a single unit cell. The results reported by the authors (for both Newtonian and viscoelastic case) are very promising. The implemented scheme allows to consider in an efficient way concentrated solid suspensions subjected to shear flow.

Recently, the bi-periodic frame concept has been extended to planar extensional flow as well [29]. However, in order to deal with such a flow, a deformation in time of the bi-periodic frame is proposed. As a consequence, after a certain time, the frames cannot be deformed anymore since the smallest characteristic length of the frame is comparable with the characteristic dimension of the particles. Hence, it is difficult to achieve a steady state for this imposed flow field. This is especially true for a viscoelastic fluid at high Weissenberg number, where large strains are needed before a steady state is obtained. Finally, in the scheme described in [29] remeshing of the domain is also done in order to keep the aspect ratio of the elements close to one.

In this Chapter, we propose a new simulation scheme that circumvents these problems. The main concept is to relocate a particle on the inflow boundary of the domain when it crosses the outflow sections. So, no periodic boundary condition is imposed. In particular, the computational domain is divided into three concentric square regions: in the internal one the particles move, the micro-structural and bulk properties are evaluated in this region. So, this region can be considered as a sample of the whole suspension. In the intermediate region the particles can move as well and, when they cross the outflow boundaries of that region, they are relocated randomly on one of the two inflow sections of the same region. Finally, the outer region only contains fluid since particles cannot enter. The elongational flow boundary conditions are imposed on the external boundaries of the outer region: so the particles feel the presence of the elongational flow boundary conditions only as an imposed "far field".

According to this scheme, no deformation of the domain occurs and a time-independent fixed grid can be used (and no need remeshing of the domain is needed). Furthermore, an average steady state can be achieved: we do not need to stop the simulation since the domain dimensions do not change. Finally, this scheme is suited for the simulation of viscoelastic suspensions. Indeed, after the relocation of the particles in the intermediate region, the stress has time to develop before particles enter the internal region where the properties are calculated.

Therefore, we consider a concentrated suspension of rigid, non-Brownian disks in a planar elongational flow, where the particle and fluid inertia can be neglected.

In this Chapter the analysis is carried out for a Newtonian medium, whereas in Chapter IV the viscoelasticity of the suspending fluid is considered. The particle-fluid interactions are taken into account by implementing a Lagrange Multiplier/Fictitious Domain Method (LM/FDM) [30, 64]. The force-free, torque-free rigid body motion of the particles is de-

scribed by a rigid-ring problem [28, 27]. So, a fixed mesh is used for the computation and the particles are described by their boundaries only, through collocation points. This description is possible because inertia is neglected. Finally, the rigid-body motion constraints are imposed through Lagrange multipliers, that can be identified as traction forces on the particle surfaces (with a correction due to the fluid stress inside the object).

Another difference with the works of Hwang et al. [28, 27, 29] is that with our scheme a particle is not splitted into parts since it never crosses the boundary of the whole domain. However, since a particle can cross the sample internal region, a slight modification of the bulk stress formula is required. Finally, our method is easy to implement and it can be easily extended to 3D problems, even if, in the latter case, iterative solvers and parallel calculations are needed.

Numerical simulations are performed and the local flow fields are presented for a many-particle problem. The bulk stress is recovered by using a standard averaging procedure [9]. Finally the bulk rheological properties are discussed and a comparison with the results of Hwang and Hulsen [29] is carried out. Our results on the bulk viscosity of the suspension are in very good agreement. Moreover, an anisotropic structure is also found even if no transient behavior as in [29] is observed.

The Chapter is organized as follows: in Section 4.2, the problem definition is presented. The governing equations for fluid, particles and hydrodynamic interactions are given as well. In Section 4.3, the weak form for the whole domain is derived. Moreover, the spatial implementation and time integration algorithms are discussed. In Section 4.4, the bulk stress formula is given. In Section 4.5, the method is validated. A comparison between the Lagrange multipliers/fictitious domain method and a boundary fitted method is carried out. A simple test problem is chosen. In particular, local flow fields and bulk stress are exploited. The influence of the number of collocation points on the accuracy of the solution is also analyzed. Moreover, the relationship between Lagrange multipliers and traction forces on the particles is discussed. In Section 4.6, the simulation procedure is introduced. The computational scheme is presented and particle area fraction and bulk stress formulas are given. In Section 4.7, the results for planar extensional flow are presented. A many-particle problem (150 and 225 particles) is simulated. Local velocity, pressure, stress fields are analyzed and discussed, by means of snapshots of the simulations. Finally, bulk properties (stress tensor and viscosity) are evaluated.

4.2 Modeling

Suspensions consisting of a large number of rigid non-Brownian circular disk particles (2D problem) in planar elongational flow are considered. A schematic representation of the problem is shown in Figure 4.1: many particles (circles) move in a Newtonian fluid medium. Particles are denoted by $P_i(t)$, $i = 1 \dots N$, where N is the total number of particles in the domain.

A square domain, denoted by Ω, is considered. On the fluid boundaries, denoted by Γ_i, $i = 1 \dots 4$, planar elongational flow boundary conditions are imposed. The Cartesian

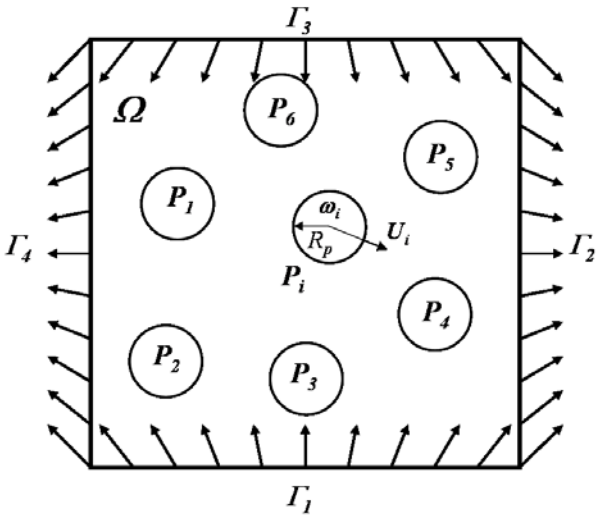

Figure 4.1: Schematic representation of the problem: a square fluid domain (Ω) filled with many particles ($P_i(t)$) is considered. Elongational flow conditions on the fluid boundaries (Γ_i) are imposed.

x and y coordinates are selected such that the origin is at the center of the domain. The particles move according to the imposed flow and hydrodynamic interactions: their rigid-body motion is completely defined by the translational velocity, $\boldsymbol{U}_i = (U_i, V_i)$, and angular velocity, $\boldsymbol{\omega}_i = \omega_i \boldsymbol{k}$, where $\boldsymbol{k}$ is the unit vector in the direction normal to the $x-y$ plane. Moreover, for a particle P_i, $\boldsymbol{X}_i = (X_i, Y_i)$, $\boldsymbol{\Theta}_i = \Theta_i \boldsymbol{k}$ are used for the coordinates of the particle center and the angular rotation, respectively. Here, the governing equations for a Newtonian suspension are presented, for the fluid domain as well as for the particles.

4.2.1 Fluid domain

For a Newtonian and inertialess fluid, the momentum balance, the continuity and the constitutive relation are:

$$\nabla \cdot \boldsymbol{\sigma} = \boldsymbol{0} \quad \text{in } \Omega \backslash P(t) \tag{4.1}$$

$$\nabla \cdot \boldsymbol{u} = 0 \quad \text{in } \Omega \backslash P(t) \tag{4.2}$$

$$\boldsymbol{\sigma} = -p\boldsymbol{I} + 2\eta \boldsymbol{D} \quad \text{in } \Omega \backslash P(t) \tag{4.3}$$

where $\boldsymbol{u}$, $\boldsymbol{\sigma}$, p, $\boldsymbol{I}$, $\boldsymbol{D}$ and η are the velocity, the stress, the pressure, the 2x2 unity tensor, the rate-of-deformation tensor and the viscosity, respectively and $P = \bigcup P_i$.

The fluid boundary conditions are given by:

$$\boldsymbol{u} = \boldsymbol{U}_i + \boldsymbol{\omega}_i \times (\boldsymbol{x} - \boldsymbol{X}_i) \quad \text{on } \partial P_i(t) \quad (i = 1 \ldots N) \tag{4.4}$$

$$u = \dot{\epsilon} x, \quad v = -\dot{\epsilon} y \quad \text{on } \Gamma_i \quad (i = 1 \ldots 4) \tag{4.5}$$

assuming that all particles are fully immersed in the fluid. Equation (4.4) is the rigid-body condition and $\boldsymbol{x}$ are the coordinates of the points on the particle surface. Equation (4.5) gives the planar elongational flow boundary conditions where $\dot{\epsilon}$ is the elongational rate. In the absence of inertia, no initial conditions are needed for the velocity field of the fluid as well as for the particles. Finally, it is sufficient to set the pressure level in one point of the domain.

4.2.2 Particle domain

Following [28, 27], in this work a rigid-ring description for the particle domain is used. In this way, a particle is considered as a rigid ring which is filled with the same fluid as in the fluid domain. This description can be used if the inertia is neglected. So, it is necessary to discretize only the particle boundary, which leads to reduction in memory requirements and simplifies the implementation. Moreover, as shown later, the traction force on the particle boundaries can be obtained as a part of the solution, when the rigid-body constraints are implemented through Lagrange multipliers.

With the rigid-ring description, the equations for a particle P_i can be written as:

$$\nabla \cdot \hat{\boldsymbol{\sigma}} = \mathbf{0} \quad \text{in } P_i(t) \tag{4.6}$$

$$\nabla \cdot \boldsymbol{u} = 0 \quad \text{in } P_i(t) \tag{4.7}$$

$$\hat{\boldsymbol{\sigma}} = -p\boldsymbol{I} + 2\eta\boldsymbol{D} \quad \text{in } P_i(t) \tag{4.8}$$

$$\boldsymbol{u} = \boldsymbol{U}_i + \boldsymbol{\omega}_i \times (\boldsymbol{x} - \boldsymbol{X}_i) \quad \text{on } \partial P_i(t) \tag{4.9}$$

Again, Eqs. (4.6)-(4.9) are equations for the momentum balance, the continuity, the constitutive relation and the boundary condition respectively, which are the same for the fluid domain. Note, that we have denoted the fluid stress tensor inside the particle ($\hat{\boldsymbol{\sigma}}$) different from the stress tensor in the fluid between particles in order to make a distinction between the stress tensor inside the 'real' rigid particle ($\boldsymbol{\sigma}$) and the fictitious fluid stress. The solution of the problem inside a particle is the rigid-body motion itself as applied on the particle boundary [28, 27]:

$$\boldsymbol{u} = \boldsymbol{U}_i + \boldsymbol{\omega}_i \times (\boldsymbol{x} - \boldsymbol{X}_i) \quad \text{in } P_i(t) \tag{4.10}$$

With this description, the pressure level inside a particle is undetermined/not unique, in theory. However it turns out that, in the numerical implementation with the fictitious domain method, it is not necessary to specify the pressure level inside the particle directly. Finally, the movement of particles is given by the following kinematic equations:

$$\frac{d\boldsymbol{X}_i}{dt} = \boldsymbol{U}_i, \quad \boldsymbol{X}_i|_{t=0} = \boldsymbol{X}_{i,0} \tag{4.11}$$

$$\frac{d\boldsymbol{\Theta}_i}{dt} = \boldsymbol{\omega}_i, \quad \boldsymbol{\Theta}_i|_{t=0} = \boldsymbol{\Theta}_{i,0} \tag{4.12}$$

Equation (4.12) is completely decoupled from the other equations for circular particles.

4.2.3 Hydrodynamic interactions

Equation (4.4) (and (4.9) as well) adds (for the 2D case) three additional unknowns for each particle, namely the translational and angular velocities of the particle. So, it is necessary to consider the balance equations for drag forces and torques, acting on the particle boundaries. Under the assumptions of absence of inertia and external forces and torques, the particles are force-free and torque-free, so the balance equations are given by:

$$\boldsymbol{F}_i = \int_{\partial P_i(t)} \boldsymbol{\sigma} \cdot \boldsymbol{n} ds = \boldsymbol{0} \tag{4.13}$$

$$\boldsymbol{T}_i = \int_{\partial P_i(t)} (\boldsymbol{x} - \boldsymbol{X}_i) \times (\boldsymbol{\sigma} \cdot \boldsymbol{n}) ds = \boldsymbol{0} \tag{4.14}$$

In these equations, $\boldsymbol{F}_i = (F_{i,x}, F_{i,y})$ and $\boldsymbol{T}_i = T_i \boldsymbol{k}$ are the total force and torque on the particle boundaries, $\boldsymbol{n}$ is the outwardly directed unit normal vector on ∂P_i. As we can see, for the 2D case, (4.13) and (4.14) add three equations to the system.

The equations (4.1)-(4.3) for the fluid domain with boundary conditions (4.4)-(4.5), the corresponding equations for the particle domain (4.6)-(4.8) with boundary condition (4.9) and the hydrodynamic equations (4.13)-(4.14) form a system in the unknowns: p, $\boldsymbol{u}$, $\boldsymbol{\sigma}$, $\boldsymbol{U}_i$, $\boldsymbol{\omega}_i$. The kinematic equations (4.11)-(4.12) are integrated to update the particle positions and rotations. So, every time-step the problem is solved and the flow fields, rigid-body unknowns and stresses are evaluated. Next, we need to find an expression for the evaluation of bulk rheological properties (bulk stress, bulk viscosity, etc.). This will be presented in Section 4.4.

4.3 Weak form and implementation

4.3.1 Weak form

In this Section the derivation of the weak form is presented. In deriving the weak form of the governing equations, the hydrodynamic forces and torques on the particles can be completely eliminated by combining the fluid and particle equations of motion into a single weak equation of motion for the combined fluid and particle system. This equation is called the combined equation of motion and can be obtained by choosing a suitable variational space for the velocity which incorporates the rigid-body motion constraint (see [30, 65] for details). This formulation has two important advantages: the first is that the hydrodynamic forces and torques do not have to be computed or modeled anymore since they cancel in the weak form. The second advantage is that these schemes are not subject to numerical instabilities as shown in [65].

Extending the combined equation of motion to cover the particle domain, removing the rigid-ring constraint from the variational spaces and enforce it as a constraint using the Lagrange multipliers, the weak form for the whole domain can be obtained:

Find $\boldsymbol{u} \in H^1(\Omega)^2, \boldsymbol{U}_i \in \Re^2, \boldsymbol{\omega}_i \in \Re, \boldsymbol{\lambda}_i \in L^2(\partial P_i(t)), p \in L^2(\Omega) \;\; (i = 1 \dots N)$ such that:

$$-\int_\Omega \nabla\cdot\boldsymbol{v}\, p\, dA + \int_\Omega 2\eta \boldsymbol{D}(\boldsymbol{v}) : \boldsymbol{D}(\boldsymbol{u})\, dA + \sum_{i=1}^{N} \langle \boldsymbol{v} - (\boldsymbol{V}_i + \boldsymbol{\chi}_i \times (\boldsymbol{x} - \boldsymbol{X}_i)), \boldsymbol{\lambda}_i \rangle_{\partial P_i} = \boldsymbol{0} \quad (4.15)$$

$$\int_\Omega q \nabla\cdot\boldsymbol{u}\, dA = 0 \quad (4.16)$$

$$\langle \boldsymbol{\mu}_i, \boldsymbol{u} - (\boldsymbol{U}_i + \boldsymbol{\omega}_i \times (\boldsymbol{x} - \boldsymbol{X}_i)) \rangle_{\partial P_i} = \boldsymbol{0} \quad (4.17)$$

for all $\boldsymbol{v} \in H^1(\Omega)^2, \boldsymbol{V}_i \in \Re^2, \boldsymbol{\chi}_i \in \Re, \boldsymbol{\mu}_i \in L^2(\partial P_i(t)), q \in L^2(\Omega) \;\; (i = 1 \dots N)$.

This weak form is at the basis of the fictitious domain method since it includes both the fluid and particle domain. The rigid-body condition is included in the momentum balance and the constraints are implemented through Lagrange multipliers, only on the particle boundaries. As a consequence, a fixed, time-independent, very simple mesh can be used, circumventing the necessity of remeshing and projection, as needed in the ALE method [66, 67, 68].

The solution of equations (4.15)-(4.17) gives ($\boldsymbol{u}$, p, $\boldsymbol{U}_i$, $\boldsymbol{\omega}_i$) as well as all the Lagrangian multipliers. Then, the particle positions and rotations can be updated by integrating the kinematic equations (Eqs. (4.11) and (4.12)) and the problem is solved at the next time step. As previously discussed, it is not necessary to specify initial conditions for $\boldsymbol{u}$, $\boldsymbol{U}_i$ and $\boldsymbol{\omega}_i$ since both fluid and particles are inertialess. Instead, it is mandatory to set the pressure level, for example by specifying the pressure in a point of the domain. The resulting system is linear in the state variables and symmetric. It is solved by a direct method based on a sparse multi-frontal variant of Gaussian elimination (HSL/MA57) [69]. However, a direct method can be used only for 2D simulations since a huge matrix needs to be solved when dealing with 3D problems. In this case, in order to manage the memory requirements, iterative solvers should be used.

4.3.2 Spatial discretization

The fictitious domain allows to use a very simple, time-independent mesh for the discretization of the whole domain. In this work, a rectangular regular mesh with bi-quadratic interpolation for the velocity and bi-linear continuous interpolation for the pressure is used ($Q_2 - Q_1$ elements). It is well known that this kind of element satisfies the LBB condition. Due to the discontinuity of the pressure field between the fluid and particle domain a discontinuous interpolation for the pressure should preferably be used [28, 27, 70]. However, as we will discuss later, even if we use a discontinuous pressure interpolation ($Q_2 - P_1^d$ element), the pressure value on the particle surface cannot be recovered accurately.

From the rigid-ring description, the particles are discretized by their boundaries. The weak form of the rigid-ring description (Eq. (4.17)) has been approximated by point collocation:

$$\langle \boldsymbol{\mu}_i, \boldsymbol{u} - (\boldsymbol{U}_i + \boldsymbol{\omega}_i \times (\boldsymbol{x} - \boldsymbol{X}_i)) \rangle_{\partial P_i} \approx \sum_{k=1}^{N_c} \boldsymbol{\mu}_{i,k} \cdot \{\boldsymbol{u}(\boldsymbol{x}_k) - (\boldsymbol{U}_i + \boldsymbol{\omega}_i \times (\boldsymbol{x}_k - \boldsymbol{X}_i)) \quad (4.18)$$

where N_c is the number of collocation points on the particle surface, $\boldsymbol{x}_k$ are the coordinates of the k^{th} collocation point and $\boldsymbol{\mu}_{i,k}$ the corresponding Lagrange multiplier. This boundary discretization is very simple to implement and, as shown in Section 4.5, stresslets on the particles can be recovered by Lagrange multipliers values. It is important to point out that the number of collocation points is a crucial choice for the accuracy of the bulk stress: too few points cannot represent adequately the rigid-body motion while too many collocation points lead to an overestimation of the surface stress integrals. A detailed analysis about the choice of N_c will be carried out in Section 4.5.

In Figure 4.2 a comparison between a typical unstructured mesh for a boundary fitted method (on the left), and the fictitious domain mesh for the same particle configuration (on the right) is shown. In the first case only the fluid domain is discretized: no solution is obtained inside the particles. In the fictitious domain, however, we can observe a mesh inside the objects as well. As a consequence, after solving the equations, pressure and velocity (and stress) are also evaluated in the nodes inside the particles. Although it is not possible to accurately recover the pressure (and stresses) on the particle surface (see Section 4.5), a simple regular mesh can be used, giving the opportunity to solve very complex interaction problems in a simple way. Also, the discretization of the particle boundaries through collocation points is shown in Figure 4.2. Finally, in the same figure, a typical $Q_2 - Q_1$ element is shown.

4.3.3 Time integration

For a given initial particle configuration, the equations (4.15)-(4.17) can be solved and then it is possible to update the particle positions and rotations. To do this, it is necessary to integrate the kinematic equations (4.11)-(4.12). An explicit time integration scheme has

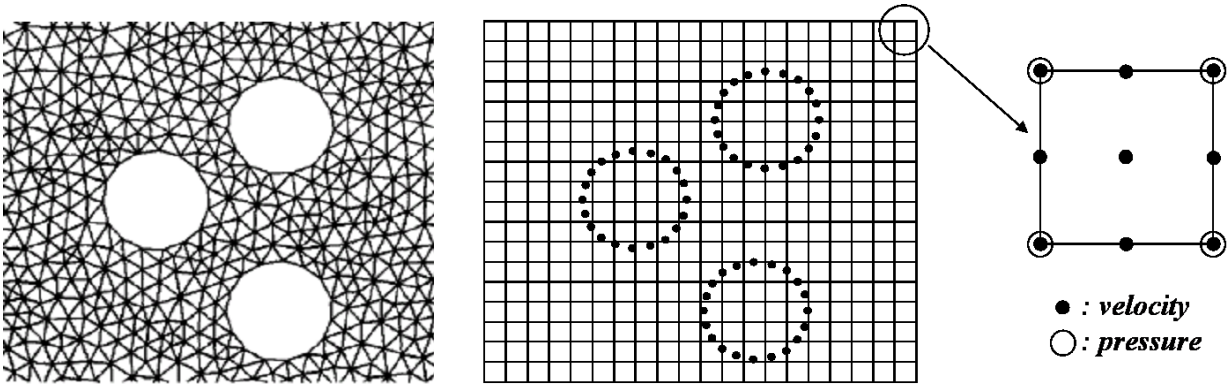

Figure 4.2: Comparison between an unstructured mesh (left) and a fictitious domain (right). In the fictitious domain method the particles are described by their boundaries through collocation points (rigid-ring description). A typical $Q_2 - Q_1$ element is shown as well.

been implemented: the Euler method at the first time step:

$$\boldsymbol{X}_i^{n+1} = \boldsymbol{X}_i^n + \triangle t \boldsymbol{U}_i^n \tag{4.19}$$

and the Adams-Bashforth method for the next time steps:

$$\boldsymbol{X}_i^{n+1} = \boldsymbol{X}_i^n + \triangle t \left(\frac{3}{2}\boldsymbol{U}_i^n - \frac{1}{2}\boldsymbol{U}_i^{n-1} \right) \tag{4.20}$$

4.4 Bulk stress

As previously discussed, we are interested in the rheological properties of concentrated suspensions in planar elongational flow, such as the stress tensor, viscosity, etc. The flow and stress fields obtained from the equations just presented are local. Local values of pressure and velocity give information about the stress distribution around the particles and thus also about the hydrodynamic interaction between particles. However, it is also important to evaluate global properties (bulk properties) in order to make predictions about global behavior of such materials. To do this, we have to consider a bulk stress expression related to local quantities. We will consider the Batchelor formula [9]. The bulk stress tensor can be calculated as the sum of the fluid contribution and the particle contribution, as follows (for the 2D case):

$$\langle \boldsymbol{\sigma} \rangle = \frac{1}{A} \int_A \boldsymbol{\sigma} \, dA = \frac{1}{A} \int_{A_f} \boldsymbol{\sigma} \, dA + \frac{1}{A} \int_{\partial A_p} \boldsymbol{\sigma} \cdot \boldsymbol{n}\boldsymbol{x} \, ds \tag{4.21}$$

where $\langle \cdot \rangle$ is an area average quantity in an area A, A_f is the area occupied by the fluid and ∂A_p is the total particle surface. For the Newtonian constitutive equation (Eq. (4.3)), the bulk stress can be written as:

$$\langle \boldsymbol{\sigma} \rangle = \langle \boldsymbol{\sigma} \rangle_f + \frac{1}{A} \int_{\partial A_p} \boldsymbol{t}\boldsymbol{x} \, ds = -\langle p \rangle_f \boldsymbol{I} + 2\eta \langle \boldsymbol{D} \rangle + \frac{1}{A} \int_{\partial A_p} \boldsymbol{t}\boldsymbol{x} \, ds \tag{4.22}$$

where $\boldsymbol{t}$ is the traction force on the particle surface and $\langle \cdot \rangle_f = 1/A \int_{A_f} \cdot \, dA$ is a weighted area average quantity in A_f. Of course, $\langle \boldsymbol{D} \rangle = \langle \boldsymbol{D} \rangle_f$ because the rate-of-deformation tensor is zero inside the particle domain. In Eq. (4.22) the first two terms of the right-hand side represent the fluid contribution and the third term is the contribution of all particles.

We need the stress tensor on the particle boundaries in order to calculate the integral term in Eq. (4.22). However, as shown in the next section, the fictitious domain method cannot accurately evaluate the stress on the particle boundaries due to the discontinuity of the pressure and velocity gradients at the particle boundaries. This problem is circumvented by considering the relation between the Lagrange multipliers and traction forces on the boundary of a particle. For a rigid-ring description, it has been shown [28] that the Lagrange multipliers are related to the traction force on the boundary plus the stress contribution of the fluid inside the rigid ring:

$$\int_{\partial A_p} \boldsymbol{t}\boldsymbol{x} \, ds = \langle \boldsymbol{\lambda}, \boldsymbol{x} \rangle + \int_{A_p} \hat{\boldsymbol{\sigma}} \, dA \tag{4.23}$$

where:

$$\int_{A_p} \hat{\boldsymbol{\sigma}}\, dA = -\int_{A_p} p\, dA\ \boldsymbol{I} + \int_{A_p} 2\eta \boldsymbol{D}\, dA \tag{4.24}$$

Note that, in theory, the fluid inside the rigid ring moves like a rigid body and that $\boldsymbol{D} = \boldsymbol{0}$ inside the rigid ring. In the numerical implementation this is only approximately true. However, the contribution of the rate-of-deformation tensor can still be neglected (see Sec. 4.5) and only the pressure contribution has to be calculated by performing an integration on the particle domain. By combining the Eq. (4.22) and (4.23), we can calculate the bulk stress as follows:

$$\langle \boldsymbol{\sigma} \rangle = \langle \hat{\boldsymbol{\sigma}} \rangle + \frac{1}{A} \langle \boldsymbol{\lambda}, \boldsymbol{x} \rangle \tag{4.25}$$

where $\langle \hat{\boldsymbol{\sigma}} \rangle$ is the average over the full domain (fluid + particles) of the fluid stress tensor (we extended the definition of $\hat{\boldsymbol{\sigma}}$ with $\hat{\boldsymbol{\sigma}} = \boldsymbol{\sigma}$ in the region between the particles).

The fluid contribution to the bulk stress can be recovered as follows:

$$\langle \boldsymbol{\sigma} \rangle_f = \langle \hat{\boldsymbol{\sigma}} \rangle - \frac{1}{A} \int_{A_p} \hat{\boldsymbol{\sigma}}\, dA \tag{4.26}$$

whereas the particle contribution in Eq. (4.22) can be computed using Eq. (4.23). It should be noticed that if one is interested in the bulk stress, it is not necessary to evaluate the integral of fluid stress inside the particles. Instead, if one needs the fluid and particle contribution separately, the integral of fluid stress tensor inside the objects is required.

Finally, it is important to point out that the Eq. (4.25) is valid only if the particles are completely immersed in the computational domain. In our simulation scheme, the particles cross the boundaries of the domain where the bulk properties are computed also. Therefore, a slightly change in the area A will be made, as shown in Section 4.6.

4.5 Code validation

4.5.1 Local fields

The code has been validated through a comparison with a boundary fitted method (BFM) using a commercial code ($PolyFlow^{©}$). First, pressure and velocity fields have been investigated. A simple system as test problem is chosen: a single particle is collocated at the center of a square domain; on the sides of the square planar elongational boundary conditions are imposed ($\dot{\epsilon} = 0.5$) and a unit viscosity is chosen. The radius of the particle is chosen equal to 0.05 and the square side is 20 times this radius ($R_p = 0.05, L_x = L_y = 1.0$). In order to preserve the symmetry of the problem, the particle does not move or rotate, so the no-slip boundary conditions on the particle surface for BFM are $u = v = 0$. Of course, the fictitious domain method (FDM) does not need to specify particle boundary conditions because the no-slip conditions are imposed through Lagrange multipliers on the collocation

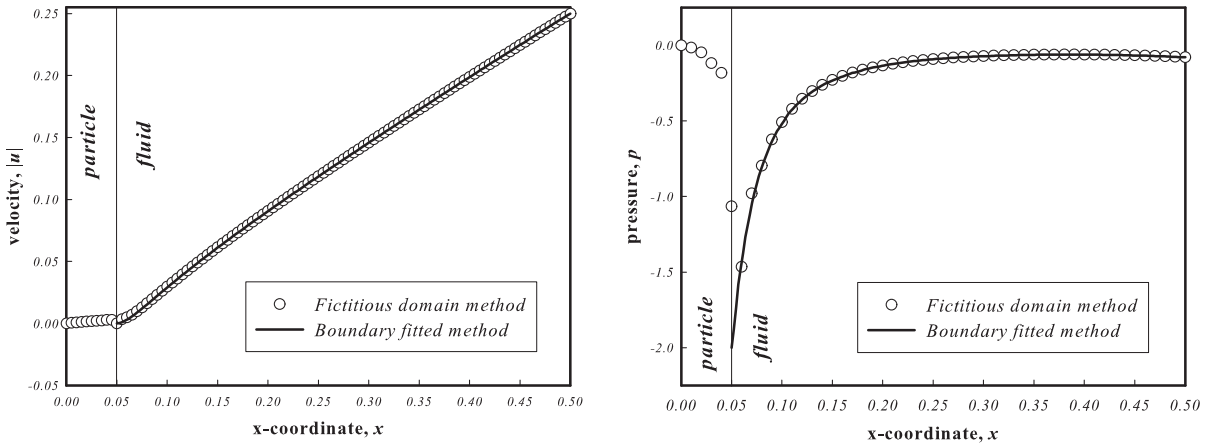

Figure 4.3: Velocity (left) and pressure (right) field on the positive x-axis, as predicted by the boundary fitted method (solid line) and a fictitious domain method (open circles).

points. A very fine triangular mesh is used in the BFM, finer close to the particle where larger gradients are expected (typical element size close to the particle is 0.005, i.e. 10 times smaller than the particle radius). A regular square mesh for FDM is used. The side of the square element is chosen 1/100 the square domain so a 100x100 grid is considered. The particle surface is discretized by 28 collocation points, chosen equally distributed on the particle boundary. This choice corresponds approximately to one point per element. As shown later, this distribution of collocation points is the optimal choice for this particle radius/element dimension ratio. The pressure is set to zero in the bottom-left corner of the square domain. Finally, a quadratic interpolation for the velocity and linear continuous interpolation for the pressure is chosen for BFM. The steady state problem is solved by means of BFM and FDM and pressure and velocity fields are compared.

In Figure 4.3, the pressure and velocity behavior along the positive x-axis is shown. First of all, notice that the FDM solution has field values also inside the particle. The velocity magnitude predicted by FDM (open circles) matches the BFM one (solid line). Moreover, FDM predicts a zero-value for the velocity inside the particle (the particle does not move), as expected. The results are different for the pressure field. Both methods predict a pressure value near zero far from the particle (of course the set pressure level on the external fluid boundaries is expected). Approaching the particle, a monotonically decreasing behavior is predicted by the BFM solution that matches the FDM solution up to a small distance from the particle surface (≈ 0.01). The BFM solution shows a minimum value on the particle surface whereas for the FDM case the pressure increases slightly. It has to be pointed out that: i) a different value of pressure is predicted on the particle boundary and ii) the pressure inside the particle is not constant (and is not zero everywhere).

This different behavior can be justified by considering that the pressure is discontinuous

across the particle boundary. The BFM "doesn't see" this discontinuity since only the fluid domain is considered; the interior of the particle is not a part of the solution. Instead, in the FDM, the particle domain is discretized as well and, to take into account the discontinuity, a very fine mesh close to the particle surface is required. Indeed, since the interpolating functions are continuous inside an element, a finer mesh can reduce the distance where the pressure goes from the minimum to zero value. However, the pressure value on the surface cannot be predicted as accurately as a BFM. Of course, the stress tensor is affected by the same problem, since it has a pressure contribution (see Eq. (4.3)). As a consequence, the bulk stress cannot be accurately evaluated using Eq. (4.21) (or (4.22)) but we will use Eq. (4.25) where only the stress over the total domain and the Lagrange multipliers are required.

A discontinuous interpolation for the pressure has also been implemented ($Q_2 - P_1^d$ element). The results (not presented) show the same behavior: the pressure predicted by the FDM follows the BFM one up to a very close distance from the particle boundary, then goes up. Therefore, a discontinuous interpolation for the pressure is not able to predict the value of pressure on the particle boundary either, since, the pressure is discontinuous between the elements but continuous inside an element. In this work, a continuous interpolation is used.

4.5.2 Bulk stress

For the rigid-ring description, only the boundaries of the particle domain need to be discretized. The rigid-body motion is enforced through Lagrange multipliers, by means of collocation points. Moreover, we can recover the bulk stress of the suspension from the

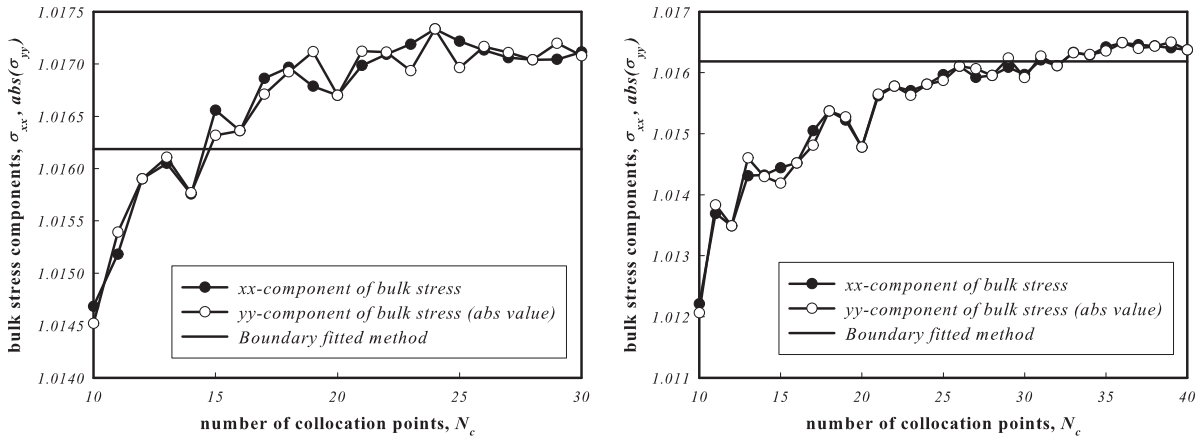

Figure 4.4: Bulk stress as a function of the number of collocation points for 50x50 (on the left) and 100x100 (on the right) grid. The close circles refer to the $xx-$component whereas with the open circles the absolute value of the $yy-$component is depicted. The straight line is the BFM prediction.

Lagrange multipliers, as stated in the previous Section.

In this paragraph, we show that the number of collocation points is a crucial choice for the accuracy of the bulk stress tensor. Of course, by fixing the number of collocation points, the orientation of the collocation point grid on the particle boundaries should not affect the bulk stress value. We will show this as well. Again, the same test problem is considered.

In Figure 4.4, the $xx-$component (plotted with full circles) and the absolute values of the $yy-$component (open circles) of the bulk stress versus the number of collocation points (N_c) are shown for a fluid viscosity $\eta = 1$. The straight line is the value of the bulk stress obtained by a boundary fitted method. On the left, the results for a 50x50 grid are plotted. On the right, a twice finer grid is considered. In both cases, the trend is upwards. A small number of points leads to an underestimation of the bulk stress. On the other hand, after using a large number points an overestimated stress value is obtained. Moreover, after a critical N_c value, the bulk stress does not increase anymore. Note, that the fluid contribution to the bulk stress has a value of 1. The particle contribution is much smaller but since the error can mostly be attributed to the error in the particle contribution, the error for a large number of points is approximately 6% and 2% in the 50x50 and 100x100 grid, respectively. An optimal value of N_c, say $N_{c,\mathrm{opt}}$, exists ($N_{c,\mathrm{opt}} \cong 15$ for a 50x50 mesh, $N_{c,\mathrm{opt}} \cong 28$ for a 100x100 mesh), where the error is minimal. These optimal values correspond to about one collocation point for each element, in agreement with Hwang et al. [28, 27]. Of course, $N_{c,\mathrm{opt}}$ depends on the grid resolution as well as on the dimensions of the particles. Since we will change the radius of the particles, a preliminary analysis on the optimal choice of N_c is carried out. For each radius exploited we solve the test problem for

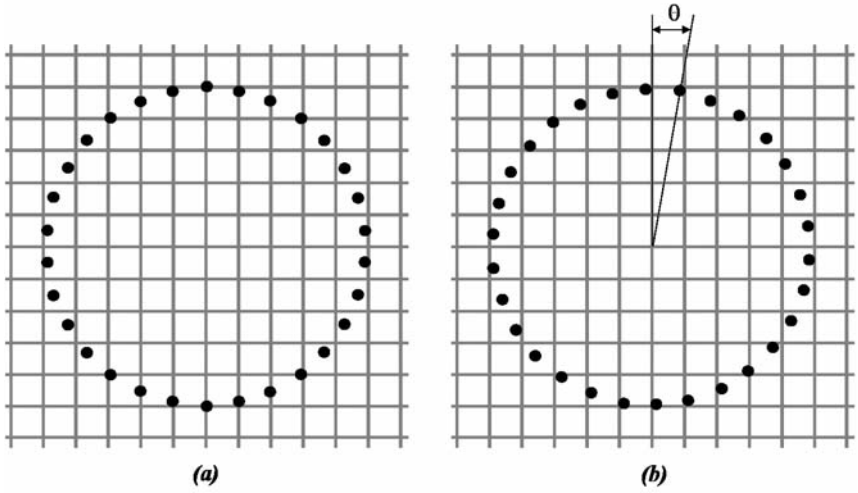

Figure 4.5: Collocation point distribution on the boundary of a particle located at the center of the square domain. 30 equally distributed points are considered. On the left, the first collocation point lies on the highest point of the circle. On the right the same grid is rotated of $\theta = 10°$.

different N_c and we compare the results with the bulk stress from the BFM. Then, $N_{c,\mathrm{opt}}$ is evaluated and the number of the collocation points of the particles in the suspension is set equal to $N_{c,\mathrm{opt}}$.

Next, we check whether the bulk stress is independent of the orientation of the collocation point grid. Let us consider again the simple test problem of one particle at the center of the domain, with the same parameters but with 30 collocation points instead of 28. Initially, we choose equally distributed points starting from the top of the particle (see Figure 4.5a). The steady state problem is solved and the bulk stress is calculated as stated in Eq. (4.25). The same problem is solved, but this time the collocation points are rotated by an angle θ with respect to the previous configuration, as shown in the Figure 4.5b. This procedure is repeated for many θ and the results are plotted in Figure 4.6 (full circles represent the $xx-$component of the bulk stress whereas open circles are the absolute value of the yy-component). The phase shift angle θ ranges in $I_\theta = [0, \pi/15]$ since, for $N_c = 30$ and for different θ, the same configurations can be recovered. The straight line is the bulk stress calculated by the boundary fitted method. We can see that the quantities plotted are nearly independent of the rotation of the collocation point grid and they match the bulk stress evaluated by means of the BFM. So, the orientation of the grid does not affect the bulk stress. Although in our simulations we use $\theta = 0$, the results show that the accuracy of the bulk stress is not related to the specific symmetry of the collocation points with respect to the fluid mesh. This also indicates that the collocation method can be easily extended to non-circular particles, where the orientation of the collocation points cannot be fixed.

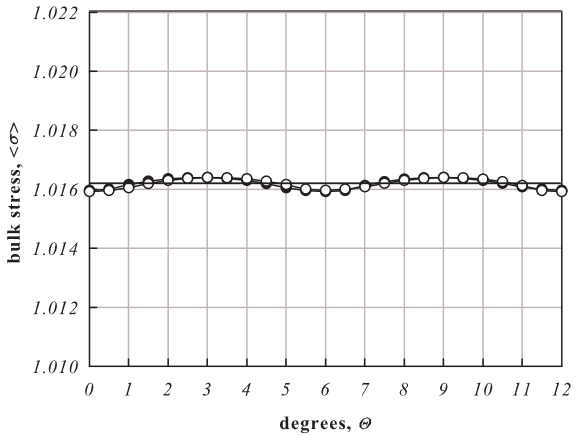

Figure 4.6: Bulk stress versus the phase shift angle. The close circles refer to the xx-component whereas with the open circles the absolute value of the yy-component is depicted.

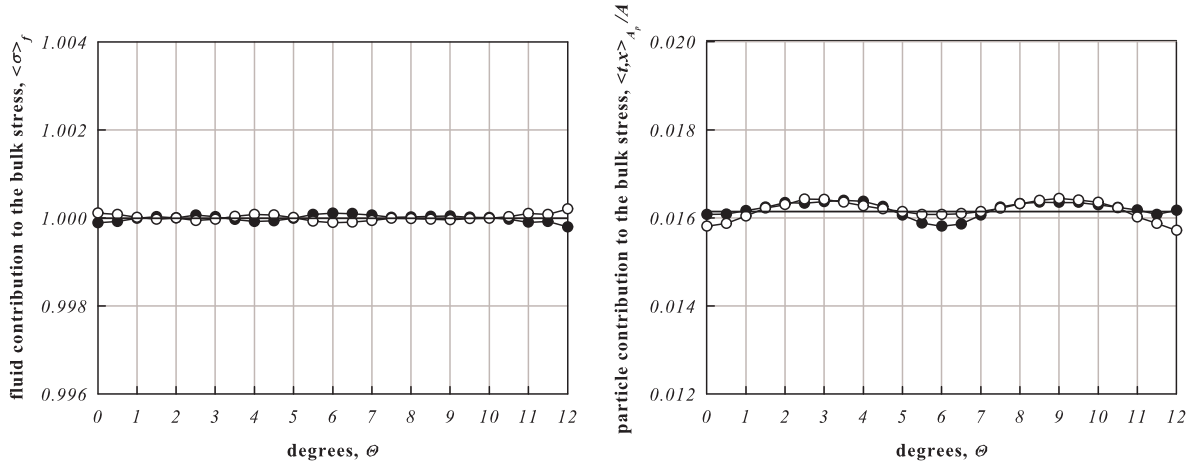

Figure 4.7: Fluid (on the left) and particle (on the right) contributions to the bulk stress. These quantities have been obtained by using the Eq. (4.26) and (4.23) (divided by the area A), respectively. The close circles refer to the xx-component whereas with the open circles the absolute value of the yy-component is depicted.

4.5.3 Fluid and particle contribution to the bulk stress

A validation of Eqs. (4.23) and (4.26) for recovering the particle and fluid contribution is carried out. By performing the procedure previously discussed, the traction force term (from Eq. (4.23) divided by the area A) and $\langle \boldsymbol{\sigma} \rangle_f$ (from Eq. (4.26)) are plotted as a function of θ in Figure 4.7 (with the same meaning of the symbol as in Figure 4.6). Notice that in both integrals the contribution of $\langle \boldsymbol{\sigma} \rangle$ inside the particle is taken into account. Again, the quantities plotted are nearly independent of the rotation of the collocation points grid and they match the fluid and particle contribution to the bulk stress evaluated by means of the BFM.

Finally, the integral of the pressure inside the particle (divided by the area A) as a function of θ is shown in Figure 4.8. A Monte Carlo integration has been used, as the Gaussian quadrature formula is difficult to implement. The integral of $\boldsymbol{D}$ has also been evaluated and it is about 10^{-5}, for every θ. The values are not small compared to particle contribution. They also depend on the angle θ, which stresses the fact that the fluid pressure inside the particle has a numerical origin. Hence, we conclude that the internal stress integral (Eq. (4.24)) is not small and fully dominated by the pressure term. As a consequence, the $\boldsymbol{D}$ term can be neglected.

In conclusion, the fluid and particle contribution to the bulk stress can be evaluated using the Eqs. (4.23) and (4.26) together with Eq. (4.23), where the integral of $\boldsymbol{D}$ inside the particle can be neglected. If only the total bulk stress is required, Eq. (4.25) can be used and no integration inside the particle is necessary.

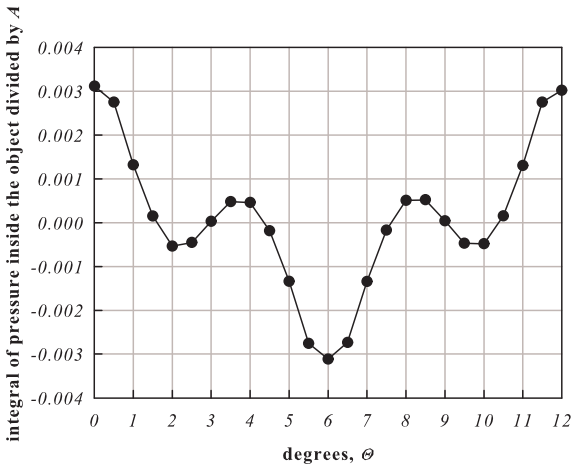

Figure 4.8: Integral of the fluid pressure inside the particle (divided by the area A) versus the phase shift angle. A Monte Carlo integration has been used.

4.6 Simulation procedure

4.6.1 Basics

In this section, the simulation procedure is presented. The basic idea is to simulate a computationally small domain that is able to describe the bulk properties of the suspension. For this purpose, i) a sufficiently high number of particles is required and ii) only the hydrodynamic interactions should influence the particles or, in other words, the particles

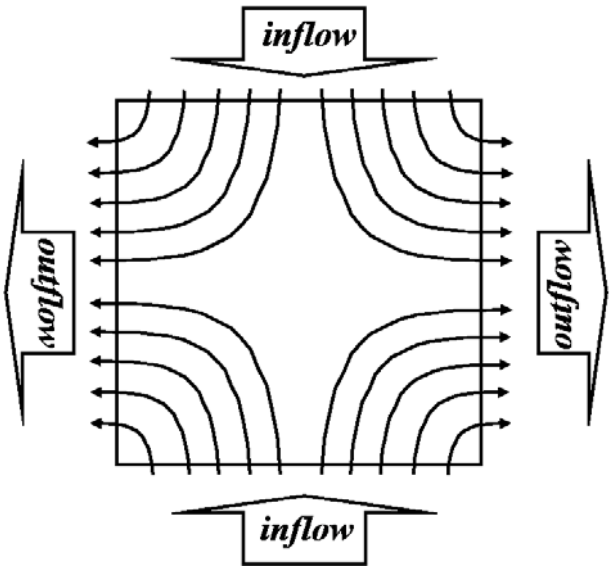

Figure 4.9: Schematic representation of the streamlines for a unfilled Newtonian fluid in a planar elongational flow. Two inflow sections and two outflow sections can be distinguished.

should not feel the presence of the boundary conditions imposed on the external side of the square domain.

Let us consider an unfilled Newtonian fluid in a planar elongational flow, as depicted in Figure 4.9. The typical streamlines are portrayed and two inflow and two outflow sections can be distinguished (see also Eq. (4.5)). Now, let us insert rigid particles inside the fluid. For simplicity, we will consider three particles only. The simulation procedure is schematized in Figure 4.10.

In this picture, four time sequence frames of the procedure are shown. Initially (first frame, $t = 0$), the particles are positioned randomly inside the fluid. Each time step the governing equations are solved, local fields can be evaluated and the particle positions are updated. The particles will move according to the streamlines and the hydrodynamic interactions as well (second frame). In the next time step, the particles will change configuration again (third frame). Note that the particle number "2" is very close to the right boundary of the domain, so, in the next time step, it would partly go out. Then, in the next time step, the particle "2" is randomly relocated on one of the two inflow sections (fourth frame). It is important to point out that the inflow section is randomly chosen as well as the position of the particle on this section. After the relocation, the equations are solved again and the particle positions are updated as stated by the kinematic equations, and so on. When a particle is relocated, its position in the next time step cannot be updated using the Adams-Bashforth algorithm (Eq. (4.20)), since the velocity in the previous time step (before the relocation) is required. So, only for this step, the Euler method (Eq. (4.19)) is used.

A schematic representation of the computational domain used in our simulations is depicted in Figure 4.11. Three different regions can be distinguished: an internal region ($A-$region), an intermediate region ($B-$region) and an external region ($C-$region).

In the $A-$region the particles can move and only in this region the bulk properties are evaluated. So, this region can be considered as a sample for the whole suspension.

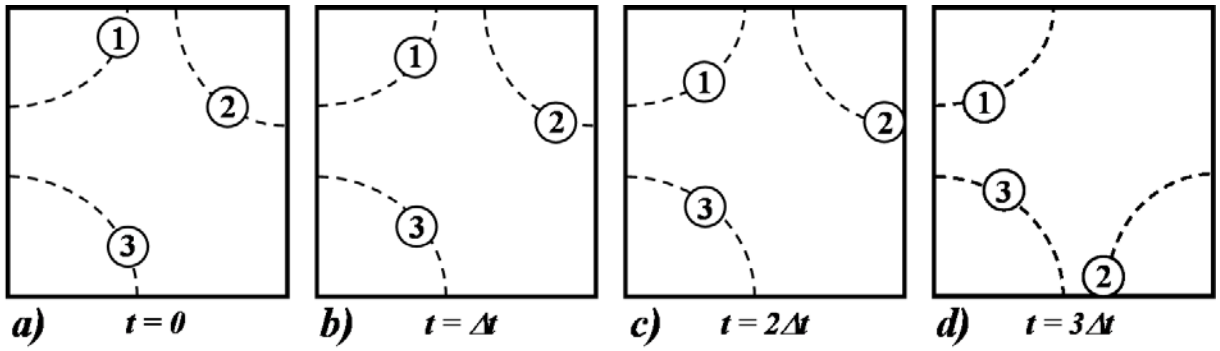

Figure 4.10: Scheme of the simulation procedure: (a) initially, the particles are randomly distributed in the fluid; (b) the particles move according to the streamlines and hydrodynamic interactions; (c) the particle "2" is close to the boundary; (d) the particle "2" is randomly relocated on one of the two inflow sections.

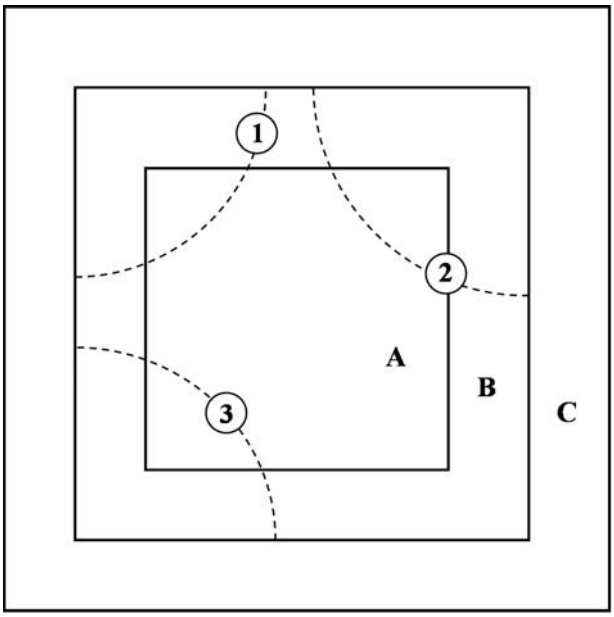

Figure 4.11: Schematic representation of the computational domain. The particles can move in the $A-$ and $B-$regions. Only in the $A-$region the bulk calculations are performed. When a particle crosses the outflow sections of the $B-$region, it is relocated on the inflow sections of the same region. The elongational flow conditions are imposed on the $C-$region external boundaries.

In the $B-$region the particles can move as well and, when they cross the outflow boundaries of it, they are relocated randomly on one of the two inflow sections of the same region. Therefore, the particles in this region affect the particles in the sample $A-$region, as should be because the sample region should be surrounded by the remainder part of the suspension. Moreover, for viscoelastic simulations, this region is mandatory because the stress surrounding the particles, after the relocation, needs time to develop before the particles enter in the $A-$region in order to achieve a "developed" state (in a statistical meaning).

The $C-$region is particle free, i.e., no particle can enter such region. This region is indeed necessary to avoid that particles could affect the elongational flow boundary conditions, Eqs. (4.5), which are imposed on the external boundaries of $C-$region. In the absence of $C-$region one would observe strong fluctuations in the local pressure field that result for the perturbation of the imposed boundary conditions due to exiting/entering particles. The width of $C-$region has to be chosen large enough with respect to particle radius.

As explained below, the particle area fraction (ϕ) in the $A-$region for this scheme changes in time. Indeed, the number of particles in the $A-$region is not constant. Therefore, simulation of very dilute systems ($0.0 < \phi < 0.05$) must be performed sufficiently long in order to get accurate statistical averages.

4.6.2 Particle area fraction and bulk stress

All the calculations concerning particle area fraction, viscosity and bulk stresses are performed in the $A-$region of the computational domain, even if the particles can move in the middle region as well. So a situation where particles are partially inside the A-region can occur (see the particle "2" in Figure 4.11).

As a consequence, the particle area fraction and bulk stress evaluations are not trivial. For each particle configuration (= each time step), the particle area fraction is calculated as follows:

$$\phi = \frac{\sum_{i=1}^{N_{\text{int}}} \pi R_{\text{p},i}^2 + \sum_{i=1}^{N_{\text{cross}}} A_{\text{c},i}}{A_{A\text{-region}}} \tag{4.27}$$

The first summation refers to the particles that are completely inside the $A-$region and N_{int} is the number of these particles. The second summation takes into account the areas inside the $A-$region of the particles crossing this region (marked areas in Figure 4.12). Therefore, in Eq. (4.27), N_{cross} is the number of the particles crossing the boundaries and $A_{\text{c},i}$ is the area inside the $A-$square of these particles. Finally $A_{A\text{-region}}$ is the area of the $A-$region. The marked areas in Figure 4.12 are evaluated by implementing geometric rules ($P_{\text{c},i-1}$ and $P_{\text{c},i}$ particles in the figure) or through a Monte Carlo integration if the particle crosses the corner of the $A-$region ($P_{\text{c},i+1}$ particle in the figure).

The bulk stress formula is slightly more complicated. The bulk stress expression Eq. (4.25) is valid only if the particles are completely immersed in the domain. However, if a particle crosses the boundary of the domain where the bulk properties are evaluated (A-region), the contribution of the particle is the stress integral on the part of the particle domain that is inside this region. The 'real' stress inside a rigid particle is unknown and it is not possible to compute the stress contribution of such a particle. So, we have to modify the domain such that all particles are fully included in the domain, but the 'average' domain (in time and space) should still approximate the A-region.

Let us consider Figure 4.13. The new computational domain is enclosed by the bold line: it is given by the A-domain plus the external part of the particles crossing the square

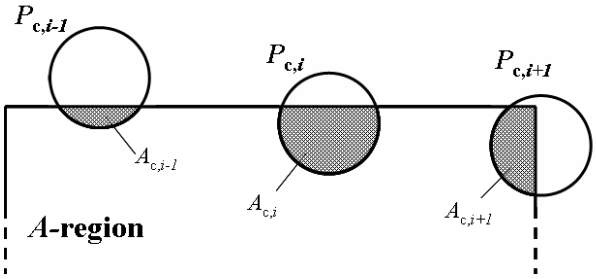

Figure 4.12: Relative positions of the particles crossing the boundaries of the $A-$region. The summation of marked regions gives the particle area inside the square of these particles.

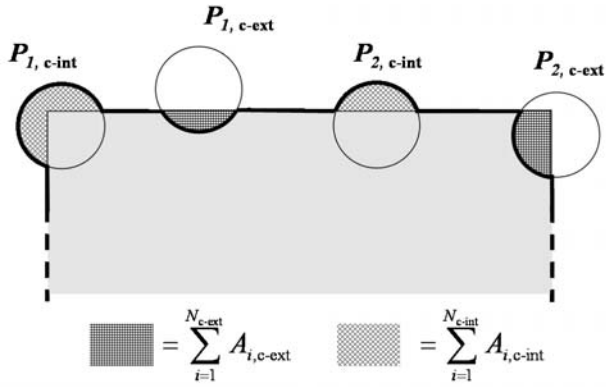

Figure 4.13: Relative positions of particles crossing the boundaries of the A-region. The bulk stress is evaluated in a modified domain, included inside the bold line: the square region plus the external part of the particles crossing the square boundaries and with the center inside the square (diagonal marked areas) minus the internal part of the particles crossing the square boundaries and with the center outside the square (square marked areas).

boundaries and with the center inside the square (diagonal marked areas) minus the internal part of the particles crossing the square boundaries and with the center outside the square (square marked areas). So, a particle gives a contribution to the bulk stress only if it is completely inside the A-region or if it crosses the boundary of the A-region and has the center inside it. As a consequence, when a particle crosses the $A-$region inflow boundary, it will not give contribution until its center is inside this region and vice versa for the outflow boundary. In this way, on the average in time, the right contribution to the bulk stress of the particles crossing the $A-$region can be recovered.

According to this change, we can apply the Eq. (4.25) to the new extended domain. So, the bulk stress formula can be written as:

$$\langle \boldsymbol{\sigma} \rangle = \frac{\displaystyle\int_{A\text{-region}} \hat{\boldsymbol{\sigma}}\, dA - \int_{\sum A_{\text{c-int}}} p\, dA\; \boldsymbol{I} + \int_{\sum A_{\text{c-ext}}} p\, dA\; \boldsymbol{I} + \sum_{i=1}^{N_{\text{int}}+N_{\text{c-int}}} \langle \boldsymbol{\lambda}, \boldsymbol{x} \rangle_i}{A_{A\text{-region}} + \displaystyle\sum_{i=1}^{N_{\text{c-int}}} A_{\text{c-int},i} - \sum_{i=1}^{N_{\text{c-ext}}} A_{\text{c-ext},i}} \tag{4.28}$$

where $N_{\text{c-int}}$ and $N_{\text{c-ext}}$ are the number of particles crossing the boundaries with the center inside and outside the A-region, respectively; $A_{\text{c-int}}$ and $A_{\text{c-ext}}$ are the areas shown in Figure 4.13. We have some remarks on Eq. (4.28): i) the area of the extended domain is given by the denominator of the formula, ii) $\langle \hat{\boldsymbol{\sigma}} \rangle$ is split into $\langle \hat{\boldsymbol{\sigma}} \rangle_{A\text{-region}} + \langle \hat{\boldsymbol{\sigma}} \rangle_{A_{\text{c-int}}} - \langle \hat{\boldsymbol{\sigma}} \rangle_{A_{\text{c-ext}}}$, iii) the last two terms, i.e. $\langle \hat{\boldsymbol{\sigma}} \rangle_{A_{\text{c-int}}} - \langle \hat{\boldsymbol{\sigma}} \rangle_{A_{\text{c-ext}}}$, are approximated by using the pressure term only, similar to procedure for approximating Eq. (4.24).

To apply this formula, one needs to evaluate the integral of the pressure on $A_{\text{c-int}}$ and $A_{\text{c-ext}}$. This integral is calculated again by performing a Monte Carlo integration. For

many particles, this method could be expensive in computational time. However, 10000 random points are shown to be sufficient for a good accuracy.

4.7 Results

In this Section, the results for Newtonian suspensions are presented. To predict the bulk properties of the suspension a high number of particles has to be chosen. Simulations are performed for 150 particles in the whole computational domain. The number of particles chosen is supposed to be sufficiently high so the average properties of the computational domain can adequately describe the suspension ones. In fact, we expect that no changes in the bulk properties occur with increasing the number of particles and keeping the area fraction the same by changing the size. This was checked by increasing the number of particles to 225 and evaluating the new viscosities. For simulation of dilute systems a smaller number of particles is used since the particle size cannot be reduced too much (the smallest particle we use has about 4×4 elements inside, as depicted in Figure 4.2).

The domain is discretized by regular square and trapezoidal elements, as depicted in Figure 4.14. Regular squares are used for the A- and B-region, because the particles can move here. No fine mesh is needed for the C-region since the particles cannot enter there: a coarser trapezoidal mesh is used, saving memory and CPU time. In particular, a finer trapezoidal element is chosen close to the B-region boundaries. In this way, when a particle is relocated, the local fields around the particle in the C-region can be accurately solved. The mesh convergence has been verified and the mesh parameters are reported in Table 4.1. The C-region is chosen sufficiently large so that the particles with the highest radius exploited can not feel the presence of the boundaries. Finally, a pressure value of zero is set on the south-west corner of the whole domain.

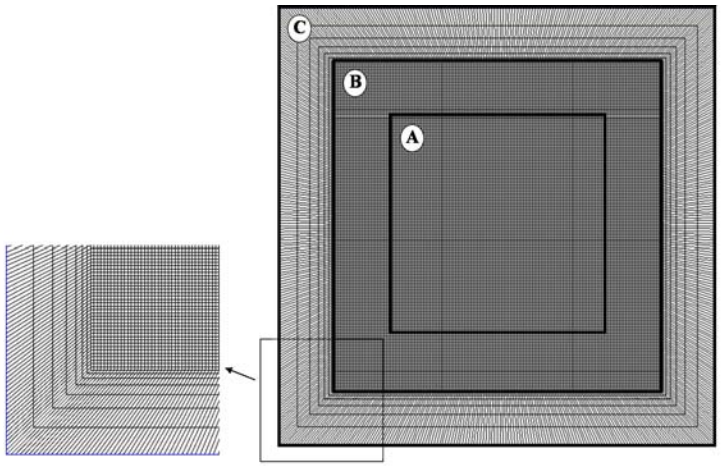

Figure 4.14: Mesh used in the simulations. A- and B-region are discretized through a regular square mesh. A trapezoidal coarser mesh is used for C-region, since the particles cannot enter in this region.

Table 4.1: Mesh parameters.

Symbol	Description	Value
$l_{x,A}$	Length of the A-region in the x-direction	1.0
$l_{y,A}$	Length of the A-region in the y-direction	1.0
$n_{x,A}$	Number of elements of the A-region in the x-direction	100
$n_{y,A}$	Number of elements of the A-region in the y-direction	100
$l_{x,B}$	Distance between the A- and B-region in the x-direction	0.25
$l_{y,B}$	Distance between the A- and B-region in the y-direction	0.25
$n_{x,B}$	Number of elements between the A- and B-region in the x-direction	25
$n_{y,B}$	Number of elements between the A- and B-region in the y-direction	25
$l_{x,C}$	Distance between the B- and C-region in the x-direction	0.25
$l_{y,C}$	Distance between the B- and C-region in the y-direction	0.25
$n_{x,C}$	Number of elements between the B- and C-region in the x-direction	7
$n_{y,C}$	Number of elements between the B- and C-region in the y-direction	7

Figure 4.15 shows a typical initial configuration: 150 equal-sized particles ($R_p = 0.03$) are randomly distributed inside the A- and B-region. Some particles cross the A-region boundaries and no particle is located in the C-region.

All the simulations are performed with $\dot{\epsilon} = 0.5$, $\eta = 1.0$, $\triangle t = 0.05$. No artificial repulsive force is implemented because particle collisions hardly occur, when choosing a sufficiently small time step and fine mesh. Anyway, when a collision occurs the particles slightly overlap. The overlapping lead to a single bigger particle with about zero stress inside: the bulk properties are hardly affected from this configuration. Moreover, the particles can also separate again. The contour plots (for $\dot{\epsilon}t = 2.5$) of the magnitude of the velocity vector, pressure and xx-component of the stress tensor are depicted in the Figures 4.16, 4.17 and 4.18, respectively, for a total of 150 equal-sized particles ($R_p = 0.03$). In these pictures, only the A-region is shown.

First of all, we can see that the presence of the particles modifies the circular concentric velocity field that is typical for an unfilled fluid in an elongational flow. Moreover, the strong influence of the hydrodynamic interactions between the particles is clear: the objects, especially at the center of domain, do not follow the streamlines but the motion is modified by the presence of the other particles.

The local pressure field (see Figure 4.17) shows the highest values (white zones) along the vertical direction between two particles and the lowest values along the horizontal one (dark regions). This agrees with the dilute theories. Of course, the local stress tensor σ_{xx} (see Figure 4.18) shows an opposite behavior. Finally, pressure and stress are larger in absolute value if the particles are close to each other. This effect leads to an increase of the viscosity with increasing the particle area fraction (see below).

In Figure 4.19, the particle area fraction in the A-region versus time is plotted. As mentioned earlier the number of particles in that region is not constant. As a result the particle area fraction is also not constant, but it is a continuous function of time due to the way the particles on the boundary of the A-region are taken into account (see Eq. (4.27)).

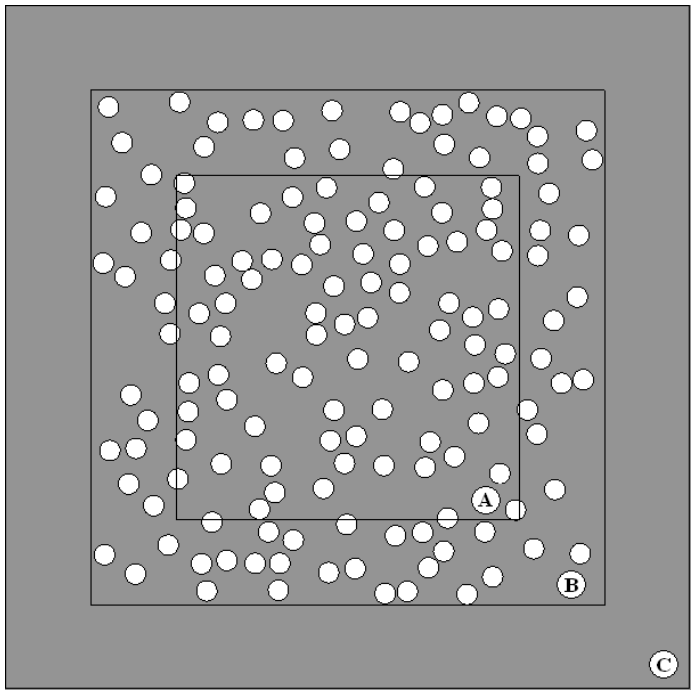

Figure 4.15: Initial random distribution of a 150-particle system ($R_p = 0.03$). Only the A- and B-region are filled.

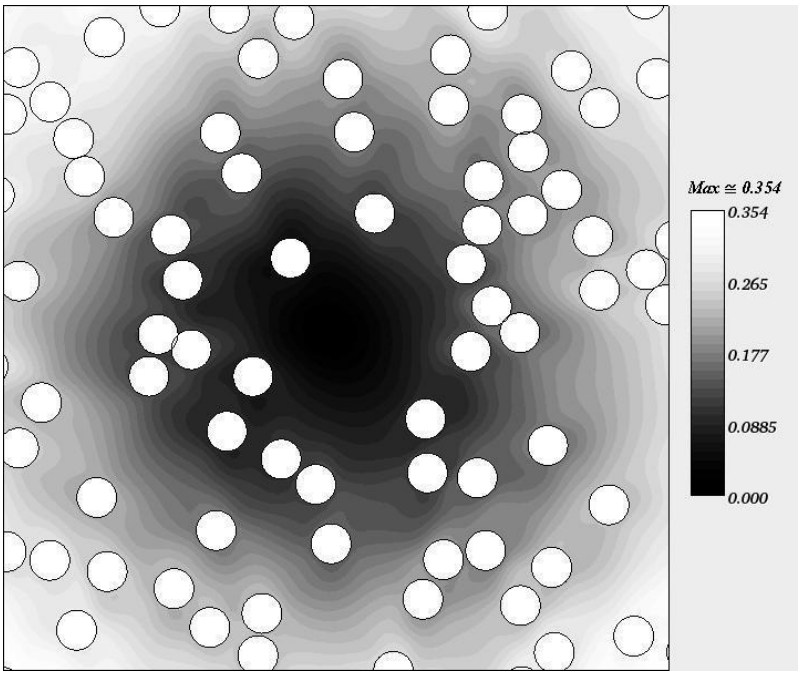

Figure 4.16: Contour plot of the velocity magnitude for the 150-particle system ($\dot{\epsilon}t = 2.5$).

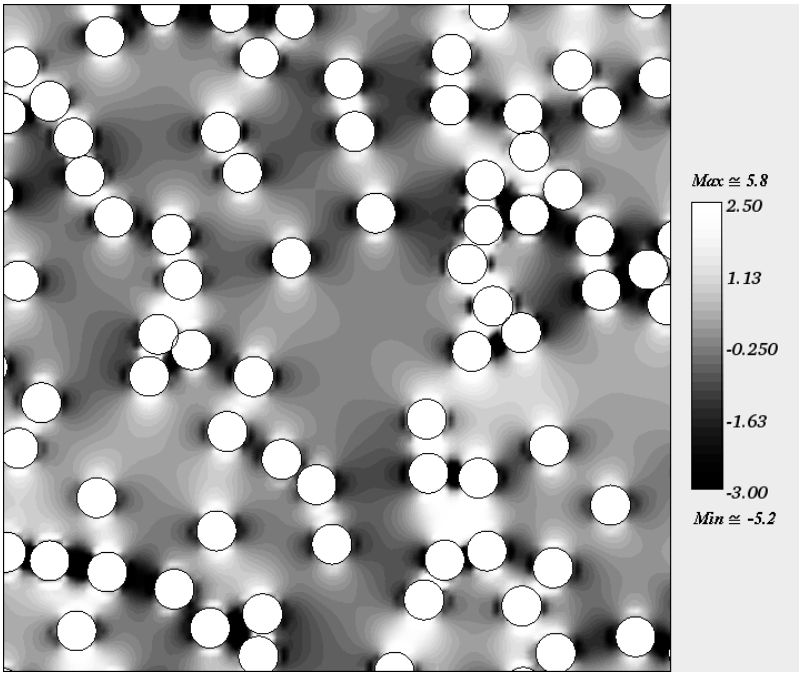

Figure 4.17: Contour plot of the pressure for the 150-particle system ($\dot{\epsilon}t = 2.5$).

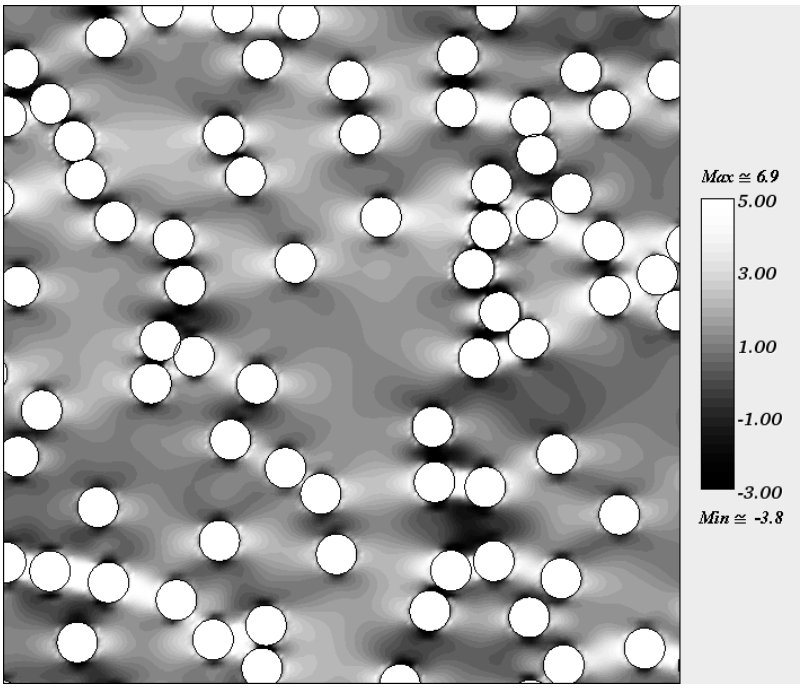

Figure 4.18: Contour plot of the xx-component of the stress tensor for the 150-particle system ($\dot{\epsilon}t = 2.5$).

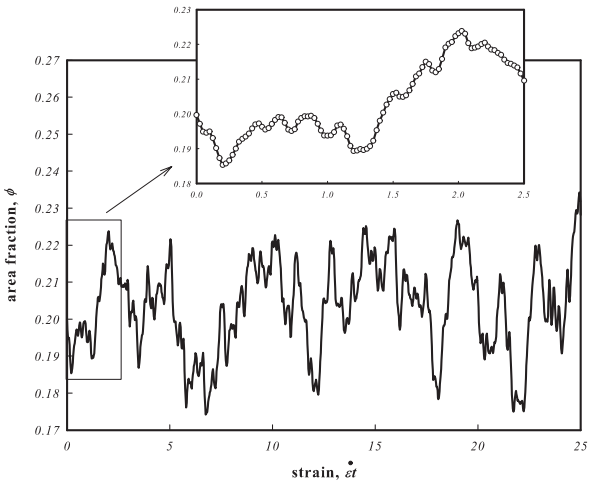

Figure 4.19: Particle area fraction as a function of the strain for the 150-particle system and $R_p = 0.03$. The particle area fraction is evaluated only into the A-region where the number of particles is not constant (Eq. (4.27)). Indeed, $\phi(\dot{\epsilon}t)$ is a continuous function of the time.

The xx- and yy-component of the bulk stress tensor are shown in Figure 4.20. Contrary to the particle area fraction, these functions are discontinuous. The reason can be understood considering the formula for the evaluation of the bulk stress, Eq. (4.28). When a

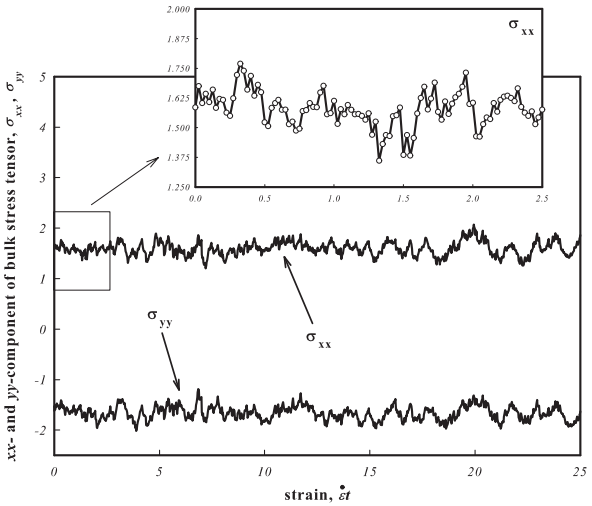

Figure 4.20: $xx-$ and $yy-$component of the bulk stress tensor as a function of the strain for the 150-particle system. These components are evaluated only into the A-region where the number of particles is not constant (Eq. 4.28).

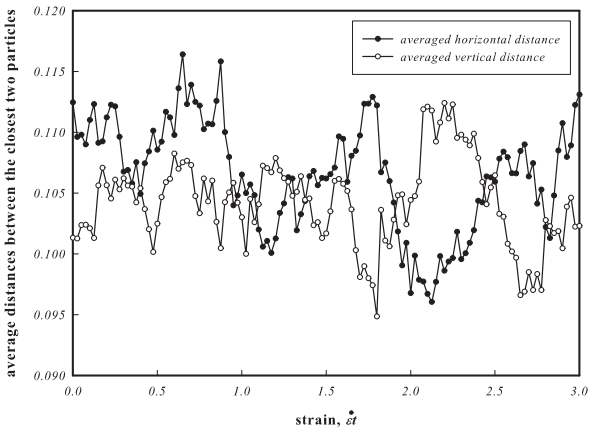

Figure 4.21: Average horizontal and vertical distances between the two closest particles as a function of the strain (evaluated according to [29]). Fluctuations around a mean value can be observed and no transient phase occurs.

particle crosses the boundaries of the A-region and the center is outside this region, it does not give a contribution to the bulk stress. As soon as the center of the particle is inside the A-region, the contribution of the particle is immediately taken into account. This leads to a "jump" into the bulk stress components. However, this jump is relatively small because the contribution of only one particle is only a small part of the total stress. Averaging the stress in time will smooth out these jumps.

The Figure 4.20 clearly shows that the two components of the bulk stress fluctuate around a mean value. However, no transient behavior occurs contrarily to the results of Hwang and Hulsen [29].

The average values of the stress components over 2000 time steps are: $\overline{\sigma}_{xx} = 1.603$ and $\overline{\sigma}_{yy} = -1.656$. Hence, a deviation between the absolute values of the average stress components exists (we verified that this discrepancy is independent from the chosen number of the time steps). This suggests the existence of an anisotropic structure, as reported in [29]. In order to verify this anisotropy, we use the same method of [29], by introducing an average horizontal and vertical distance between the two closest particles. The horizontal distance for each particle to the others is defined by considering the horizontal distance to the closest particle within an angular window of $\pm 45°$ about the $x-$axis. The vertical distance is defined similarly but now using $\pm 45°$ about the $y-$axis. By evaluating the two distances for every particle and by averaging over the total particle number, the plot in the Figure 4.21 is obtained. Firstly, no transient phase is observed. Furthermore, the distances fluctuate around two mean values that are 0.111 for the horizontal distance and 0.106 for the vertical one. So, we can conclude that a small anisotropy in the structure exists: the particles are slightly farther apart along the horizontal direction than along the vertical one. Note, that our calculations predict an anisotropy less pronounced than in [29] (the deviation between the two average distances is about 4% of their average value whereas it

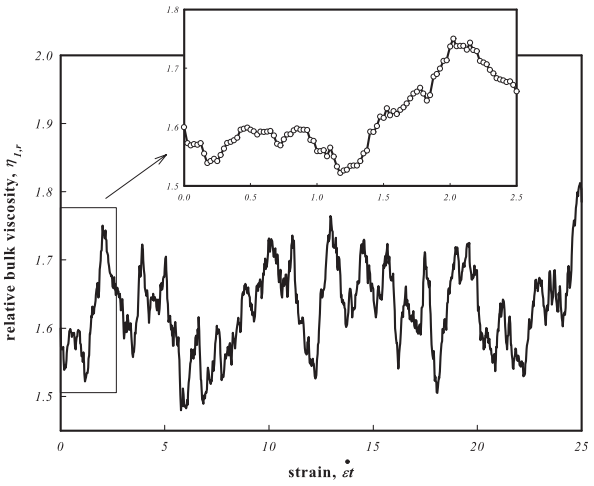

Figure 4.22: Relative bulk viscosity as a function of the strain for the 150-particle system. The viscosity is evaluated only in the A-region where the number of particles is not constant (Eq. (4.29)).

is 14% in [29]).

As expected, the $xy-$component of the stress tensor (not shown) fluctuates around a mean value that is very close to zero (the fluctuations are about $\pm 0.03 \div 0.04$).

Finally, in Figure 4.22, the relative bulk viscosity:

$$\eta_{1,r} = \frac{\eta_1}{4\eta_0} = \frac{\sigma_{xx} - \sigma_{yy}}{\dot{\epsilon}_{\text{eff}}} \cdot \frac{1}{4\eta_0} \tag{4.29}$$

is plotted. In Eq. (4.29), σ_{xx} and σ_{yy} are the xx- and yy-component of the bulk stress tensor, η_0 is the zero-shear-rate viscosity and $\dot{\epsilon}_{\text{eff}}$ is an effective elongational rate evaluated by performing the integral of $\boldsymbol{D}$ over the $A-$region for every particle configuration. Of course, $\dot{\epsilon}_{\text{eff}}$ is a function of time since the particle distribution changes each time step. The fluctuations in $\dot{\epsilon}_{\text{eff}}$ are small and the time average value is slightly below the imposed $\dot{\epsilon}$. For example, for $\phi = 0.277$ we find the average value of $\dot{\epsilon}_{\text{eff}} = 0.485$. The factor "4" in Eq. (4.29) is due to the bi-dimensional Trouton ratio. A similarity between particle area fraction and viscosity trends can be noticed, which confirms what said previously: a higher particle area fraction increases the bulk viscosity. It is possible to recover the average properties of suspension by averaging over a sufficient high number of configurations (= time steps). In our simulations, 2000 time steps are considered to be enough since the average values do not change anymore. In Figure 4.23, the results are shown. In particular, the average relative bulk viscosity:

$$\overline{\eta}_{1,r} = \frac{\overline{\eta}_1}{4\eta_0} = \left\langle \frac{\sigma_{xx} - \sigma_{yy}}{\dot{\epsilon}_{\text{eff}}} \right\rangle \cdot \frac{1}{4\eta_0} \tag{4.30}$$

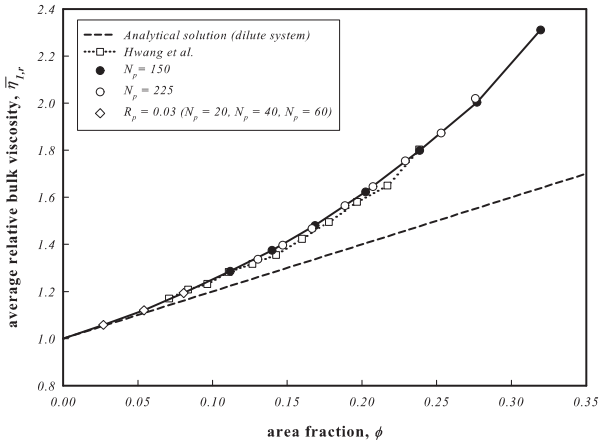

Figure 4.23: Relative bulk viscosity as a function of the particle area fraction for a 150-particle (full circles) and 225-particle system (open circles). Hwang and Hulsen results [29] are plotted as well (open squares). The dilute systems are simulated by considering a small number of particles (open diamonds).

versus the average particle area fraction is plotted. The dashed line refers to the well known Einstein prediction for dilute systems (for the 2D case) [8]:

$$\eta_{Ein} = \frac{\overline{\eta}_1}{4\eta_0} = 1 + 2\phi \tag{4.31}$$

that is valid for $\phi \leq 0.05$. For higher particle area fractions, hydrodynamic interactions cannot be neglected anymore. The circles represent our predictions for 150 (full circles) and 225 (open circles) particles: each circle corresponds to a simulation and the particle area fraction is varied by changing the particle radius. Strongly dilute systems can be simulated by performing sufficiently long simulations in order to correctly recover the average properties. However, small particle area fractions should be obtained by reducing the number of particles. Since reducing the radius of the particles leads to a too few number of collocation points on the particle boundaries (for $N_p = 225$ and $R_p = 0.02$ we have used $N_c = 12$ that is the lower limit for a good discretization of particle curvature). Therefore, the points for $\phi \cong 0.03, \phi \cong 0.054, \phi \cong 0.08$, are obtained by considering $N_p = 20, N_p = 40, N_p = 60$ respectively and $R_p = 0.03$ (open diamonds). Finally, the solid line is obtained by connecting the viscosities for $N_p = 150$ (full circles) and for the dilute system (open diamonds) with straight lines.

Our predictions show an increasing viscosity with increasing the particle area fraction. The trend is not linear but exponential, as found experimentally. The results for 225 particles match the 150 particles ones: 150 particles are sufficient to describe adequately the bulk properties of the suspension. Moreover, for dilute systems, the curve approaches the Einstein solution, as expected.

Finally, in the same figure, a comparison with the results of Hwang and Hulsen [29] is shown (open squares). As we can see, our predicted viscosity curve is slightly above

the Hwang and Hulsen one. However, it is important to point out that the viscosities reported by Hwang and Hulsen refer to the initial random distribution of the particles in the bi-periodic domain and they found an increasing transient behavior in time (which our simulations do not predict). Considering the uncertainty in the steady state value in their results we think the agreement is very good.

4.8 Conclusions

In this Chapter, we implemented a new simulation scheme for direct simulation of concentrated particle suspensions. Our simulation scheme is based on a three-layer domain that is able to: i) consider a small domain as a sample of the suspension, ii) impose the planar elongational flow boundary conditions sufficiently far from the particles and iii) calculate the steady state properties (in a statistical meaning) of the suspension. We don't need to deform the computational domain and no periodic boundary condition is imposed as in [29].

A steady state can be achieved by relocating the particles on the inflow sections when they cross the outflow sides of the domain.

We used a fictitious domain that is able to easily manage the rigid-body motion of the particles and to evaluate directly the hydrodynamic interactions, without approximations. So, we can obtain a combined weak formulation of the particle and fluid domain. This weak form has been discretized through a finite element method. The advantages of this procedure are: i) a time-independent mesh can be used, ii) the particle domain is discretized through the particle boundaries only (rigid-ring description) and iii) the rigid-body motion constraints are imposed by means the Lagrange multipliers (that are related to the traction force on the particle boundaries).

In order to demonstrate the feasibility of our method, we performed 2D simulations with an high number of the particles (150 and 225) in order to recover the bulk properties of a Newtonian suspension, by neglecting the fluid and particle inertia.

The local distribution of the flow and stress fields as well as the bulk properties are evaluated. These last ones are related to the bulk stress calculated through the Batchelor formula [9] where a particle and a fluid contribution are taken into account.

The results showed a very good agreement with dilute theory as well as other numerical simulations in the literature. In particular, for low particle area fractions, the relative bulk viscosity approaches the Einstein's analytical solution. By increasing the area fraction, the viscosity increases as well according to an exponential-like trend, as shown in the experiments. For concentrated systems, our results agree with the results of Hwang and Hulsen [29], obtained by using a different scheme. Finally, as in [29], we found an anisotropic structure where the particles are slightly farther apart along the horizontal direction than along the vertical direction. However, according to our calculations, the anisotropy is less pronounced than in [29]. Moreover, we don't observe any start-up phase.

Our scheme can be easily extended to 3D problems as well as to suspensions of viscoelastic fluids (see the next Chapter). In particular, to circumvent the memory limitations

due to the 3D simulations, iterative solvers and parallel calculations are required.

Chapter 5

Concentrated suspensions in planar elongational flow - Viscoelastic case

5.1 Introduction

In the previous Chapter, we presented a new numerical method in order to simulate concentrated suspensions under planar elongational flow. The analysis has been carried out for a Newtonian suspending fluid. In this Chapter, the method is extended to viscoelastic suspensions [71].

We analyze bulk rheological properties and the flow fields of a concentrated (two-dimensional) suspension of inertialess, non-Brownian particles inside a viscoelastic medium in a planar elongational flow. In such a fluid, the three-layer scheme previously presented is particularly well-suited. Indeed, the intermediate region serves to relax the viscoelastic stresses around the particles after the relocation, before they enter the inner region where the suspension properties are evaluated.

As already discussed, this approach possesses several useful features. First of all, a relatively small computational domain can be considered as the rheological and morphological responses can be obtained on a small region which represents (statistically) the entire suspension. The exit-relocation policy allows the use of time-independent fixed grid and avoids mesh deformation and remeshing, which strongly limits the achievement of a steady state [29]. With this approach, an average (statistically) steady state can be always achieved. Finally, no periodic boundary conditions are assumed, thus there is no need to split exiting-entering particles into parts [29].

The scheme is combined with a DEVSS-G/SUPG method [42, 56, 55, 72] that is one of the most robust mixed formulation currently available [73, 74]. Furthermore, we use the log-conformation representation of the constitutive equation [57, 58], which stabilizes computations at high Weissenberg number in an significant way. A Lagrange Multipliers/Fictitious Domain Method (LM/FDM) is implemented [30] in order to take into account the particle-fluid interactions that are treated implicitly via a combined weak formulation. Moreover, we use a rigid-ring description for the particle domain so only the

particle boundary needs to be discretized (we use collocation points) [28, 27, 29, 75]. Finally, the rigid-body motion constraints are imposed through Lagrange multipliers, that can be identified as traction forces on the particle surfaces.

We limit the simulations to two dimensions in order to show the feasibility of the new method based on a fixed grid. This is a first attempt and our objective is to try to find the typical experimental phenomena in such a system in a qualitative way. We can interpret our current 2D system as a viscoelastic fluid filled with cylindrical rods that are aligned normal to the flow direction. For comparison with real spherical particle suspensions, we need to extend the method to three dimensions. This will require iterative solvers and parallel calculations.

We focus on concentrated suspensions of rigid, non-Brownian disks in a planar elongational flow, where the particle and fluid inertia can be neglected. The viscoelastic medium is modeled as a Giesekus fluid taking into account shear thinning as well as elongational thickening phenomena. Simulations for a many-particle system are carried out. The local fields are calculated by solving the governing equations of the system. These distributions give useful information about the micro structure of the suspension and they show how the presence of the inclusions can affect the fluid domain with respect to the unfilled medium. Then, the macroscopic properties of the suspension as a whole (= bulk properties) are investigated. These properties are related to the bulk stress that is recovered by integrating the local stress field over the whole fluid domain. In this regard, we use the Batchelor bulk stress formula [9] where the bulk stress is given by a fluid as well as a particle contribution. Finally a comparison of our predictions with experimental data found in the literature is presented.

The Chapter is organized as follows: a description of the problem and the governing equations of the flow of circular disks in a viscoelastic matrix are presented in Section 5.2. In Section 5.3 the weak form of the equations is derived. Moreover, in the same Section, the spatial implementation and the time integration algorithm are also discussed. In Section 5.4, the bulk stress formula is given. Hence, in Section 5.5 the simulation scheme is presented. The particle area fraction and bulk stress formulas are also discussed. Finally, in Section 5.6, the results for the viscoelastic suspension are shown. Local fields are analyzed and discussed, by means of snapshots of the simulations. Then, the bulk properties are evaluated and the effect of the relaxation time (Weissenberg number) on the bulk viscosity is also studied. The local distribution of the Weissenberg number is exploited, in order to better understand the rheology of such suspensions. A comparison with experimental data is carried out, showing a good qualitative agreement.

5.2 Modeling

We consider suspensions consisting of a large number of rigid, non-Brownian, inertialess, circular disk particles (2D problem) inside a viscoelastic fluid under planar elongational flow. The fluid is modeled as a Giesekus fluid. The problem is schematized in Figure 5.1: particles (circles), denoted by $P_i(t)$ $(i = 1 \dots N)$, move in a square domain, Ω. Planar

elongational boundary conditions are imposed on the external boundaries, denoted by Γ_i ($i = 1 \ldots 4$). The Cartesian x and y coordinates are selected with the origin at the center of the domain. The particles move according to the imposed flow and hydrodynamic interactions: their rigid-body motion is completely defined by the translational velocity, denoted by $\boldsymbol{U}_i = (U_i, V_i)$ and angular velocity, $\boldsymbol{\omega}_i = \omega_i \boldsymbol{k}$, where $\boldsymbol{k}$ is the unit vector in the direction normal to the $x - y$ plane. For the 2D case, $\boldsymbol{U}_i$ and $\boldsymbol{\omega}_i$ have two and one components, respectively. So, each particle adds three unknowns to the global system. Moreover, the vector $\boldsymbol{X}_i = (X_i, Y_i)$ gives the position of the center of the particle P_i. In order to evaluate particle rotation, an angular information, $\boldsymbol{\Theta}_i = \Theta_i \boldsymbol{k}$, is associated with each disk (note that this latter quantity only serves for post-processing purposes).

5.2.1 Fluid domain

The governing equations for the fluid domain, neglecting inertia, can be stated as follows:

$$\nabla \cdot \boldsymbol{\sigma} = \boldsymbol{0} \quad \text{in } \Omega \backslash P(t) \tag{5.1}$$

$$\nabla \cdot \boldsymbol{u} = 0 \quad \text{in } \Omega \backslash P(t) \tag{5.2}$$

$$\boldsymbol{\sigma} = -p\boldsymbol{I} + 2\eta_s \boldsymbol{D} + \boldsymbol{\tau}_p \quad \text{in } \Omega \backslash P(t) \tag{5.3}$$

Equations (5.1)-(5.3) are the equations for the momentum balance and the continuity. In these equations $\boldsymbol{u}$, $\boldsymbol{\sigma}$, p, $\boldsymbol{I}$, $\boldsymbol{D}$, η_s, are the velocity, the stress, the pressure, the unity tensor, the rate-of-deformation tensor, the viscosity of Newtonian solvent, respectively.

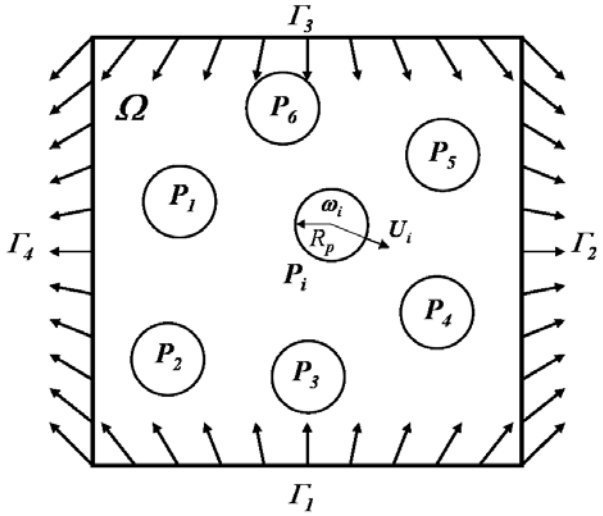

Figure 5.1: Schematic representation of the problem: a square fluid domain (Ω) filled with many particles ($P_i(t)$) is considered. Elongational flow conditions on the fluid boundaries (Γ_i) are imposed.

The polymer stress is given by:

$$\boldsymbol{\tau}_p = \frac{\eta_p}{\lambda}(\boldsymbol{c} - \boldsymbol{I}) \tag{5.4}$$

where $\boldsymbol{c}$ is the conformation tensor, η_p is the polymer viscosity and λ is the relaxation time.

We will model the viscoelastic fluid with the Giesekus constitutive equation:

$$\lambda \overset{\nabla}{\boldsymbol{c}} + \boldsymbol{c} - \boldsymbol{I} + \alpha(\boldsymbol{c} - \boldsymbol{I})^2 = \boldsymbol{0} \quad \text{in } \Omega \backslash P(t) \tag{5.5}$$

where α is the so-called mobility parameter. Moreover, the symbol $(\overset{\nabla}{})$ denotes the upper-convected time derivative defined as:

$$\overset{\nabla}{\boldsymbol{c}} \equiv \frac{\partial \boldsymbol{c}}{\partial t} + \boldsymbol{u} \cdot \nabla \boldsymbol{c} - (\nabla \boldsymbol{u})^T \cdot \boldsymbol{c} - \boldsymbol{c} \cdot \nabla \boldsymbol{u} \tag{5.6}$$

The zero shear viscosity is defined as $\eta_0 = \eta_s + \eta_p$.

The fluid boundary and initial conditions are given by:

$$\boldsymbol{u} = \boldsymbol{U}_i + \boldsymbol{\omega}_i \times (\boldsymbol{x} - \boldsymbol{X}_i) \quad \text{on } \partial P_i(t) \quad (i = 1 \dots N) \tag{5.7}$$

$$u = \dot{\epsilon} x, \quad v = -\dot{\epsilon} y \quad \text{on } \Gamma_i \quad (i = 1 \dots 4) \tag{5.8}$$

$$\boldsymbol{c}|_{t=0} = \boldsymbol{c}_0 \quad \text{in } \Omega \backslash P(t) \tag{5.9}$$

$$\boldsymbol{c} = \boldsymbol{c}_{\text{in}} \quad \text{on } \Gamma_1, \Gamma_3 \tag{5.10}$$

Equations (5.7)-(5.8) are the rigid-body motion on the particle boundaries and the planar elongation flow conditions on the external fluid boundaries, respectively. The initial conformation tensor condition is necessary (Eq. (5.9)) whereas no initial condition of the velocity and pressure fields is required, since inertia is neglected. In our simulations, we use a stress-free state, i.e. $\boldsymbol{c}|_{t=0} = \boldsymbol{I}$, as initial condition over the whole domain. Moreover, the conformation tensor condition on the inflow sections is required (Eq. (5.10)), since it is convected with the fluid. We impose on the inflow sections the conformation tensor for an unfilled Giesekus fluid, under the same flow and initial conditions of the suspension. As a consequence this condition is time-dependent, achieving a steady state after a certain time depending on the relaxation time.

5.2.2 Particle domain

Following [28, 27], a rigid-ring description for the particle domain is used in this work. A particle is considered as a rigid ring which is filled with the same fluid as in the fluid domain. This description can be used if inertia is neglected. Consequently, only the particle boundary needs to be discretized, thus leading to reduced memory requirements, and to a significant simplification of the implementation. Moreover, as shown later, the traction force on the particle boundaries can be obtained as a part of the solution, when the rigid-body constraints are implemented through Lagrange multipliers.

With the rigid-ring description, the set of equations for a particle P_i in a Giesekus fluid can be written as:

$$\nabla \cdot \hat{\boldsymbol{\sigma}} = \mathbf{0} \ \text{ in } P_i(t) \tag{5.11}$$

$$\nabla \cdot \boldsymbol{u} = 0 \ \text{ in } P_i(t) \tag{5.12}$$

$$\hat{\boldsymbol{\sigma}} = -p\boldsymbol{I} + 2\eta_s \boldsymbol{D} + \boldsymbol{\tau}_p \ \text{ in } P_i(t) \tag{5.13}$$

$$\boldsymbol{\tau}_p = \frac{\eta_p}{\lambda}(\boldsymbol{c} - \boldsymbol{I}) \tag{5.14}$$

$$\lambda \overset{\nabla}{\boldsymbol{c}} + \boldsymbol{c} - \boldsymbol{I} + \alpha(\boldsymbol{c} - \boldsymbol{I})^2 = \mathbf{0} \ \text{ in } P_i(t) \tag{5.15}$$

$$\boldsymbol{u} = \boldsymbol{U}_i + \boldsymbol{\omega}_i \times (\boldsymbol{x} - \boldsymbol{X}_i) \ \text{ on } \partial P_i(t) \tag{5.16}$$

Again, Eqs. (5.11)-(5.16) are equations for the momentum balance, the continuity, the constitutive relation (Giesekus) and the boundary conditions respectively, which are the same for the fluid domain. As we did in Chapter IV (and in [75]), we denote the fluid stress tensor inside the particle ($\hat{\boldsymbol{\sigma}}$) different from the stress tensor in the fluid between particles in order to make a distinction between the stress tensor inside the 'real' particle ($\boldsymbol{\sigma}$) and the fictitious fluid stress. The initial condition for the polymer stress is again the stress-free state, as it should be inside the rigid-ring:

$$\boldsymbol{c}|_{t=0} = \boldsymbol{c}_0 = \boldsymbol{I} \ \text{ in } P_i(t) \tag{5.17}$$

However, for the particle domain, we do not need any inflow condition for the conformation tensor, since there is no net convection of material across the particle boundaries.

The solution of the rigid-ring problem, Eqs. (5.11)-(5.17), is the rigid-ring motion imposed on the particle boundary [28, 27]:

$$\boldsymbol{u} = \boldsymbol{U}_i + \boldsymbol{\omega}_i \times (\boldsymbol{x} - \boldsymbol{X}_i) \ \text{ in } P_i(t) \tag{5.18}$$

Due to the rigid-body motion, the polymer stress inside the ring remains zero. However, as discussed later, after the particle relocation, the stress inside the ring will be the one corresponding to the region occupied by the relocated particle (of course different from zero). In order to preserve the particle as a rigid-ring, we set to zero the polymer stress (i.e. $\boldsymbol{c}|_{t=0} = \boldsymbol{I}$) inside the ring after the relocation. As remarked in Chapter IV (and in [75]), with the rigid-ring description, the pressure level inside a particle is undetermined/not unique, in theory. However it turns out that, in the numerical implementation with the fictitious domain method, it is not necessary to specify the pressure level inside the particle directly [28].

Finally, the particle positions and rotations are updated by integrating the following kinematic equations:

$$\frac{d\boldsymbol{X}_i}{dt} = \boldsymbol{U}_i, \quad \boldsymbol{X}_i|_{t=0} = \boldsymbol{X}_{i,0} \tag{5.19}$$

$$\frac{d\boldsymbol{\Theta}_i}{dt} = \boldsymbol{\omega}_i, \quad \boldsymbol{\Theta}_i|_{t=0} = \boldsymbol{\Theta}_{i,0} \tag{5.20}$$

Equation (5.20) is completely decoupled from the other equations for circular particles.

5.2.3 Hydrodynamic interactions

In the coupling of the fluid and particle domain we require the velocity to be continuous. The equations governing the velocity on the fluid-particle interface (Eqs. (5.7) and (5.16)) restrict the motion on particle-fluid interface to (for the 2D case) three unknowns for each particle, namely the translational ($\boldsymbol{U}_i$) and angular velocities ($\boldsymbol{\omega}_i$) of the particle. Therefore, requiring $\boldsymbol{U}_i$ and $\boldsymbol{\omega}_i$ to be the same for the fluid and particle domain is sufficient for the velocity to be continuous.

An additional requirement in the particle-fluid coupling is that the force acting on the fluid is minus the force acting on the particle (sum is zero). The same is true for the torque. Under the assumptions of absence of inertia and external forces and torques, the particles are in fact force-free and torque-free:

$$\boldsymbol{F}_i = \int_{\partial P_i(t)} \boldsymbol{\sigma} \cdot \boldsymbol{n} ds = \boldsymbol{0} \tag{5.21}$$

$$\boldsymbol{T}_i = \int_{\partial P_i(t)} (\boldsymbol{x} - \boldsymbol{X}_i) \times (\boldsymbol{\sigma} \cdot \boldsymbol{n}) ds = \boldsymbol{0} \tag{5.22}$$

where $\boldsymbol{F}_i = (F_{i,x}, F_{i,y})$ and $\boldsymbol{T}_i = T_i \boldsymbol{k}$ are the total force and torque on the particle boundaries, $\boldsymbol{n}$ is the outwardly directed unit normal vector on ∂P_i. Note, that (5.21) and (5.22) do not need to be imposed: they are a property of the system studied. We only require a balance of forces and torques on the particle/fluid interfaces.

Finally, the system of equations (5.1)-(5.5) for the fluid domain with initial and boundary conditions (5.7)-(5.10), the corresponding equations for particle domain (5.11)-(5.15) with initial and boundary condition (5.16)-(5.17) and the hydrodynamic equations (5.21)-(5.22) form a well-posed problem in the unknowns: p, $\boldsymbol{u}$, $\boldsymbol{\sigma}$, $\boldsymbol{c}$, $\boldsymbol{U}_i$, $\boldsymbol{\omega}_i$. The kinematic equations (5.19)-(5.20) are integrated to update the particle positions and rotations. So, every time-step the problem is solved and the flow fields, rigid-body unknowns and stresses are evaluated. However, we need to find an expression for the evaluation of bulk rheological properties (bulk stress, bulk viscosity, etc.). This will be presented in Section 5.4.

5.3 Weak form and implementation

5.3.1 Weak form

In this Section, the weak form for the whole domain is presented. We follow the combined weak formulation procedure of Glowinski et al. [30], consisting of the following steps:

1. The coupling of the fluid and particle domains into a single weak form. The variational spaces in this weak form still fulfill the rigid body constraint. The balance of forces and torques at fluid-particle boundaries is satisfied, but the forces and torques do not explicitly end up in the variational form.

2. The "release" of the constraint on the variational space by introducing Lagrange multipliers. Here the variational space is extended with all velocity degrees of freedom. The unknowns ω_i and $\boldsymbol{U}_i$ are still there and are part of the separate constraint equation.

We implement the DEVSS method [42] that is one of the most robust formulations currently available. The constitutive equation (5.5) is discretized using the SUPG method [56]. Moreover, in the constitutive equation, the velocity gradient used is the projected one ($\boldsymbol{G}$) that is the projection of $(\nabla \boldsymbol{u})^T$ (DEVSS-G formulation) [55]. With this formulation, the instabilities that can arise for time-dependent shear flows are suppressed [72, 73, 74]. Finally, a log-conformation representation for the conformation tensor has been used [57, 58]. The original equation for the conformation tensor $\boldsymbol{c}$ is transformed to an equivalent equation for $\boldsymbol{s} = \log(\boldsymbol{c})$:

$$\dot{\boldsymbol{s}} = \frac{\partial \boldsymbol{s}}{\partial t} + \boldsymbol{u} \cdot \nabla \boldsymbol{s} = \boldsymbol{g}(\boldsymbol{\nabla u^T}, \boldsymbol{s}) \tag{5.23}$$

An expression for the function $\boldsymbol{g}$ can be found in [58]. Solving the equation for $\boldsymbol{s}$ instead of the equation for $\boldsymbol{c}$ leads to a substantial improvement of stability for high Weissenberg number (defined as $\mathrm{Wi} = \dot{\epsilon}\lambda$).

With these assumptions, the weak form for the whole domain can be stated as follows: For $t > 0$, find $\boldsymbol{u} \in U, p \in P, \boldsymbol{s} \in S, \boldsymbol{G} \in G, \boldsymbol{U}_i \in \Re^2, \boldsymbol{\omega}_i \in \Re, \boldsymbol{\lambda}_i \in L^2(\partial P_i(t)),\ (i = 1 \ldots N)$ such that:

$$\begin{aligned}
&\int_\Omega 2\eta_s \boldsymbol{D}(\boldsymbol{v}) : \boldsymbol{D}(\boldsymbol{u})\, dA - \int_\Omega \nabla \boldsymbol{v}\, p\, dA + \int_\Omega a(\nabla \boldsymbol{v})^T : \nabla \boldsymbol{u}\, dA \\
&- \int_\Omega a(\nabla \boldsymbol{v})^T : \boldsymbol{G}^T\, dA + \sum_{i=1}^{N} \langle \boldsymbol{v} - (\boldsymbol{V}_i + \boldsymbol{\chi}_i \times (\boldsymbol{x} - \boldsymbol{X}_i)), \boldsymbol{\lambda}_i \rangle_{\partial P_i} \\
&\qquad = -\int_\Omega \boldsymbol{D}(\boldsymbol{v}) : \boldsymbol{\tau}_p\, dA,
\end{aligned} \tag{5.24}$$

$$\int_\Omega q \nabla \cdot \boldsymbol{u}\, dA = 0, \tag{5.25}$$

$$\int_\Omega \boldsymbol{H} : \boldsymbol{G}\, dA - \int_\Omega \boldsymbol{H} : (\nabla \boldsymbol{u})^T\, dA = \boldsymbol{0}, \tag{5.26}$$

$$\int_\Omega (\boldsymbol{S} + \tau \boldsymbol{u} \cdot \nabla \boldsymbol{S}) : \left(\frac{\partial \boldsymbol{s}}{\partial t} + \boldsymbol{u} \cdot \nabla \boldsymbol{s} - \boldsymbol{g}(\boldsymbol{G}, \boldsymbol{s}) \right) dA = \boldsymbol{0}, \tag{5.27}$$

$$\langle \boldsymbol{\mu}_i, \boldsymbol{u} - (\boldsymbol{U}_i + \boldsymbol{\omega}_i \times (\boldsymbol{x} - \boldsymbol{X}_i)) \rangle_{\partial P_i} = \boldsymbol{0}, \quad (i = 1...N), \tag{5.28}$$

$$\boldsymbol{s} = \boldsymbol{s}_0 \quad \text{at } t = 0, \quad \text{in } \Omega, \tag{5.29}$$

$$\boldsymbol{s} = \boldsymbol{s}|_{\phi=0} \quad \text{on } \Gamma_1, \Gamma_3 \tag{5.30}$$

for all $\boldsymbol{v} \in U$, $q \in P$, $\boldsymbol{S} \in S$, $\boldsymbol{H} \in G$, $\boldsymbol{V}_i \in \Re^2$, $\boldsymbol{\chi}_i \in \Re$ and $\boldsymbol{\mu}_i \in L^2(\partial P_i(t))$, where U, P, S, G are suitable functional spaces. The τ parameter in Eq. (5.27) is given by $\tau = \beta h / 2V$, where

β is a dimensionless constant, h is a typical size of the element and V is a characteristic velocity for the element. In our simulations, we have chosen $\beta = 1$ and for V we take the velocity in the center of the element. Moreover, a in the Eq. (5.24) is chosen equal to the polymer viscosity, $a = \eta_p$. We take the initial value of $\boldsymbol{s}_0 = \mathbf{0}$, corresponding to zero initial stress. Finally, $\boldsymbol{s}|_{\phi=0}$ is the conformation tensor for a unfilled fluid in the same conditions as the suspension and generally is a function of time.

In our rigid ring formulation the Lagrange multiplier $\boldsymbol{\lambda_i}$ can be interpreted as the "traction jump" over the rigid ring (see [28, 27]). Note, the variation of $\boldsymbol{U}_i$ and $\boldsymbol{\omega}_i$ (i.e. $\boldsymbol{V}_i$ and $\boldsymbol{\chi}_i$) in Eq. (5.24) leads to the equations:

$$\langle \boldsymbol{\lambda_i} \rangle = \mathbf{0} \tag{5.31}$$

$$\langle (x - \boldsymbol{X}_i) \times \boldsymbol{\lambda_i} \rangle = \mathbf{0} \tag{5.32}$$

for all particles, which can be interpreted as: the total force jump and torque jump is zero, i.e. forces and torques are correctly balanced on the particle surface.

5.3.2 Implementation

For the discretization of the weak form, we use regular quadrilateral elements with continuous bi-quadratic interpolation (Q_2) for the velocity $\boldsymbol{u}$, bilinear continuous interpolation (Q_1) for the pressure p, bilinear continuous interpolation (Q_1) for velocity gradient $\boldsymbol{G}$ and bilinear continuous interpolation (Q_1) for the log-conformation tensor $\boldsymbol{s}$. We discretize the boundaries of the particles through collocation points. Then, Eq. (5.28) is approximated as:

$$\langle \boldsymbol{\mu}_i, \boldsymbol{u} - (\boldsymbol{U}_i + \boldsymbol{\omega}_i \times (\boldsymbol{x} - \boldsymbol{X}_i)) \rangle_{\partial P_i} \approx \sum_{k=1}^{N_c} \boldsymbol{\mu}_{i,k} \cdot \{ \boldsymbol{u}(\boldsymbol{x}_k) - (\boldsymbol{U}_i + \boldsymbol{\omega}_i \times (\boldsymbol{x}_k - \boldsymbol{X}_i)) \tag{5.33}$$

The time integration is more cumbersome. Initially, the viscoelastic polymer stress is set to zero in the whole domain. Since we neglect inertia, the initial condition for the velocity is not necessary. So, we can solve the equations (5.24)-(5.26) and the constraint equation (5.28) in order to get the distribution of the fluid velocity and the rigid-body motion of the particles, at the initial time step. Then, at every time step, we follow the following procedure:

Step 1. The particle positions and rotations are updated. The new configuration is obtained by integrating the kinematic equation (5.19). The explicit second-order Adams-Bashforth method is used:

$$\boldsymbol{X}_i^{n+1} = \boldsymbol{X}_i^n + \Delta t \left(\frac{3}{2} \boldsymbol{U}_i^n - \frac{1}{2} \boldsymbol{U}_i^{n-1} \right) \tag{5.34}$$

The first time step of the simulation is performed with an explicit Euler method:

$$\boldsymbol{X}_i^{n+1} = \boldsymbol{X}_i^n + \Delta t \boldsymbol{U}_i^n \tag{5.35}$$

Step 2. The log-conformation tensor at the next time step, $\boldsymbol{s}^{n+1}$, is evaluated by integrating the constitutive equation (5.27). A semi-implicit first-order Euler scheme is used and (5.27) is replaced by the following time-discretized form:

$$\int_\Omega (\boldsymbol{S} + \tau \boldsymbol{u^n} \cdot \nabla \boldsymbol{S}) : \left(\frac{\boldsymbol{s}^{n+1} - \boldsymbol{s}^n}{\Delta t} + \boldsymbol{u}^n \cdot \nabla \boldsymbol{s}^{n+1} - \boldsymbol{g}(\boldsymbol{G}^n, \boldsymbol{s}^n) \right) dA = \boldsymbol{0}, \tag{5.36}$$

Step 3. Finally, the remaining unknowns $(\boldsymbol{u}, p, \boldsymbol{G}, \boldsymbol{U}_i, \boldsymbol{\omega}_i)^{n+1}$ as well as the Lagrange multipliers $(\boldsymbol{\lambda}_i)$ can be found by solving the Eqs. (5.24)-(5.26) and (5.28) using the particle configuration and the polymer stress evaluated in the previous two steps:

$$\begin{aligned} &\int_\Omega 2\eta_s \boldsymbol{D}(\boldsymbol{v}) : \boldsymbol{D}(\boldsymbol{u}^{n+1})\, dA - \int_\Omega \nabla \cdot \boldsymbol{v}\, p^{n+1}\, dA + \int_\Omega a(\nabla \boldsymbol{v})^T : \nabla \boldsymbol{u}^{n+1}\, dA \\ &- \int_\Omega a(\nabla \boldsymbol{v})^T : (\boldsymbol{G}^{n+1})^T\, dA + \sum_{i=1}^{N} \langle \boldsymbol{v} - (\boldsymbol{V}_i + \boldsymbol{\chi}_i \times (\boldsymbol{x} - \boldsymbol{X}_i^{n+1}), \boldsymbol{\lambda}_i^{n+1} \rangle_{\partial P_i} \\ &\qquad = - \int_\Omega \boldsymbol{D}(\boldsymbol{v}) : \boldsymbol{\tau}_p^{n+1}\, dA, \end{aligned} \tag{5.37}$$

$$\int_\Omega q \nabla \cdot \boldsymbol{u}^{n+1}\, dA = 0, \tag{5.38}$$

$$\int_\Omega \boldsymbol{H} : \boldsymbol{G}^{n+1}\, dA - \int_\Omega \boldsymbol{H} : (\nabla \boldsymbol{u}^{n+1})^T\, dA = \boldsymbol{0}, \tag{5.39}$$

$$\langle \boldsymbol{\mu}_i, \boldsymbol{u}^{n+1} - (\boldsymbol{U}_i^{n+1} + \boldsymbol{\omega}_i^{n+1} \times (\boldsymbol{x} - \boldsymbol{X}_i^{n+1})) \rangle_{\partial P_i} = 0, \quad (i = 1...N) \tag{5.40}$$

In Step 3, a sparse linear symmetric system needs to be solved. We use a direct method based on a sparse multi-frontal variant of Gaussian elimination (HSL/MA57) [69]. This solver is suited for a symmetric matrix because it stores only one half of the full matrix, saving memory and CPU time. However, since Eq. (5.36) leads to an unsymmetric system, an unsymmetric sparse direct solver (HSL/MA41) is used [69].

5.4 Bulk stress

By solving the set of equations just presented, one gets the field values in every point of the domain. However we are also interested in the properties of the material as a whole (= bulk properties). We use the bulk stress formulation by Batchelor [9] taking into account a fluid as well a particle contribution, as follows (for the 2D case):

$$\langle \boldsymbol{\sigma} \rangle = \frac{1}{A} \int_A \boldsymbol{\sigma}\, dA = \frac{1}{A} \int_{A_f} \boldsymbol{\sigma}\, dA + \frac{1}{A} \int_{\partial A_p} \boldsymbol{\sigma} \cdot \boldsymbol{n} \boldsymbol{x}\, ds \tag{5.41}$$

where $\langle \cdot \rangle$ is an area average quantity in an area A, A_f is the area occupied by the fluid and ∂A_p is the total particle surface. For a viscoelastic constitutive equation (Eq. (5.3)),

the bulk stress can be written as:

$$\langle \boldsymbol{\sigma} \rangle = -\langle p \rangle_f \boldsymbol{I} + 2\eta_s \langle \boldsymbol{D} \rangle_f + \langle \boldsymbol{\tau}_p \rangle_f + \frac{1}{A} \int_{\partial A_p} \boldsymbol{t}\boldsymbol{x}\, ds \tag{5.42}$$

In this equation $\boldsymbol{t}$ is the traction force on the particle surface and $\langle \cdot \rangle_f = 1/A \int_{A_f} \cdot \; dA$ is a weighted area average quantity in A_f. Note, that, $\langle \boldsymbol{D} \rangle_f = \langle \boldsymbol{D} \rangle$ because the rate-of-deformation tensor is zero inside the particle domain, but we prefer to retain $\langle \boldsymbol{D} \rangle_f$ for clarity. In Eq. (5.42) the first three terms of the right-hand side represent the fluid contribution and the integral term is the contribution of all particles.

As discussed in our previous Chapter (see also [75]), this equation is not useful for the evaluation of the bulk stress in our numerical scheme. Indeed, the pressure and the polymer stress on the particle boundaries are required. Since these fields are discontinuous across the particle boundaries, a large error affects the solution close to the particles. The relationship between the Lagrange multipliers and traction forces acting on the particle surface can be used instead. In fact, this relationship is still valid in the viscoelastic case, since the traction force now includes the contribution of the polymer stress:

$$\int_{\partial A_p} \boldsymbol{t}\boldsymbol{x}\, ds = \langle \boldsymbol{\lambda}, \boldsymbol{x} \rangle + \int_{A_p} \hat{\boldsymbol{\sigma}}\, dA \tag{5.43}$$

where:

$$\int_{A_p} \hat{\boldsymbol{\sigma}}\, dA = -\int_{A_p} p\, dA\; \boldsymbol{I} + \int_{A_p} 2\eta_s \boldsymbol{D}\, dA + \int_{A_p} \boldsymbol{\tau}_p\, dA \tag{5.44}$$

In theory, the fluid inside the rigid ring moves like a rigid body so $\boldsymbol{D} = \boldsymbol{0}$ and $\boldsymbol{\tau}_p = \boldsymbol{0}$ inside the rigid ring. In the numerical implementation this is only approximately true. However, as in Chapter IV (and in [75]), we found both contributions can still be neglected and only the pressure has to be calculated by performing an integration on the particle domain.

Eqs. (5.42) and (5.43) can be combined and the bulk stress is calculated as follows:

$$\langle \boldsymbol{\sigma} \rangle = \langle \hat{\boldsymbol{\sigma}} \rangle + \frac{1}{A} \langle \boldsymbol{\lambda}, \boldsymbol{x} \rangle \tag{5.45}$$

where $\langle \hat{\boldsymbol{\sigma}} \rangle$ is the average over the full domain (fluid + particle) of the fluid stress tensor. Note that this equation is the same for the Newtonian case. Of course, now $\langle \hat{\boldsymbol{\sigma}} \rangle$ includes the polymer stress also.

The fluid contribution to the bulk stress can be recovered as follows:

$$\langle \boldsymbol{\sigma} \rangle_f = \langle \hat{\boldsymbol{\sigma}} \rangle - \frac{1}{A} \int_{A_p} \boldsymbol{\sigma}\, dA \tag{5.46}$$

whereas the particle contribution in Eq. (5.42) can be computed using Eq. (5.43). It should be noticed that if one is interested in the bulk stress $\langle \boldsymbol{\sigma} \rangle$ only, it is not necessary to evaluate the integral of fluid stress inside the particles. Instead, if one needs the fluid and particle contribution separately, the integral of fluid stress tensor inside the objects is required.

Finally, it is important to point out that Eq. (5.45) is valid only if the particles are completely immersed in the computational domain, where bulk properties are evaluated. In our simulation scheme, the particles cross the boundaries of the domain where the bulk properties are computed [75]. Therefore, a slight change in the area A will be required, as shown in Sec. 5.5.

5.5 Simulation scheme

In this Section, the basics of our simulation procedure and the computational domain used in the simulations are briefly presented. For details, refer to the previous Chapter and [75]. The idea of the scheme is depicted in Figure 5.2. In this picture, four time sequence frames of the procedure are shown (for simplicity we consider three particles only). Initially (first frame, $t = 0$), the particles are positioned randomly inside the fluid. Each time step we solve the governing equations and we get the local fields. Finally the particle positions can be updated. The particles will move according to the streamlines and the hydrodynamic interactions as well (second frame). In the next time step, the particles will change configuration again (third frame). Note that the particle number "2" is very close to the right boundary of the domain, so, in the next time step, it would go out. The basic idea is to randomly relocate the particle "2" on one of the two inflow sections of the domain (fourth frame). The inflow section is randomly chosen as well as the position of the particle on this section. Note that when a particle is relocated, its position in the next time step cannot be updated using the Adams-Bashforth algorithm (Eq. (5.34)), since the velocity in the previous time step (before the relocation) is required. So, only for this step, the Euler method (Eq. (5.35)) is used.

The implementation of the scheme needs to satisfy two conditions: i) the particles should not feel the presence of the boundary conditions imposed on the external bound-

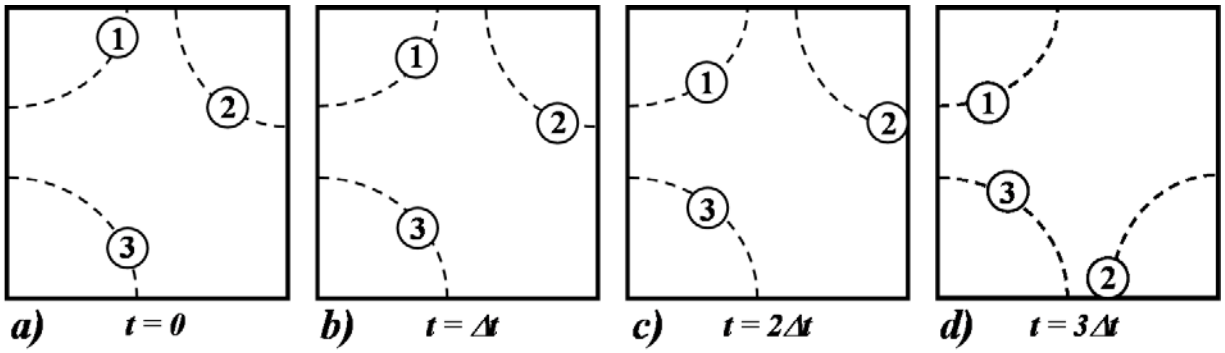

Figure 5.2: Scheme of the simulation procedure: (a) initially, the particles are randomly distributed in the fluid; (b) the particles move according to the streamlines and hydrodynamic interactions; (c) the particle "2" is close to the boundary; (d) the particle "2" is randomly relocated on one of the two inflow sections.

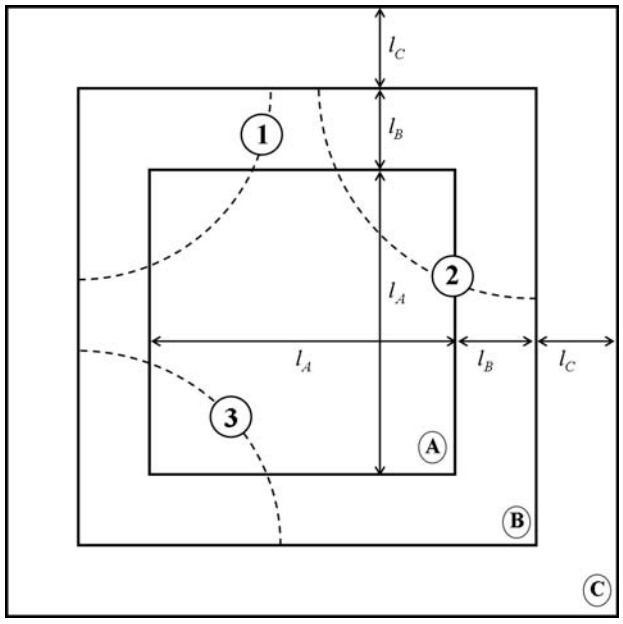

Figure 5.3: Schematic representation of the computational domain. The particles can move in the A- and B-regions. In the A-region the bulk calculations are performed. When a particle crosses the outflow sections of the B-region, it is relocated on the inflow sections of the same region. The elongational flow conditions are imposed on external boundaries of the C-region.

aries of the computational domain, ii) after the relocation, the polymer stress surrounding the particles needs to relax before it is taken into account in order to recover the bulk properties. Therefore, the computational domain is divided in three concentric square regions as depicted in Figure 5.3.

In the A-region the particles can move and only in this region the bulk properties are evaluated. So, this region can be considered as the representative frame for the whole suspension.

In the B-region the particles can move as well and, when they cross the outflow boundaries of it, they are relocated randomly on one of the two inflow sections of the same region. Therefore, the particles in this region affect the particles in the sample A-region, as should be because the sample region should be surrounded by the remainder part of the suspension. This region is mandatory because the stress surrounding the particles, after the relocation, needs time to develop before the particles enter in the A-region in order to achieve a "developed" state (in a statistical meaning). Moreover, after the relocation, the polymer stress inside the particle will not be zero but the one corresponding to the region occupied by the relocated particle before the relocation. Then, in order to preserve the particle as a rigid-ring, we impose zero stress ($\boldsymbol{c} = \boldsymbol{I}$ or $\boldsymbol{s} = \log(\boldsymbol{c}) = \boldsymbol{0}$) inside the relocated particle.

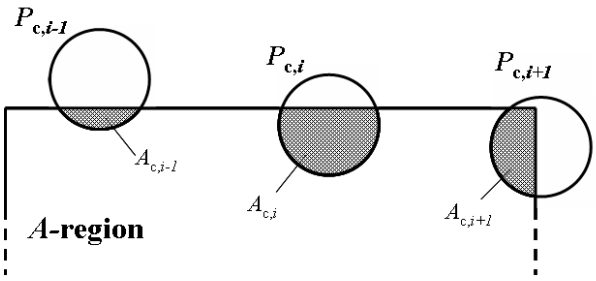

Figure 5.4: Relative positions of the particles crossing the boundaries of the A-region. The summation of marked regions gives the particle area inside the square of these particles.

Finally, on the external boundaries of the C-region we impose the elongational flow boundary conditions (Eqs. (5.8)) and no particle will enter there. This region imposes the boundary conditions sufficiently far from the particles to avoid wall effects. Of course, this region should be sufficiently large compared to the particle radius.

Bulk stress calculations are performed in the A-region only. Therefore, particles can be found on the boundaries dividing region A from B (See particle "2" in Figure 5.3). As a result, the particle area fraction and bulk stress evaluations in the internal region are not trivial [75]. For each particle configuration (= each time step), the particle area fraction is calculated as follows:

$$\phi = \frac{\sum_{i=1}^{N_{\text{int}}} \pi R_{\text{p},i}^2 + \sum_{i=1}^{N_{\text{cross}}} A_{\text{c},i}}{A_{A\text{-region}}} \tag{5.47}$$

The first summation refers to the particles that are completely inside the A-region and N_{int} is the number of these particles. The second summation takes into account the areas inside the A-region of the particles crossing this region (marked areas in Figure 5.4). Therefore, in Eq. (5.47), N_{cross} is the number of the particles crossing the boundaries and $A_{\text{c},i}$ is the area inside the A-square of these particles. Finally $A_{A\text{-region}}$ is the area of the A-region. The marked areas in Figure 5.4 are evaluated by implementing geometric rules ($P_{\text{c},i-1}$ and $P_{\text{c},i}$ particles in the figure) or through a Monte-Carlo integration if the particle crosses the corner of the A-region ($P_{\text{c},i+1}$ particle in the figure).

Let us now consider the bulk stress expression Eq. (5.43). As stated above, this formula is valid only if the particles are completely immersed in the domain. However, we need to evaluate the bulk stress in the internal region only, where the particles can cross the corresponding boundaries. We should evaluate the particle stress integral on the part of the object that is inside this region. Since the 'real' stress inside a particle is unknown and it is not possible to compute the stress contribution of such a particle we need to modify the domain [75]. The new A-region should fully include all the particles and the 'average' domain (in time and space) should still approximate the A-region.

The new computational domain is depicted in Figure 5.5 and it is enclosed by the bold line: it is given by the A-region plus the external part of the particles crossing the

square boundaries and with the center inside the square (diagonal marked areas) minus the internal part of the particles crossing the square boundaries and with the center outside the square (square marked areas). So, a particle gives a contribution to the bulk stress only if it is completely inside the A-region or if it crosses the boundary of the A-region and has the center inside it. In this way, on average in time, the right contribution to the bulk stress of the particles crossing the A-region can be recovered.

So, the bulk stress formula Eq. (5.45) to the new extended domain is written as follows:

$$\langle \boldsymbol{\sigma} \rangle = \frac{\displaystyle\int_{A\text{-region}} \hat{\boldsymbol{\sigma}}\, dA - \int_{\sum A_{\text{c-int}}} p\, dA\, \boldsymbol{I} + \int_{\sum A_{\text{c-ext}}} p\, dA\, \boldsymbol{I} + \sum_{i=1}^{N_{\text{int}}+N_{\text{c-int}}} \langle \boldsymbol{\lambda}, \boldsymbol{x} \rangle_i}{A_{A\text{-region}} + \displaystyle\sum_{i=1}^{N_{\text{c-int}}} A_{\text{c-int},i} - \sum_{i=1}^{N_{\text{c-ext}}} A_{\text{c-ext},i}} \tag{5.48}$$

where $N_{\text{c-int}}$ and $N_{\text{c-ext}}$ are the number of particles crossing the boundaries with the center inside and outside the A-region, respectively; $A_{\text{c-int}}$ and $A_{\text{c-ext}}$ are the areas shown in Figure 5.5. Note that: i) the area of the extended domain is given by the denominator of the formula, ii) $\langle \hat{\boldsymbol{\sigma}} \rangle$ is split into $\langle \hat{\boldsymbol{\sigma}} \rangle_{A\text{-region}} + \langle \hat{\boldsymbol{\sigma}} \rangle_{A_{\text{c-int}}} - \langle \hat{\boldsymbol{\sigma}} \rangle_{A_{\text{c-ext}}}$, iii) the last two terms are approximated by using the pressure term only, similar to procedure for approximating Eq. (5.44). This formula is exactly the same as the Newtonian case (Eq. (4.28)) including, now, the polymer stress in $\hat{\boldsymbol{\sigma}}$.

To apply this formula, one needs to evaluate the integral of the pressure on $A_{\text{c-int}}$ and $A_{\text{c-ext}}$. This integral is calculated again by performing a Monte-Carlo integration. For many particles, this method could be expensive in computational time. However, 10000 random points are sufficient for a good accuracy.

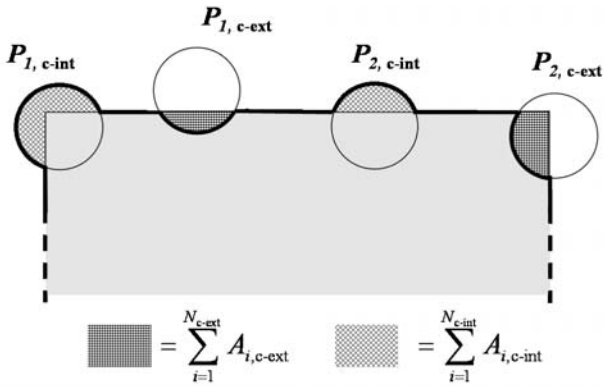

Figure 5.5: Relative positions of particles crossing the boundaries of the A-region. The bulk stress is evaluated in a modified domain, included inside the bold line: the square region plus the external part of the particles crossing the square boundaries and with the center inside the square (diagonal marked areas) minus the internal part of the particles crossing the square boundaries and with the center outside the square (square marked areas).

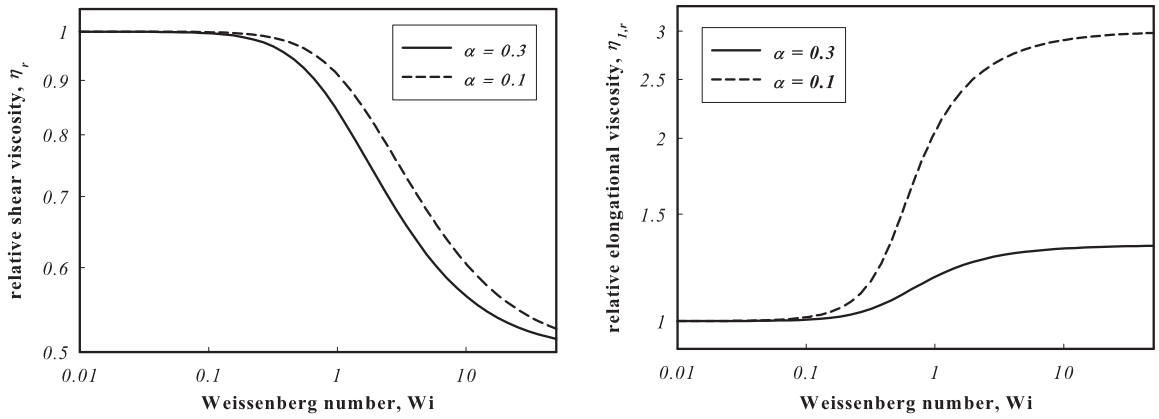

Figure 5.6: Shear (a) and elongational (b) relative viscosities for an unfilled Giesekus fluid. The shear thinning and strain hardening phenomena are predicted.

5.6 Results

In this Section, we present the results for a concentrated viscoelastic suspension in a planar elongational flow.

There are three parameters in the Giesekus model: the ratio of the solvent viscosity to the polymer viscosity, η_s/η_p, the constitutive parameter, α, and the Weissenberg number. In our simulations, we set $\eta_s = \eta_p = 1.0$ ($\eta_s/\eta_p = 1$) and $\dot{\epsilon} = 0.5$ (Wi $= 0.5\lambda$).

In Figure 5.6, the relative viscosities in shear (η_r) and elongational ($\eta_{1,r}$) flow for a unfilled Giesekus fluid as functions of Weissenberg number are shown. These viscosities are given by:

$$\eta_r = \frac{\sigma_{xy}}{\dot{\gamma}} \cdot \frac{1}{\eta_s + \eta_p} \tag{5.49}$$

$$\eta_{1,r} = \frac{(\sigma_{xx} - \sigma_{yy})}{\dot{\epsilon}} \cdot \frac{1}{4(\eta_s + \eta_p)} \tag{5.50}$$

where σ_{xx}, σ_{xy}, σ_{yy} are the xx-, xy-, yy-component of the stress tensor and $\dot{\gamma}$ and $\dot{\epsilon}$ are the shear and elongational rate. The factor "4" in Eq. (5.50) is due to the bi-dimensional Trouton ratio.

As we can see, the Giesekus model can predict shear thinning and strain hardening phenomena. The effect of the parameter α on both viscosities is shown. Realistic values of α are given by $0.05 < \alpha < 0.5$ [76]. In our simulations, $\alpha = 0.1$ is chosen.

The average relative bulk viscosities of the suspension is defined by using the effective elongational rate [75]:

$$\overline{\eta}_{1,r} = \left\langle \frac{\sigma_{xx} - \sigma_{yy}}{\dot{\epsilon}_{\text{eff}}} \right\rangle \cdot \frac{1}{4(\eta_s + \eta_p)} \tag{5.51}$$

Table 5.1: Mesh parameters for A- and C-region.

Symbol	Description	Value
l_A	Length of the A-region	1.0
n_A	Number of elements in the A-region in one coordinate direction	100
l_C	Length of the C-region	0.25
n_C	Number of elements in the C-region in one coordinate direction	see Table 2

In Eq. (5.51), $\dot{\epsilon}_{\text{eff}}$ is an effective elongational rate evaluated by performing the integral of $\boldsymbol{D}$ over the A-region for every particle configuration. As for the Newtonian case [75], we can evaluate a time-average relative bulk viscosity by averaging over a sufficiently high number of time steps (= many configurations). Of course, we will not take into the account the initial transient phase. Also in this case, 2000 time steps are enough (the bulk properties do not change if an higher number of time steps are considered).

Finally, we note that occasionally there is a slight overlap of a small number of particles. As reported in Chapter III (and [75]) this overlapping can be reduced by using an artificial repulsion force. However, the bulk stress is hardly affected and the differences are within the statistical fluctuations. Therefore, we decided not to use artificial repulsive forces in this work.

5.6.1 Code validation/verification

A validation of the code is carried out through a comparison with a boundary fitted method ($PolyFlow^{©}$). The simple test problem of a single particle at the center of a square domain is chosen. The results (not presented here) show the same features of the Newtonian case [75]: i) the discontinuity of pressure and polymer stress cannot accurately be predicted by the fictitious domain method and ii) the number of collocation points is a crucial choice in order to assure an accurate solution (especially regarding the bulk properties). A preliminary analysis has shown that the right number of collocation points is the same as the Newtonian case.

The mesh used is slightly different from the one used in Chapter III. Regular square elements are again chosen to discretize the A-region and coarser trapezoidal elements are chosen for the C-region (the mesh parameters are reported in Table 5.1 with the meaning of the symbols in the Figure 5.3). However, in this work, trapezoidal elements are chosen in the B-region as well, whereas in [75], for the B-region, squares were used. In particular, in the present simulations, a finer trapezoidal element is chosen close to the A-region boundaries so the fields are accurately solved when the particles approaching the internal region. A comparison between the two meshes showed a difference in the bulk properties less than 0.5% against a substantial decreasing in the CPU time and memory. The mesh parameters for the B-region depend on the distance between its boundaries and the A-region ones, as discussed below. Finally, a constant time step $\Delta t = 0.05$ is chosen.

In order to discuss about the impact of higher Wi on the suspension properties, the influence of the length of the B-region l_B (see Figure 5.3) on the bulk properties has been

investigated. As discussed in Section 5.5, a region between the internal and external one is mandatory for viscoelastic suspensions. Indeed, after the relocation, the stress surrounding a particle needs to be developed. It would seem that l_B should be proportional to the Weissenberg number. Indeed, for a relaxation time two times higher, the particle needs approximately a distance that is two times as long in order to develop the surrounding stress distribution. This would lead to a huge B-region for high Weissenberg numbers. Luckily, we will show this is really necessary only for dilute systems, since, in concentrated suspensions, the interactions between the particles become more important then the local stress around the particles (when in isolation).

In order to verify this, we have performed simulations for two different Weissenberg numbers, 0.5 and 1.0, by varying l_B from 0.125 to 1.0 (we point out that Wi = 1.0 is the highest Wi exploited in this work). A 150-particle system is considered with $R_p = 0.030$. Again, the Giesekus model with $\alpha = 0.1$ is used to model the viscoelastic medium. The mesh parameters are reported in Table 5.2. The number of elements in the B- and C-region are chosen such that, even when a particle is relocated, a good discretization inside the particle is assured. Note that with $l_B = 0$ a two-region scheme is recovered (the B-region is suppressed). Furthermore, simulations for a single particle and Wi = 0.1 show that $l_B = 0.25$ is sufficient such that the particle completely develops the polymer stress after the relocation and before entering the A-region. Thus, for Wi = 0.5 and Wi = 1.0, we expect l_B at least five and ten times that distance, respectively, i.e. $l_B = 1.25$ and $l_B = 2.5$. Since the dimension of the B-region changes, it is necessary to modify the total number of particles in order to perform simulations at the same particle area fraction (chosen about 0.20). The results are shown in Figure 5.7, where the average relative bulk viscosities $\overline{\eta}_{1,r}$ are plotted versus l_B. In both cases we observe an increasing behavior. First of all, the viscosities corresponding to the minimum and maximum distance investigated are close to

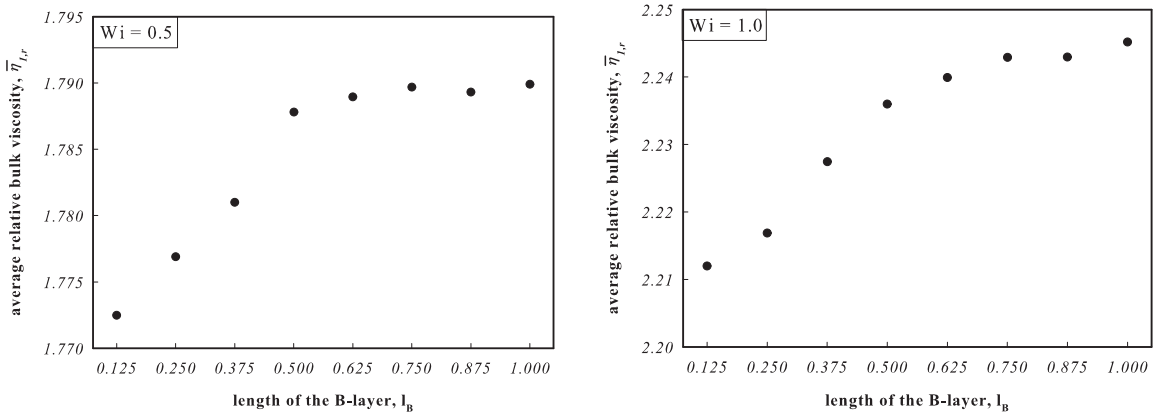

Figure 5.7: Average relative bulk viscosities as a function of the length of B-region. The results for Wi = 0.5 (a) and Wi = 1.0 (b) are plotted.

Table 5.2: Mesh parameters for the B- and C-region.

l_B	$n_B + n_C$
0.125	15
0.250	20
0.375	25
0.500	30
0.625	35
0.750	40
0.875	45
1.000	50

each other (the difference is $\cong 1\%$ for $\mathrm{Wi} = 0.5$ and $\cong 1.5\%$ for $\mathrm{Wi} = 1.0$). Furthermore, there exists a value for l_B beyond which the viscosities do not change anymore. These values (0.625 for $\mathrm{Wi} = 0.5$ and 0.750 for $\mathrm{Wi} = 1.0$) are by far less than the expected ones (i.e. 1.25 for $\mathrm{Wi} = 0.5$ and 2.5 for $\mathrm{Wi} = 1.0$). Therefore, the local development of the stress tensor field due to the inter-particle interactions is more important than the distribution of stress around the particles (as if it were in isolation). In our simulations, $l_B = 0.5$ will be used for $\mathrm{Wi} = 0.5$ and $\mathrm{Wi} = 1.0$, since this choice does not affect the bulk properties (the difference with $l_B = 1.0$ is less than 0.1% in both cases) and leads to a reasonable computational time (as already mentioned, $l_B = 0.25$ is instead chosen for $\mathrm{Wi} = 0.1$).

5.6.2 Simulation results

The first results presented now refer to a simulation of a 150-particle problem with $R_p = 0.03$ (corresponding to $\phi \cong 0.20$). The trend of the velocity, pressure and stress local fields look qualitatively like the Newtonian suspension [75]. Indeed, for an example, the local distribution of xx-component of the stress tensor shows the highest values along the horizontal direction between two particles and the lowest values along the vertical one, as for the Newtonian case. However, in this case, the maximum value of this component of the stress tensor is higher than the Newtonian one: indeed, now, there is also the polymer contribution to the bulk stress.

More interesting are the local distributions of the trace of the conformation tensor $\boldsymbol{c}$. In Figures 5.8, 5.9 and 5.10 the contour plots of $\mathrm{tr}\,\boldsymbol{c}$, for $\mathrm{Wi} = 0.1$, $\mathrm{Wi} = 0.5$ and $\mathrm{Wi} = 1.0$ respectively, are reported. These snapshots are taken after the transient phase and only the A-region is depicted.

For an unfilled Giesekus fluid, the trace of $\boldsymbol{c}$ values, for the three Wi exploited, are $\mathrm{tr}\,\boldsymbol{c}|_{\mathrm{Wi}=0.1,\phi=0} = 2.07$, $\mathrm{tr}\,\boldsymbol{c}|_{\mathrm{Wi}=0.5,\phi=0} = 4.65$ and $\mathrm{tr}\,\boldsymbol{c}|_{\mathrm{Wi}=1.0,\phi=0} = 13.03$. Firstly, we can observe the existence of regions where the fluid is more (white zones) and less (dark zones) stretched than the unfilled polymer. Furthermore, for high Weissenberg numbers, these highly stretched regions seem to be localized in narrow bands, suggesting highly oriented regions where polymer molecules are induced along these directions. Such a phenomenon can affect the final behavior and mechanical properties of the suspension (for example by

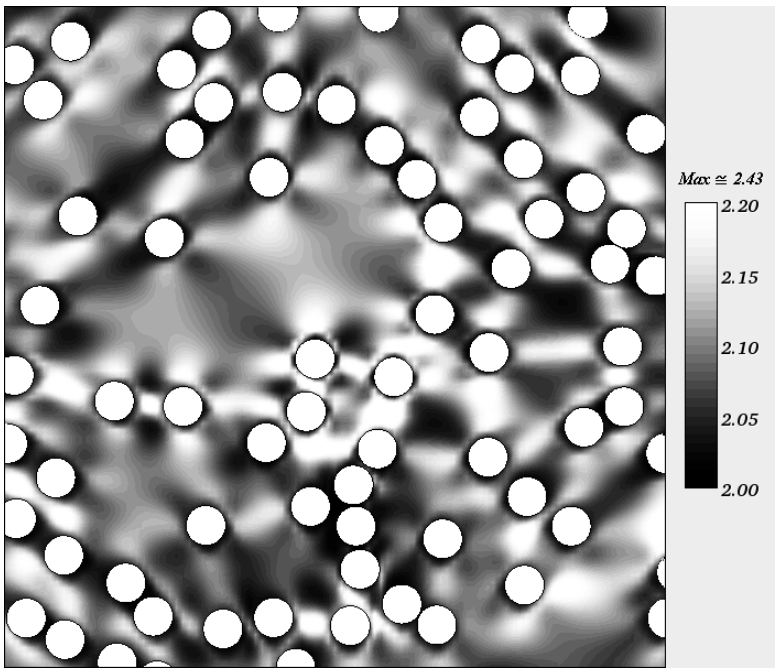

Figure 5.8: Contour plot of the trace of the conformation tensor for a 150-particle system and Wi = 0.1

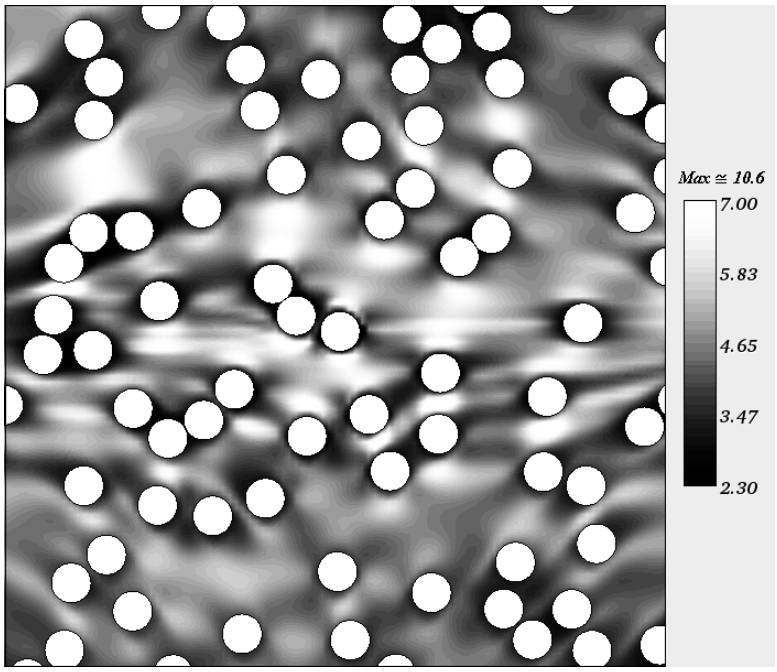

Figure 5.9: Contour plot of the trace of the conformation tensor for a 150-particle system and Wi = 0.5

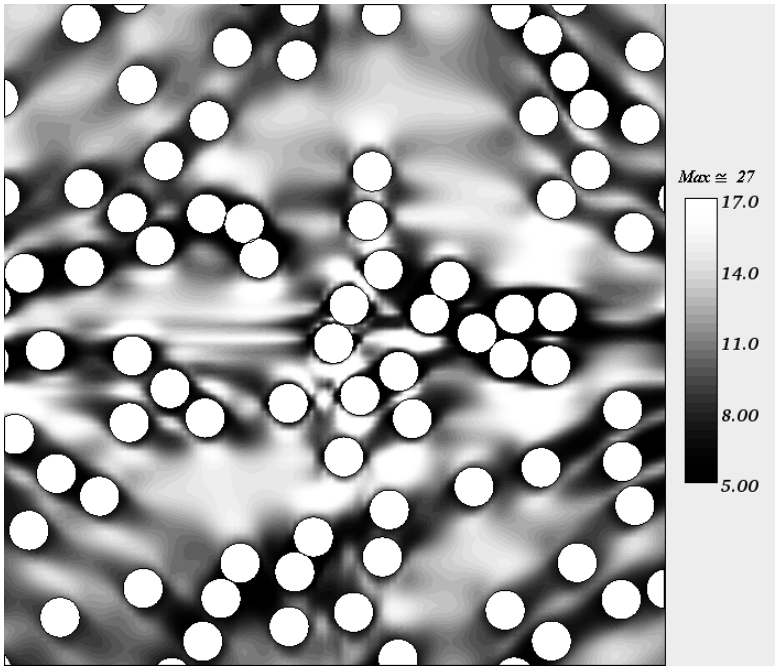

Figure 5.10: Contour plot of the trace of the conformation tensor for a 150-particle system and Wi = 1.0

enhancing the nucleation and crystallization processes during processing of the material). Finally the stretched regions quickly disappear for Wi = 0.1 since the polymer stress relaxes fast. Instead, a higher Wi leads to the existence of the stretched zones that survive much longer.

In Figure 5.11, the relative bulk viscosities versus time for different Weissenberg numbers are plotted. The system simulated and the parameters are the same as the Figures 5.8-5.10. In this figure, the trend of the viscosity for a Newtonian suspension with the same number and radius of particles (= same area fraction) is also depicted. First of all, the start-up for the viscoelastic suspension can be noticed: at $t = 0$ the polymer stress is 0 and only the solvent contributes to the bulk viscosity. Despite of this, the curves don't start exactly from the same viscosity value since the initial configuration of the particles (chosen randomly) changes. So, the stress distribution in the suspension will be different. However, for $t = 0$, the suspension bulk stress is the Newtonian one with the same particle initial configuration. Then, for $t > 0$, the polymeric stress starts to develop and an increasing trend of the viscosity in time can be observed. Notice that the startup of the higher Weissenberg numbers (Wi = 0.5 and Wi = 1.0) seems to be somewhat delayed compared to the smaller ones ((Wi = 0.05 and Wi = 0.1). A true steady state (= a viscosity constant in time) cannot be achieved, since the particles go in and out the internal square and the structure changes every time step. So, the viscosity shows fluctuations. Finally, the average relative bulk viscosity for the viscoelastic suspension is lower than the Newtonian one, for low Wi values and vice versa if Wi is increased.

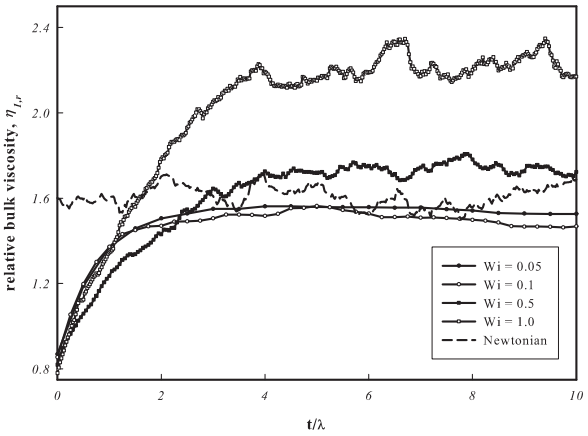

Figure 5.11: Relative bulk viscosities as a function of time for different Weissenberg numbers. For viscoelastic suspensions a start-up can be noticed.

Figure 5.12 shows the average relative bulk viscosities as a function of the particle area fraction for different Wi. The solid curves refer to the viscoelastic suspension simulations whereas the dashed line is the trend of the average relative bulk viscosity for the Newtonian case (the same curve reported in Figure 4.23). Again, the simulated systems refer to 150 particles and the particle area fraction is modified by varying the particle radius. For dilute systems (the three symbols on the curves corresponding to the lowest ϕ values, except, of course, the symbol for $\phi = 0$ evaluated analytically for an unfilled fluid), we changed the number of the particles in the whole domain (N_p) as reported in Table 5.3.

First of all, we can notice an increase in the bulk viscosity by increasing both the

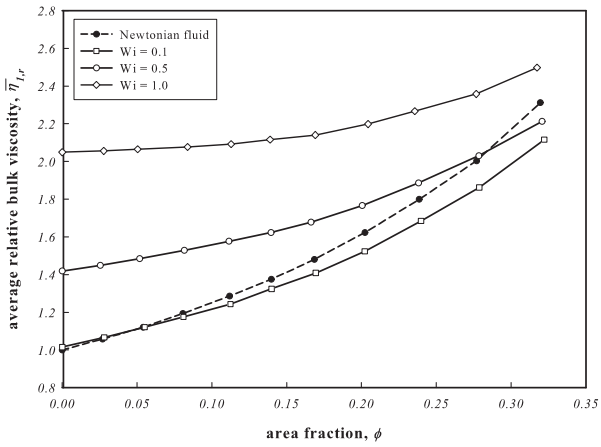

Figure 5.12: Average relative bulk viscosities as a function of the particle area fraction for different Weissenberg numbers (solid lines) and for a Newtonian suspension (dashed line).

Table 5.3: Number of particles used to simulate dilute systems.

Wi	N_p	ϕ
0.1	20	0.0281
0.1	40	0.0551
0.1	60	0.0810
0.5	35	0.0255
0.5	70	0.0517
0.5	110	0.0816
1.0	35	0.0278
1.0	70	0.0504
1.0	110	0.0837

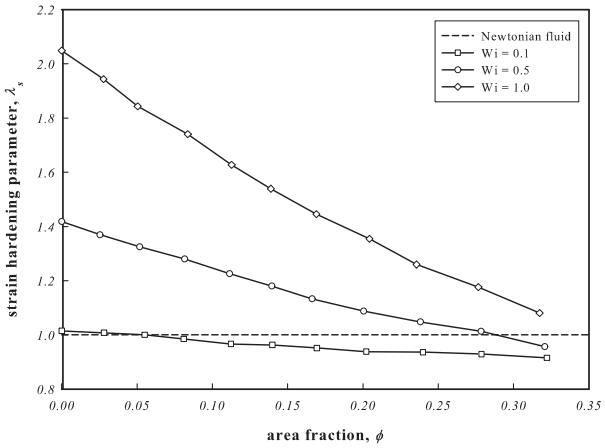

Figure 5.13: Strain hardening parameter versus the particle area fraction for different Weissenberg numbers (solid lines) and for a Newtonian suspension (dashed line).

particle area fraction (according to an exponential-like trend) and the Weissenberg number. Furthermore, the viscoelastic curves show a smaller slope than the Newtonian curve: as a consequence, in the particle area fraction range investigated, the intersection point between the viscoelastic curves and the Newtonian one moves to higher area fractions, if Wi is higher.

It is well known from experimental results of concentrated suspensions in elongational flow that adding particles will reduce the extent of strain hardening [77, 18]. To quantify the effect of the Weissenberg number, the strain hardening parameter λ_s is introduced in the experimental extensional literature [18, 78]:

$$\lambda_s = \frac{\eta_{1,r}(\mathrm{Wi}, \phi, t)}{\eta_{1,r}(\mathrm{Wi} = 0, \phi, t)} \tag{5.52}$$

In words: the strain hardening parameter is the ratio of the extensional viscosity at time t and the particle area fraction ϕ at a given Wi over the extensional viscosity at the

same time and area fraction but for Wi = 0. Since in Figure 5.12, the average pseudo-steady state relative bulk viscosities are plotted, in our case λ_s is given by the ratio of the viscoelastic viscosity at a fixed ϕ over the viscosity of the Newtonian system at the same ϕ. Experimental results show that λ_s is a decreasing function of the area fraction, at a fixed Wi, whereas it is an increasing function of Wi, at a fixed ϕ [18].

Our calculations qualitatively agree. In Figure 5.13, λ_s versus ϕ is plotted for the Wi values previously considered. Of course, for the Newtonian case, λ_s is equal to 1.0 independently from the particle area fraction (dashed line). As we can see, the strain hardening effect is reduced by increasing the particle concentration. Furthermore, the values for Wi = 0.1 are below the Newtonian ones when ϕ is higher than 0.05: the strain hardening has completely disappeared. On the contrary, if we observe the curve for the highest Wi exploited, the strain hardening decreases but does not vanish, at least in the ϕ range investigated. However, one should consider that our quantitative values are strictly related to the viscoelastic model and the parameters chosen.

Finally, the trend of $\bar{\eta}_{1,r}$ and λ_s as function of Wi is shown in Figure 5.14. The solid line is the relative viscosity of an unfilled fluid, whereas the solid circles refers to a filled suspension with $\phi = 0.20$. The open circles is the trend of λ_s for $\phi = 0.20$. In this plot, the λ_s curve is the $\bar{\eta}_{1,r}$ one scaled by a factor equal to the viscosity of the Newtonian suspension, for the same area fraction. As expected, an increase of the relative viscosity for a suspension compared with the unfilled fluid is predicted. It is important to point out that for an unfilled fluid, the average relative bulk viscosity and λ_s are the same. Hence, since the open circles are below the unfilled fluid one for every Wi, a reduction of strain hardening is predicted in the whole range of Wi exploited, as experimentally observed. Moreover, λ_s shows initially a decreasing trend with Wi, then a minimum is achieved and it increases for higher Wi.

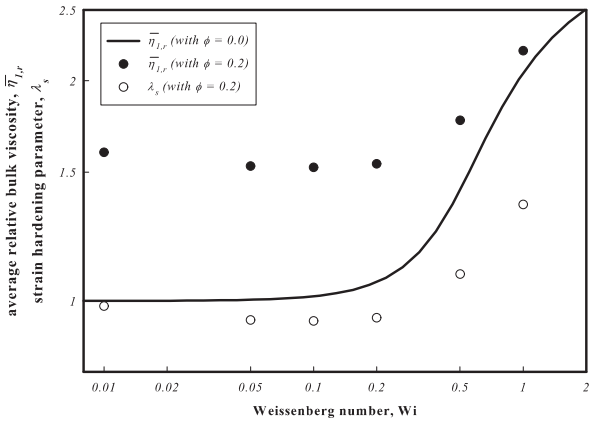

Figure 5.14: Average relative bulk viscosity (solid circles) and strain hardening parameter (open circles) versus the Weissenberg number for $\phi \cong 0.20$. The viscosity for an unfilled Giesekus fluid is reported as well (solid line).

The effects just shown can be explained by considering that the flow in between the objects in the suspension is not in a pure elongational flow and a mixture of elongational and shear flow is present. In this regard, let us consider the contour plots of the distribution of local Weissenberg number:

$$Wi_{\text{loc}} = \lambda\sqrt{1/2(\mathbf{D} : \mathbf{D})} \tag{5.53}$$

shown in Figures 5.15 and 5.16, for Wi = 0.1 and Wi = 1.0, respectively. First of all, we can see that the Wi_{loc} values are higher that the external imposed one.

In particular, the highest values are where two or more particles are close to each other (white zones). Furthermore the particles rotate and shear each other by the effect of hydrodynamic interactions. The combination of these two effects suggests that the fluid between near particles is sheared as well, where the Weissenberg number is higher. As the Figure 5.6 shows, the shear thinning phenomenon occurs and leads to the decreasing of the viscosity previously predicted. This effect is not so important for low Wi values since, as the Figure 5.6 states, the shear thinning (also for Wi = 0.5) does not lead to a considerable reduction in the viscosity. On the contrary, for Wi = 1.0, when Wi_{loc} can be very high (about 4.0), the viscosity can decrease significantly. So, the strain hardening reduction is especially observed for high Weissenberg numbers, as shown in Figure 5.14. Hence, the analysis just carried out suggests that the ratio between shear thinning and strain hardening might be a very important parameter since it affects significantly the bulk viscosity of the suspension.

Finally, a comparison with the theoretical analysis carried out in Chapter II (and in [14, 15, 16]) is done. According to the analytical predictions for a second-order fluid (SOF), λ_s decreases with ϕ and increases with Wi. It is important to point out that in Chapter II we consider a dilute system (so the theory is valid only for low ϕ) and the SOF model (and the perturbative technique used) is rigorous only for very low Weissenberg numbers ($0 \leq \text{Wi} \leq 0.15$). In this range, this model can be assumed like the asymptote for more realistic viscoelastic models. The results presented here predict a similar behavior with regard of the dependence on the area fraction: it's clear from Figure 5.13 that λ_s decreases with ϕ, also for the lowest Wi value exploited.

A more complex discussion regards the λ_s dependence on the Weissenberg number. In Figure 5.14 we can see that, for small Wi where the SOF is valid, the behavior is the opposite with respect to the dilute theory. However, the results shown in this figure refer to a strongly non-dilute suspension, where the theory is not valid anymore. Hence, we deduce that hydrodynamic interactions play a crucial role when the number of the particles increases. This would confirm what we previously said: the λ_s reduction when Wi is increased is due to the shear flows between the particles. These flows, in fact, do not arise in a dilute system since the particles are so far that do not feel the presence of each other.

Instead, observing the region of Figure 5.13 corresponding to small area fraction, we see that the viscoelastic curves are higher than the Newtonian one, even for the smallest Wi exploited. So, by fixing ϕ sufficiently small to consider a dilute system, an increasing

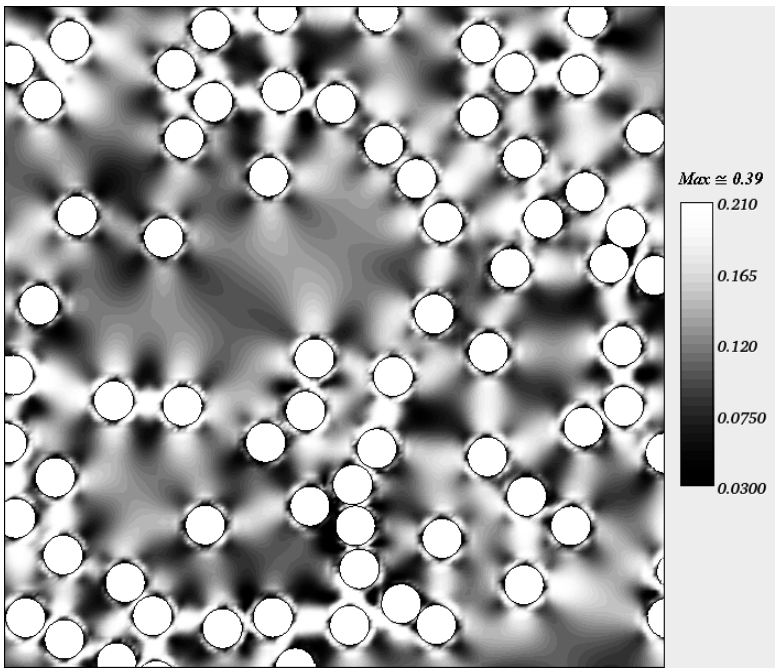

Figure 5.15: Contour plot of the local Weissenberg number for a 150-particle system and Wi = 0.1.

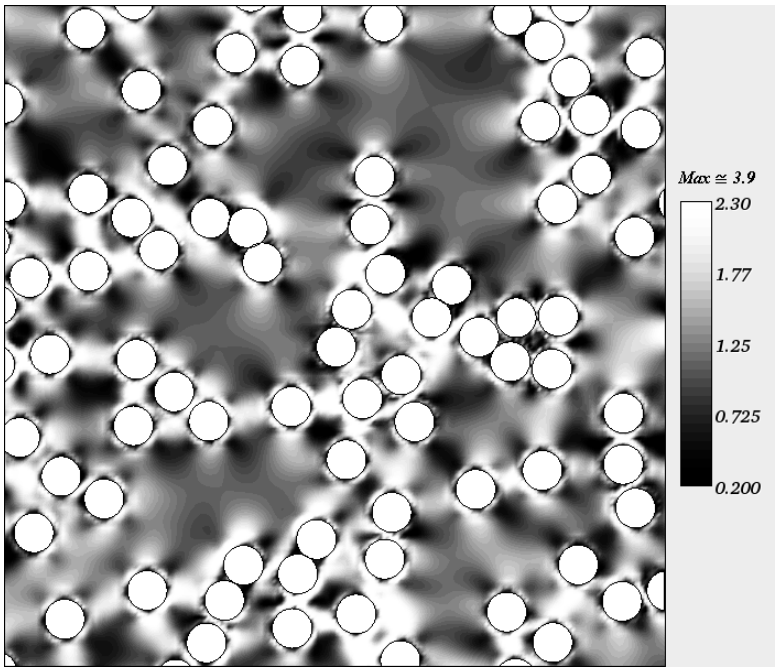

Figure 5.16: Contour plot of the local Weissenberg number for a 150-particle system and Wi = 1.0.

trend of λ_s with Wi is observed, in qualitative agreement with the results in Chapter II (and [14, 15, 16]). A quantitative comparison cannot be carried out since we simulated 2D systems whereas in Chapter II a 3D problem is considered.

However, the main objective of this work is to characterize the rheology of concentrated suspensions and so the developed method is proper to manage systems with an high number of particles. If one is interested in the dilute suspensions, very good theoretical results, that have been confirmed experimentally too, are available in the literature.

5.7 Conclusions

In this Chapter, numerical results of simulations of concentrated rigid particle viscoelastic suspensions are presented. An external elongational flow is imposed and the viscoelastic medium has been modeled like a Giesekus fluid in order to take into account the typical phenomenon of strain hardening in such a flow field.

The simulation scheme used has been presented in the previous Chapter and in [75] and it is based on a random relocation of the particles on the inflow boundaries when they go out the outflow ones. The three-region scheme used allows to manage a relatively small computational domain and impose the external boundary conditions far from the particles. As remarked in Chapter III and in [75], the particles cannot move in the external region and are relocated on the inflow boundaries of the intermediate one. As a consequence, after relocation and before the particle enters into the internal region (where the bulk properties are evaluated), the polymer stress tensor has time to develop.

A fictitious domain is also used and the particles are discretized through their boundaries only (rigid-ring description). Finally, the rigid-body motion is imposed by means of Lagrange multipliers. According to this scheme, a time-independent, fixed, regular mesh can be used without any deformation of the domain (so no remeshing is needed).

Finally, a steady state in a statistical meaning can be achieved and the micro-structural interactions can be studied.

The scheme is combined with a DEVSS-G/SUPG formulation and the log-conformation representation of the constitutive equation is used, leading to an increase of the numerical stability of the method.

The bulk properties are calculated by using the Batchelor formula where a particle as well as a fluid contribution is taken into account.

A code validation/verification shows the same features remarked in Chapter III and in [75]: i) the number of collocation points affects the bulk properties and ii) the discontinuity of pressure and stresses through the particle boundaries cannot be predicted. However, a similar relationship between the stress tensor and Lagrange multipliers is obtained so the bulk calculations can be successfully performed. Moreover, preliminary simulations showed that the size of the intermediate region can be chosen relatively small in order to get a good accuracy. Indeed, the hydrodynamic interactions between the particles seem to be more important than the development of the viscoelastic stress after the relocation.

The local distribution of the conformation tensor shows the presence of highly oriented

regions. Moreover, the presence of particles lead to non-uniform fluid zones where the polymer is less or more stretched than the unfilled one. The prediction of these regions can be useful in processes where the polymer molecule orientation plays a crucial role.

The average relative bulk viscosities, evaluated over many configurations, show an increasing behavior with respect to the particle area fraction and Weissenberg number. However, the slope of these curves is found to be less steep than the Newtonian one. As a consequence, we found a decreasing strain hardening parameter with increasing the particle fraction. This effect is exactly what the experimental data show [18] so our calculations are in qualitative agreement with them, predicting the reduction of the strain hardening.

This phenomenon can be explained by considering that, by means of the particle motion, the fluid in between the inclusions is sheared. An analysis of the local Weissenberg number shows the highest values (greater than the external imposed one) occur where the polymer is sheared. This effect enhances the shear thinning, leading to the decreasing of the elongational bulk viscosity experimentally (and numerically) observed.

Finally, a good qualitative agreement with a dilute SOF theory is also found whereas a quantitative comparison cannot be assessed since our calculations are limited to 2D case. In this regard, our relocation scheme can be easily extended to 3D, however the computational demands on memory and CPU time for the currently employed direct solver would restrict the system to very low resolutions. Use of iterative solvers and a parallel implementation will be required to resolve this problem.

Chapter 6

Conclusions

In this thesis, a study of solid particles in a viscoelastic suspending liquid is carried out by means of numerical simulations. It's well known from the experimental literature on this topic that the presence of particles alter the fluid dynamic of the fluid and leads to rheological non linear phenomena, even if the matrix shows a Newtonian behavior. A crucial parameter is then the particle volume fraction that classifies the suspensions in dilute ($< 5-6\%$) and concentrated (up to $30-40\%$). It's quite obvious that the diluteness hypotheses simplifies the problem since only a single particle needs to take into account, being the others sufficiently far such that no interaction arises. Under the other hypotheses (assumed throughout the work) of spherical, non-Brownian, buoyancy free particles and neglecting the inertia of the particles as well as of the fluid, the analysis is firstly carried out for a dilute viscoelastic suspension, extending the study to concentrated ones in the second part of this thesis.

A continuum approach is used, i.e. the simulations are performed by solving the balance equations for such a system (continuity and momentum), in general coupled with a constitutive equation representing a particular viscoelastic model. The finite element method is used and proper stabilization techniques are introduced when required (high Weissenberg number). By solving the governing equations, the local fields (pressure, velocity and stress tensor) can be obtained. The properties of the material considered as a whole (= bulk properties) are then recovered by implementing a standard averaging procedure [9].

In Chapter II, we start the analysis by choosing a simple constitutive equation for the medium, i.e. the "Second Order Fluid". This model is the most general properly invariant stress tensor quadratic in the velocity gradient [33] and is valid for slow and slowly varying flow [33] (low Weissenberg number). This features allows to use a perturbative technique considering the Weissenberg number as perturbative parameter. Therefore, analytical expressions for the local fields can be obtained and, finally, an analytical prediction for the bulk stress tensor is recovered. These analytical results are confirmed by 3D numerical simulations. Since the SOF stress tensor is explicitly related to velocity gradients, a standard velocity - pressure formulation is implemented.

For simple shear flow, the analytical results show a bulk viscosity equal to the Einstein prediction, in the whole $Wi-$range exploited. Instead, in uniaxial elongational flow, the

presence of particles leads to an high viscosity then the unfilled fluid, which increases with Wi as well. Regarding the normal stress differences in shear, bulk N_1 increases with Wi and is independent of SOF constitutive parameter whereas a non-zero bulk N_2 is found, decreasing with Wi.

Our predictions are in excellent agreement with the numerical simulations and in qualitatively agreement with experimental data found in literature.

In Chapter III, the SOF theory is abandoned and the analysis is focused to non-vanishing Weissenberg number (up to 2.5). More realistic viscoelastic equations need to be considered and the choice is so made that different non-linear phenomena can be separately taken into account. A cubic cell with the sphere at the center is chosen so, under simple shear flow, it can only rotate. However, the rotation rate is unknown in advance, if a suspending viscoelastic liquid is considered. Therefore, by imposing the rigid-body motion on the sphere surface by means of constraints, the angular velocity is added as additional unknown and can be recovered by solving the full system of equations.

About the rotation of the sphere, our simulations results are able to capture the experimentally observed [20] slowing down. However, a purely viscous shear thinning model (Bird-Carreau) is not sufficient to predict such a slowing down. Therefore, this effect seems to be related to normal stresses. In particular, the Maxwell model predicts the slowest rotation whereas the Giesekus and Phan-Thien Tanner curves lie in between the Maxwell and Newtonian ones. However, the additional constitutive parameter of GSK and PTT models strongly affect the slope of these curves.

The bulk rheology of such a suspension is then investigated. For Maxwell model, the viscosity shows a slight shear thins behaviour even if the unfilled fluid predicts a constant viscosity. Furthermore, the presence of the particles increase bulk N_1 with respect to the pure fluid and, surprisingly, lead to non zero bulk second normal stress differences.

The steady state bulk viscosity and N_1 for PTT and GSK shows a similar behaviour and both are higher then the corresponding unfilled fluid quantity. As in Maxwell, a non zero second normal stress difference is found for PTT if particles are added into the fluid. The influence of the particle concentration is also investigated. Our simulations predict a decreasing bulk N_1 and a increasing bulk N_2 (in absolute value) if the volume fraction is increased. These results are in qualitatively agreement with experimental data from literature [17]. Finally, an excellent agreement with SOF analytical predictions is also found, for vanishing Weissenberg number.

In the second part of this thesis (Chapter IV and V), the diluteness hypothesis is removed. Due to the high particle concentration, hydrodynamic interactions need to be taken into account. The approach used is based on the Direct Numerical Simulations where the governing equations for the fluid and the rigid-body motion for the solid are directly solved (coupled through the no-slip boundary conditions and force-free and torque-free conditions). In order to easily manage the particle motion, a fictitious domain is implemented together a rigid ring description of particle boundary [30, 28].

To handle a sufficiently small computational domain representing an infinite frame of the suspension, periodic conditions should be imposed. This concept has been applied successfully for shearing flows [28, 27]. On the contrary, a periodic domain in elongational

flow leads to the necessity to consider stretching frame and limits the highest Wi that can be achieved [29].

Therefore, we implemented a new simulation scheme for direct simulation of concentrated particle suspensions in planar elongational flow. The basic idea is to relocate a particle on the inflow boundary of the domain when it crosses the outflow sections. The simulation scheme is based on a three-layer domain in order to impose the planar elongational flow boundary conditions sufficiently far from the particles and calculate the steady state properties (in a statistical meaning) of the suspension. We don't need to deform the computational domain (so no remeshing and projection are required) and no periodic boundary condition is imposed.

The scheme is applied to concentrated Newtonian suspensions first, in order to validate the code and compare with [29]. A many-particle problem (150 and 225 particles) is solved and the local distribution of the flow and stress fields as well as the bulk properties are evaluated.

The results showed a very good agreement with dilute theory as well as numerical simulations from [29]. In particular, for low particle area fractions, the relative bulk viscosity approaches the Einstein's analytical solution. By increasing the area fraction, the viscosity increases as well according to an exponential-like trend, as shown in the experiments.

The scheme has been extended to viscoelastic suspensions and the fluid has been modeled like a Giesekus fluid. The local distribution of the conformation tensor shows the presence of highly oriented regions. In addition, the presence of particles lead to non-uniform fluid zones where the polymer is less or more stretched than the pure one [71].

The average relative bulk viscosities, evaluated over many configurations, show an increasing behavior with respect to the particle area fraction and Weissenberg number. However, the slope of these curves is found to be less steep than the Newtonian one. As a consequence, we found a decreasing strain hardening parameter with increasing the particle fraction. This effect is exactly what the experimental data show so our calculations are in qualitative agreement with them, predicting the reduction of the strain hardening.

Appendix A

Derivation of $\boldsymbol{v}_{SOF} = \mathbf{0}$ on the sphere surface

In this Appendix we demonstrate Eq. (2.18). At order Wi, the general expression for $\boldsymbol{v}_{SOF}$ is (Eq. (2.20) in the text):

$$\begin{aligned}\boldsymbol{v}_{SOF} = v_1 \boldsymbol{D}^{\infty}\boldsymbol{D}^{\infty} :: \boldsymbol{uuuuu} + v_2 \boldsymbol{D}^{\infty} \cdot \boldsymbol{D}^{\infty} : \boldsymbol{uuu} + v_3 \boldsymbol{D}^{\infty} : \boldsymbol{D}^{\infty}\, \boldsymbol{u} + \\ v_4 \boldsymbol{D}^{\infty} : \boldsymbol{uu}\, \boldsymbol{D}^{\infty} \cdot \boldsymbol{u} + v_5 \boldsymbol{D}^{\infty} \cdot \boldsymbol{D}^{\infty} \cdot \boldsymbol{u} + v_6 \boldsymbol{A}^{\infty} : \boldsymbol{uuu} + v_7 \boldsymbol{A}^{\infty} \cdot \boldsymbol{u}\end{aligned} \tag{A.1}$$

where, on the sphere surface, the coefficients v_i are real numbers (as yet unknown). We recall that the terms appearing in the RHS of Eq. (A.1) are mutually independent, as they have irreducible tensorial forms. Since the velocity must be tangential to the sphere surface, the coefficients v_1, v_2, v_3 and v_6 must all be zero, because the corresponding terms are directed along $\boldsymbol{u}$. Regarding the remaining three velocity terms, their radial components must be nil, that is:

$$\boldsymbol{v}_{SOF} \cdot \boldsymbol{u} = v_4(1) \boldsymbol{D}^{\infty}\boldsymbol{D}^{\infty} :: \boldsymbol{uuuu} + v_5(1) \boldsymbol{D}^{\infty} \cdot \boldsymbol{D}^{\infty} : \boldsymbol{uu} + v_7(1) \boldsymbol{A}^{\infty} : \boldsymbol{uu} = 0 \tag{A.2}$$

Again, in view of the mutual independence of the terms in Eq. (A.2), the coefficients v_4, v_5, and v_7 must be individually nil. Consequently, $\boldsymbol{v}_{SOF} = \mathbf{0}$ on the sphere surface.

Seemingly, in the above derivation, no use is done of the freely rotating condition (at order Wi). This is a consequence of the adoption, in the expansion procedure, of properly invariant, irreducible tensorial forms. Indeed, the torque free condition at order Wi reads:

$$\int_{4\pi} \boldsymbol{u} \times \boldsymbol{T}_{SOF} \cdot \boldsymbol{u}\, dA = \int_{4\pi} \boldsymbol{u} \times \boldsymbol{w}_{SOF} dA = \mathbf{0} \tag{A.3}$$

where $\boldsymbol{w}_{SOF}$ is a properly invariant order$-Wi$ vector (equal in form to the $\boldsymbol{v}_{SOF}$ vector):

$$\begin{aligned}\boldsymbol{w}_{SOF} = w_1 \boldsymbol{D}^{\infty}\boldsymbol{D}^{\infty} :: \boldsymbol{uuuuu} + w_2 \boldsymbol{D}^{\infty} \cdot \boldsymbol{D}^{\infty} : \boldsymbol{uuu} + w_3 \boldsymbol{D}^{\infty} : \boldsymbol{D}^{\infty}\, \boldsymbol{u} + \\ w_4 \boldsymbol{D}^{\infty} : \boldsymbol{uu}\, \boldsymbol{D}^{\infty} \cdot \boldsymbol{u} + w_5 \boldsymbol{D}^{\infty} \cdot \boldsymbol{D}^{\infty} \cdot \boldsymbol{u} + w_6 \boldsymbol{A}^{\infty} : \boldsymbol{uuu} + w_7 \boldsymbol{A}^{\infty} \cdot \boldsymbol{u}\end{aligned} \tag{A.4}$$

In the surface integral (Eq. (A.3)), all the scalar coefficients w_i are evaluated at $r = 1$. However, the surface integral turns out to be zero independently of the values of those

coefficients. Indeed, it is readily seen that the cross product of $\boldsymbol{u}$ with the first, second, third and sixth terms in the RHS of Eq. (A.4) is nil (because $\boldsymbol{u} \times \boldsymbol{u} = \mathbf{0}$). The surface integrals of the three remaining terms are shown to be zero by inspection. (It can be shown that this latter result directly stems from the symmetric nature of the tensors $\boldsymbol{D}^{\infty}$ and $\boldsymbol{A}^{\infty}$.)

Thus, the adoption of an irreducible representation for order$-Wi$ vectors from one hand *empties* the freely rotating condition, Eq. (2.7), but on the other hand allows one to readily determine $\boldsymbol{v}_{SOF} = \mathbf{0}$ on the sphere surface.

Appendix B

Deviatoric bulk stress of $\boldsymbol{M}_{SOF}$

In this appendix we compute the deviatoric bulk stress by surface integration of the dyad $\boldsymbol{M}_{SOF}$, see Eq. (2.36) in the text. In order to perform the surface integration, the following identities are needed:

$$\int_{4\pi} u_i u_j dA = \frac{4\pi}{3}\delta_{ij} \tag{B.1}$$

$$\int_{4\pi} u_i u_j u_k u_l dA = \frac{4\pi}{15}(\delta_{ij}\delta_{kl} + 2 \text{ terms}) \tag{B.2}$$

$$\int_{4\pi} u_i u_j u_k u_l u_m u_n dA = \frac{4\pi}{105}(\delta_{ij}\delta_{kl}\delta_{mn} + 14 \text{ terms}) \tag{B.3}$$

where, in the RHS of Eq. (B.2) and (B.3), appropriate index permutation is implied. The seven integrals from the dyad $\boldsymbol{M}_{SOF}$ are then straightforwardly calculated:

$$\int_{4\pi} \boldsymbol{D}^\infty \boldsymbol{D}^\infty :: \boldsymbol{uuuuuu}\, dA = \frac{4\pi}{105}(2\boldsymbol{D}^\infty : \boldsymbol{D}^\infty \boldsymbol{I} + 8\boldsymbol{D}^\infty \cdot \boldsymbol{D}^\infty) \tag{B.4}$$

$$\int_{4\pi} \boldsymbol{D}^\infty \cdot \boldsymbol{D}^\infty : \boldsymbol{uuuu}\, dA = \frac{4\pi}{15}(\boldsymbol{D}^\infty : \boldsymbol{D}^\infty \boldsymbol{I} + 2\boldsymbol{D}^\infty \cdot \boldsymbol{D}^\infty) \tag{B.5}$$

$$\int_{4\pi} \boldsymbol{D}^\infty : \boldsymbol{D}^\infty\, \boldsymbol{uu} dA = \frac{4\pi}{3}\boldsymbol{D}^\infty : \boldsymbol{D}^\infty \boldsymbol{I} \tag{B.6}$$

$$\int_{4\pi} \boldsymbol{D}^\infty : \boldsymbol{uu}\, \boldsymbol{D}^\infty \cdot \boldsymbol{uu} dA = \frac{8\pi}{15}\boldsymbol{D}^\infty \cdot \boldsymbol{D}^\infty \tag{B.7}$$

$$\int_{4\pi} \boldsymbol{D}^\infty \cdot \boldsymbol{D}^\infty \cdot \boldsymbol{uu} dA = \frac{4\pi}{3}\boldsymbol{D}^\infty \cdot \boldsymbol{D}^\infty \tag{B.8}$$

$$\int_{4\pi} \boldsymbol{A}^\infty : \boldsymbol{uuuu}\, dA = \frac{8\pi}{15}(2\boldsymbol{D}^\infty : \boldsymbol{D}^\infty \boldsymbol{I} + \boldsymbol{A}^\infty) \tag{B.9}$$

$$\int_{4\pi} \boldsymbol{A}^\infty \cdot \boldsymbol{uu} dA = \frac{4\pi}{3}\boldsymbol{A}^\infty \tag{B.10}$$

By grouping terms, the nondimensional deviatoric bulk stress at order Wi reads:

$$\frac{\langle \boldsymbol{\tau}_{SOF} \rangle}{\phi} = (\frac{8}{35}m_1 + \frac{2}{5}m_2 + \frac{2}{5}m_4 + m_5)\boldsymbol{D}^{\infty} \cdot \boldsymbol{D}^{\infty} + (\frac{2}{5}m_6 + m_7)\boldsymbol{A}^{\infty} \tag{B.11}$$

The coefficients m_i of the dyad $\boldsymbol{M}_{SOF}$ (evaluated at $r = 1$) needed in Eq. (B.11) are:

$$m_1 = -\frac{25}{2} \tag{B.12}$$

$$m_2 = \frac{5}{4}(14 + b) \tag{B.13}$$

$$m_3 = \frac{52 - b}{56} \tag{B.14}$$

$$m_4 = \frac{5}{16}(4 + b) \tag{B.15}$$

$$m_5 = \frac{5}{56}\,(-76 + 9\,b) \tag{B.16}$$

$$m_6 = 0 \tag{B.17}$$

$$m_7 = \frac{5}{2} \tag{B.18}$$

By inserting these coefficients into Eq. (B.11), and by adding the contribution from volume integrals, the total stress at order Wi is finally obtained, Eq. (2.37) and Eq. (2.38) in the text.

Bibliography

[1] H. Brenner. Suspension rheology. *Proc. Heat and Mass Transfer*, 5:89, 1972.

[2] D.R. Foss and J.F. Brady. Structure, diffusion and rheology of Brownian suspensions by Stokesian Dynamics simulation. *J. Fluid Mech.*, 407:167, 2000.

[3] C.J. Petrie. The rheology of fibre suspensions. *J. Non-Newtonian Fluid Mech.*, 87:369, 1999.

[4] S. Taneda. Experimental investigation of the wake behind a sphere at low Reynolds numbers. *J. Phys. Soc. Jpn*, 11:1004, 1956.

[5] S. Taneda. Visualization of separating Stokes flows. *J. Phys. Soc. Jpn*, 46:1935, 1979.

[6] C.W. Macosko. *Rheology: principles, measurements, and applications.* Wiley-VCH, New York, 1994.

[7] H.M. Laun. Rheological properties of aqueous polymer dispersions. *Angew. Makromol. Chem.*, 124-125:335, 1984.

[8] A. Einstein. Berichtigung zu Meiner Arbeiten: Eine Neue Bestimmung der Molekul Dimensionen. *Annalen der Physik Berlin*, 19:289, 1906.

[9] G.K. Batchelor. The stress system in a suspension of force-free particles. *J. Fluid Mech.*, 41:545, 1970.

[10] P.N. Kaloni and V. Stastna. Steady-state rheological behavior of the suspension of spherical-particles in a 2nd-order fluid. *Polym. Eng. Sci.*, 23:465, 1983.

[11] K. Sun and K. Jayaraman. Bulk rheology of dilute suspensions in viscoelastic liquids. *Rheol. Acta*, 23:84, 1984.

[12] A.C. Li and J.C. Slattery. Local volume-averaged equations of motions for suspensions in 2nd-order fluids. *Chem. Eng. Comm.*, 85:9, 1989.

[13] D.L. Koch and G. Subramanian. The stress in a dilute suspension of spheres suspended in a second-order fluid subject to a linear velocity field. *J. Non-Newt. Fluid Mech.*, 138:87, 2006.

[14] F. Greco, G. D'Avino, and P.L. Maffettone. Stress tensor of a dilute suspension of spheres in a viscoelastic liquid. *Phys. Rev. Lett.*, 95:246001, 2005.

[15] F. Greco, G. D'Avino, and P.L. Maffettone. Erratum - Stress tensor of a dilute suspension of spheres in a viscoelastic liquid (vol 95, pg 246001, 2005). *Phys. Rev. Lett.*, 98:109904, 2007.

[16] F. Greco, G. D'Avino, and P.L. Maffettone. Rheology of a dilute suspension of rigid spheres in a second order fluid. *J. Non-Newtonian Fluid Mech.*, 147:1, 2007.

[17] S.E. Mall-Gleissle, W. Gleissle, G.H. McKinley, and H. Buggisch. The normal stress behaviour of suspensions with viscoelastic matrix fluids. *Rheol. Acta*, 41:61, 2002.

[18] J.-F. Le Meins, P. Moldenaers, and J. Mewis. Suspensions of monodisperse spheres in polymer melts: particle size effects in extensional flow. *Rheol. Acta*, 42:184, 2003.

[19] R. Scirocco, J.Vermant, and J. Mewis. Shear thickening in filled boger fluids. *J. Rheol.*, 49:551, 2005.

[20] M. Astruc, S. Vervoort, H.O. Nouatin, T. Coupez, Y. De Puydt, P. Navard, and E. Peuvrel-Disdier. Experimental and numerical study of the rotation and the erosion of fillers suspended in viscoelastic fluids under simple shear flow. *Rheol. Acta*, 42(5):421, 2003.

[21] J.F. Brady and G. Bossis. Stokesian dynamics. *Ann. Rev. Fluid Mech.*, 20:111, 1988.

[22] P. Smereka. On the motion of bubbles in a periodic box. *J. Fluid Mech.*, 254:79, 1993.

[23] A.S. Sangani and A.K. Didwania. Dynamic simulations of flow of bubbly liquids at large Reynolds numbers. *J. Fluid Mech.*, 250:307, 1993.

[24] J.N. McLaughlin. Numerical computation of particle-turbulent interaction. *Int. J. Multiphase Flow*, 20:211, 1994.

[25] M.J. Andrews and P.J. O'Rourke. The multiphase particle-in-cell (MP-PIC) method for dense particulate flows. *Int. J. Multiphase Flow*, 22:379, 1996.

[26] D.M. Snider, P.J. O'Rourke, and M.J. Andrews. Sediment flow in inclined vessels calculated using a multiphase particle-in-cel model for dense particle flows. *Int. J. Multiphase Flow*, 24:1359, 1998.

[27] W.R. Hwang, M.A. Hulsen, and H.E.H. Meijer. Direct simulation of particle suspensions in a viscoelastic fluid in sliding bi-periodic frames. *J. Non-Newtonian Fluid Mech.*, 121:15, 2004.

[28] W.R. Hwang, M.A. Hulsen, and H.E.H. Meijer. Direct simulation of particle suspensions in sliding bi-periodic frames. *J. Comput. Phys.*, 194:742, 2004.

[29] W.R. Hwang and M.A. Hulsen. Direct numerical simulations of hard particle suspensions in planar elongational flow. *J. Non-Newtonian Fluid Mech.*, 136:167, 2006.

[30] R. Glowinski, T.-W. Pan, T.I. Hesla, and D.D. Joseph. A distributed Lagrangian multipliers/fictitious domain method for particulate flows. *Int. J. Multiphase Flow*, 25:755, 1999.

[31] H.A. Barnes. *in Rheology Reviews 2003*, page British Society of Rheology., 2003.

[32] L.D. Landau and E.M. Lifshitz. *Fluid Mechanics*. Pergamon Press.

[33] C.A. Truesdell and W. Noll. in: S.Flugge (Ed.), Encyclopaedia of Physics. III/3, Springer, 1965.

[34] R.G Larson. *The Structure and Rheology of Complex Fluids*. Oxford University Press, 1998.

[35] P.O. Brunn. Slow motion of a sphere in a second-order fluid. *Rheol. Acta*, 15:163, 1976.

[36] L.G. Leal. The motion of small particles in nonNewtonian fluids. *J. Non-Newtonian Fluid Mech.*, 5:33, 1979.

[37] G.K. Batchelor. Transport properties of 2-phase materials with random structure. *Ann. Rev. Fluid Mech.*, 6:227, 1974.

[38] F. Greco. Second-order theory for the deformation of a Newtonian drop in a stationary flow field. *Phys. Fluid*, 14:946, 2002.

[39] F. Greco. Drop deformation for non-Newtonian fluids in slow flows. *J. Non-Newtonian Fluid Mech.*, 107:111, 2002.

[40] J.H. Peery. *Fluid mechanics of rigid and deformable particles in shear flows at low Reynolds numbers*. PhD thesis, Princeton University, Princeton.

[41] F. Brezzi and M. Fortin. *Mixed and Hybrid Finite Element Methods*. Springer-Verlag, 1991.

[42] R. Guénette and M. Fortin. A new mixed finite element method for computing viscoelastic flows. *J. Non-Newtonian Fluid Mech.*, 60:27, 1995.

[43] B.K. Aral and D.M. Kalyon. Viscoelastic material functions of noncolloidal suspensions with spherical particles. *J. Rheol.*, 41:599, 1997.

[44] F. Gauthier, H.L. Goldsmith, and S.G. Mason. Particle motions in non-newtonian media, I. Coutte flow. *Rheol. Acta*, 10:344, 1971.

[45] F. Gauthier, H.L. Goldsmith, and S.G. Mason. Particle motions in non-newtonian media, II. Poiseuille flow. *Trans. Soc. Rheol.*, 15:297, 1971.

[46] E. Bartram, H.L. Goldsmith, and S.G. Mason. Particle motions in non-newtonian media, III. Further observations in elasticoviscous fluids. *Rheol. Acta*, 14:776, 1975.

[47] D.J. Highgate and W. Whorlow. Rheological properties of suspensions of spheres in non-Newtonian media. *Rheol. Acta*, 9:569, 1970.

[48] N. Ohl and W. Gleissle. The characterization of the steady-state shear and normal stress functions of highly concentrated suspensions formulated with viscoelastic liquids. *J. Rheol.*, 37:381, 1993.

[49] I.E. Zarraga, D.A. Hill, and D.T. Leighton jr. Normal stresses and free surface deformation in concentrated suspensions of noncolloidal spheres in a viscoelastic fluid. *J. Rheol.*, 45:1065, 2001.

[50] R.B. Bird and P.J. Carreau. A nonlinear viscoelastic model for polymer solutions and melts - I. *Chem. Eng. Sci.*, 23:427, 1968.

[51] R.B. Bird, R.C. Armstrong, and O. Hassager. *Dynamics of polymeric liquids, Vol. 1, Fluid Dynamics*. Wiley, New York edition, 1977.

[52] N. Phan Thien and R.I. Tanner. A new constitutive equation derived from network theory. *J. Non-Newtonian Fluid Mech.*, 2:353, 1977.

[53] N. Phan Thien. A nonlinear network viscoelastic model. *J. Rheol.*, 22:259, 1978.

[54] H. Giesekus. A simple constitutive equation for polymer fluids based on the concept of deformation-dependent tensorial mobility. *J. Non-Newtonian Fluid Mech.*, 11:69, 1982.

[55] A.C.B. Bogaerds, A.M. Grillet, G.W.M. Peters, and F.P.T. Baaijens. Stability analysis of polymer shear flows using the extended pom-pom constitutive equations. *J. Non-Newtonian Fluid Mech.*, 108:187, 2002.

[56] A.N. Brooks and T.J.R. Hughes. Streamline upwind/Petrov-Galerkin formulations for convection dominated flows with particular emphasis on the incompressible Navier-Stokes equations. *Comp. Meth. Appl. Mech. Eng.*, 32:199, 1982.

[57] R. Fattal and R. Kupferman. Constitutive laws for the matrix-logarithm of the conformation tensor. *J. Non-Newtonian Fluid Mech.*, 123:281, 2004.

[58] M.A. Hulsen, R. Fattal, and R. Kupferman. Flow of viscoelastic fluids past a cylinder at high Weissenberg number: stabilized simulations using matrix logarithms. *J. Non-Newtonian Fluid Mech.*, 127:27, 2005.

[59] O. Schenk, K. Gartner, and W. Fichtner. Efficient sparse LU factorization with left-right looking strategy on shared memory multiprocessors. *BIT*, 40(1):158, 2000.

[60] O. Schenk and K. Gartner. Solving unsymmetric sparse systems of linear equations with PARDISO. *J. of Future Generation Computer Systems*, 20(3):475, 2004.

[61] O. Schenk and K. Gartner. On fast factorization pivoting methods for symmetric indefinite systems. *Elec. Trans. Numer. Anal.*, 23:158, 2006.

[62] J. Mewis and R. de Bleyser. Concentration effects in viscoelastic dispersions. *Rheol. Acta*, 14:721, 1975.

[63] P. Moldenaers, J. Vermant, E. Heinrich, and J. Mewis. Effect of fillers on the steady state rheological behaviour of liquid crystalline polymers. *Rheol. Acta*, 37:463, 1998.

[64] F. Bertrand, P.A. Tanguy, and F. Thibault. A three-dimensional fictitious domain method for incompressible fluid flow problems. *Int. J. Numer. Meth. Fluids*, 25:719, 1997.

[65] H.H. Hu. Direct simulation of flows of solid-liquid mixtures. *Int. J. Multiphase Flow*, 22:335, 1996.

[66] H.H. Hu, D.D. Joseph, and M.J. Crochet. Direct simulation of fluid particle motions. *Theor. Comp. Fluid Dyn.*, 3:285, 1992.

[67] N.A. Patankar. *Numerical simulation of particulate two-phase flow.* PhD thesis, University of Pennsylvania, Pennsylvania.

[68] A. Johnson and T. Tezduyar. 3D simulation of fluid-particle interactions with the number of particles reaching 100, Research report 96-037. Army High Performance Computing Research Center, University of Minnesota. 1996.

[69] HSL, A collection of Fortran codes for large scale scientific computation. 2002, Available from: http://www.cse.clrc.ac.uk/nag/hsl/.

[70] F.P.T. Baaijens. A fictitious domain/mortar element method for fluid-structure interaction. *J. Non-Newtonian Fluid Mech.*, 79:361, 1998.

[71] G. D'Avino, P.L. Maffettone, M.A. Hulsen, and G.W.M. Peters. Numerical simulation of planar elongational flow of concentrated rigid particle suspensions. *J. Non-Newtonian Fluid Mech.*, in press, 2007.

[72] M.J. Szady, T.R. Salamon, A.W. Liu, D.E. Bornside, R.C. Armstrong, and R.A. Brown. A new mixed finite element method for viscoelastic flows governed by differential constitutive equations. *J. Non-Newtonian Fluid Mech.*, 59:215, 1995.

[73] F.P.T. Baaijens. Mixed finite element methods for viscoelastic flow analysis: A review. *Int. J. Numer. Math. Fluids*, 35:743, 2001.

[74] F.P.T. Baaijens, M.A. Hulsen, and P.A. Anderson. The use of mixed finite element methods for viscoelastic fluid flow analysis. *in Encyclopedia of Computational Mechanics*, Volume 3 Fluids:481, 2004.

[75] G. D'Avino, P.L. Maffettone, M.A. Hulsen, and G.W.M. Peters. A numerical method for simulating concentrated rigid particle suspensions in an elongational flow using a fixed grid. *J. Comp. Phys.*, 226:688, 2007.

[76] R. Larson. *Constitutive equations for polymer melts and solutions.* Butterworth-Heinermann, 1988.

[77] M. Kobayashi, T. Takahashi, J. Takimoto, and K. Koyama. Flow-induced whisker orientation and viscosity for molten composite systems in a uniaxial elongational flowfield. *Polymer*, 36:3927, 1995.

[78] O. Ishizuka and K. Koyama. Elongational viscosity at a constant elongational strain rate of polypropylene melt. *Polymer*, 21:164, 1980.